CHALMERS
UNIVERSITY OF TECHNOLOGY

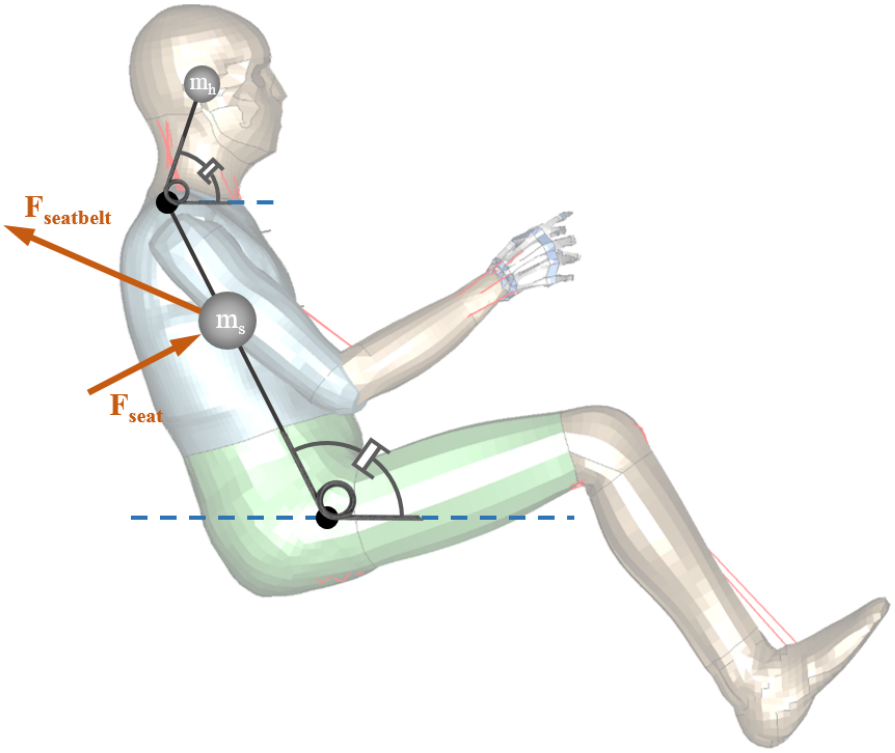

Modeling of Occupant Kinematic Response in Pre-crash Maneuvers

A simplified human 3D-model for simulation of occupant kinematics in maneuvers

Master's thesis in Engineering Mathematics and Biomedical Engineering

OSCAR CYRÉN
SOFIA JOHANSSON

Department of Mechanical and Maritime Sciences
CHALMERS UNIVERSITY OF TECHNOLOGY
Gothenburg, Sweden 2018

Master's thesis 2018:57

Modeling of Occupant Kinematic Response in Pre-crash Maneuvers

A simplified human 3D-model for simulation of occupant kinematics in maneuvers

Oscar Cyrén & Sofia Johansson

CHALMERS
UNIVERSITY OF TECHNOLOGY

Department of Mechanical and Maritime Sciences
Division of Vehicle Safety
Chalmers University of Technology
Gothenburg, Sweden 2018

Modeling of Occupant Kinematic Response in Pre-crash Maneuvers
A simplified human 3D-model for simulation of occupant kinematics in maneuvers
Oscar Cyrén & Sofia Johansson

Supervisors:
Linus Wågström, Volvo Cars Safety Centre
Alexandros Leledakis, Volvo Cars Safety Centre
Alexey Geynts, dept. of Mathematical Sciences, Chalmers University of Technology

Examiner:
Robert Thomson, dept. of Mechanical and Maritime Sciences, div. of Vehicle Safety, Chalmers University of Technology

Master's Thesis 2018:57
Department of Mechanical and Maritime Sciences
Division of Vehicle Safety
Chalmers University of Technology
SE-412 96 Gothenburg
Telephone +46 31 772 1000

Cover: The simplified occupant kinematic model is a 3D pendulum representation of the occupant, where the dimensions and positioning are based on the SAFER HBM (Iraeus *et al.*, 2017) as seen in the background.

Typeset in LaTeX
Gothenburg, Sweden 2018

Modeling of Occupant Kinematic Response in Pre-crash Maneuvers
A simplified human 3D-model for simulation of occupant kinematics in maneuvers
OSCAR CYRÉN & SOFIA JOHANSSON
Department of Mechanical and Maritime Sciences
Chalmers University of Technology

Abstract

Most car manufacturers today equip their cars with collision avoidance systems which can act to avoid or mitigate a crash. Retrospective studies have shown that these systems help reduce the number of crashes, however the intervening evasive maneuvers provoke occupant displacements. Consequently the occupant's position relative to the restraint systems of the car is affected. Therefore, there is a need to investigate occupant safety also for the pre-crash phase when these evasive maneuvers take place. There are an extensive number of maneuvers to consider and the existing methods for simulating the occupant during the pre-crash phase are inefficient with respect to time. For that reason, a more efficient dynamic model of the occupant was developed to primarily compute the head kinematics and secondarily T1 kinematics, when the occupant model is subjected to the linear- and rotational accelerations that are induced by evasive maneuvers. The model represents the upper body of an occupant, i.e. a front seat passenger or a driver, which is restrained by the seat, the seat belt, as well as the arms if the model is a driver. Two types of occupant models were proposed based on the inverted spherical pendulum theory. The systems of differential equations were derived using Lagrangian mechanics and implemented in Simulink. The models were tuned and validated based on pre-existing volunteer data from vehicle maneuver studies. The results demonstrate that the models were able to capture the occupant kinematics by showing similar dynamic behavior to the kinematics of test subjects in volunteer tests. The computation time when simulating a maneuver of approximately 4 seconds, resulted in a computation time of 0.7 seconds for both models, which allows for efficient computation of an extensive number of pre-crash maneuver simulations for analysis of occupant kinematics.

Keywords: INTEGRATED SAFETY, KINEMATICS, HUMAN BODY MODEL, PRE-CRASH MANEUVER, KINEMATIC MODEL, OCCUPANT

Preface

This Master's Thesis was carried out during the spring semester of 2018, in the department of Mechanical and Maritime Sciences (M2), div. of Vehicle Safety, at Chalmers University of Technology. The project was proposed by Volvo Cars and was executed at their facilities in Gothenburg. The work was supervised by Alexandros Leledakis and Linus Wågström at Volvo Cars Safety Centre, and by Alexey Geints at dept. of Mathematical Sciences, Chalmers. The examiner was professor Robert Thomson at M2, dept. of Vehicle Safety at Chalmers.

Acknowledgements

We would like to begin by thanking our supervisors at Volvo Cars Safety Centre (VCSC), Alexandros Leledakis and Linus Wågström, for giving us the opportunity to execute this very interesting Master's Thesis. Your guidance, creative ideas, and enthusiasm have been important factors in our work. We also thank our supervisor Alexey Geynts, dept. of Mathematical Sciences at Chalmers, for sharing your extraordinary knowledge in mathematics and physics with us. Our meetings with you have been truly inspiring and essential for the development of the model. A big thank you to Robert Thomson at M2, div. of Vehicle Safety at Chalmers for being an inspiring and helpful examiner of our project. Thank you Johan Davidsson at M2, div. of Vehicle Safety at Chalmers, for sharing data from volunteer maneuver studies with us. We would also like to thank Lotta Jakobsson at VCSC, for your meaningful feedback on our work and the report. Furthermore, we would like to thank Jonas Östh, Katarina Bohman, Mats Landervik, Jacob Wass, Magdalenda Lindman, and Catherine Lef at VCSC for providing us with useful information and answers to our many questions. At last, thank you to all master's thesis students and colleagues at VCSC for making the time of our thesis work truly enjoyable.

Oscar Cyrén and Sofia Johansson, Gothenburg, June 2018

Nomenclature

CAS	Collision avoidance systems
CoG	Center of gravity
Corridor	Statistical region containing the mean, the mean plus one standard deviation and the mean minus one standard deviation of a dataset
Displacement	The distance from the initial to the current position of a point in a dynamic event
EMG	Electromyography, i.e. a method for measuring muscle activity
ERR	Electrical reversible retractor, i.e. seat belt pre-tensioner activated during evasive events
FE	Finite element, i.e. a numerical method for solving problems of engineering and mathematical physics
HBM	Human body model
Kinematics	The study of motion, i.e. the velocities and accelerations of particles, bodies and system of bodies of finite dimension, without reference to its causes (forces, friction etc.)
Lateral	The right-left direction of the car
Longitudinal	The forward-rear direction of the car, i.e. the driving direction
Maneuver	A move, or a series of moves, performed to control a vehicle, here referring to a braking and/or steering action
Model	A representation of a dynamic system, as described by mathematical concepts
Occupant	A person travelling in a car, either a driver or a passenger
Pre-crash	The state in time before a crash, when a collision is unavoidable yet possible to mitigate
PSO	Particle swarm optimization
RMSE	Root mean square error
Response	The behaviour of a dynamic system during the influence of external forces
Standard belt	A standard configuration of the seat belt, without pre-crash triggered systems
T1	The first vertebrae of the thoracic segment of the human vertebral column, counting from the neck and downward
Tuning	Setting of model parameters so that the modeled system response resembles the real system response with minimal difference
VCSC	Volvo Cars Safety Centre

Contents

1| Introduction

Road traffic crashes account for more than 1.25 million deaths each year world wide, and it is the leading cause of death for people in the ages 15-29 (World Health Organization, 2015). Moreover, between 20 to 50 million people suffer non-fatal injuries, many resulting in disability and life-long consequences for the injured. Among the fatalities caused by road traffic accidents, 31% are car occupants. In the European Union (EU) alone, over 26.000 people were killed in road traffic crashes in 2015, among them 46% were killed in a car (European Road Safety Observatory, 2017). For every person killed in road traffic crashes in EU there is an estimate of up to 4 permanently disabling injuries such as serious brain damage or spinal cord damage, 8 serious injuries and 50 minor injuries (World Health Organization, 2015). As motorization is increasing world wide each year, the number of fatalities from road traffic crashes would be expected to increase. However, the number of fatalities has plateaued since 2007 as a result of the progress in vehicle and traffic safety, mostly due to development of safer infrastructure, improvement of passive safety, and implementation of collision avoidance systems (CAS) in cars (World Health Organization, 2015).

During the past fifteen years, considerable effort has been invested in the development of collision avoidance systems, and today most car manufacturers offer this type of technology (Aust, Jakobsson, Lindman, & Coelingh, 2015). These systems function to avoid or mitigate a crash by warning the driver and/or intervening in the driving situation. The intervening evasive maneuvers lead to occupant displacement (Schoeneburg, Baumann, Fehring, Ag, & Cars, 2011; Östh, Ólafsdóttir, Davidsson, & Brolin, 2013; Ólafsdóttir, Östh, Davidsson, & Brolin, 2013), thus the occupants may be out of their initial positions when facing a potential crash. Consequently occupant safety evaluation needs to be performed, not only for the crash phase, but also for the events leading up to the crash (Schoeneburg et al., 2011).

1.1 Background

An investigation of frontal crashes in the GIDAS (German In-Depth Accident Study) database demonstrated the proportion of frontal crashes that contained a braking maneuver prior to the crash with a deceleration greater than 4 m/s^2, i.e. harsh braking (Schoeneburg et al., 2011). In 49% of the cases, braking at or above this level was found. In the remaining cases, no braking or insufficient braking was prevalent. Given that most car manufacturers today equip their cars with CAS (Aust et al., 2015), which implies that the car will brake for every case when the driver is not acting sufficiently, an increasing number of crashes will be preceded by at least one type of mitigating maneuver. CAS operate by warning the driver and/or intervening in a critical driving situation, through applying braking and/or steering interventions to avoid or mitigate a crash (Aust et al., 2015). The systems act based on environmental data obtained by radar, LiDAR (laser), cameras and other sensors. For example, a retrospective study (Isaksson-Hellman & Lindman, 2016) showed a reduction of rear-end frontal collisions by 37% for cars equipped with forward collision warning with autobrake and adaptive cruise control. Another retrospective study (Cicchino, 2016) showed injurious rear-end frontal crashes were reduced by 42% for cars equipped with forward collision warning and emergency brake. Furthermore, a

reduction of 10% of the impact speed has been predicted to reduce the risk of occupant fatalities by 30% and the risk of having a severe injury by 19% (Krafft, Kullgren, Lie, Strandroth, & Tingvall, 2009).

The evasive maneuvers expose occupants to longitudinal, lateral, and rotational accelerations (Schoeneburg et al., 2011). As a result, occupant displacements can arise and shift the occupants out of their initial positions when facing a potential crash, and alter their positions relative to the restraint systems of the car. This effect has been found in several volunteer studies when subjects have been exposed to different evasive maneuvers in the magnitude of 1 g (Östh et al., 2013; Ólafsdóttir et al., 2013; Huber, Kirschbichler, Prüggler, & Steidl, 2015; Ghaffari et al., 2018). Occupant head and chest excursion as a result of the evasive maneuvers was found considerable in all tests. A simulation analysis of the influence of evasive maneuvers (Antona, Ejima, & Zama, 2011) concluded that maximum chest deflection and seat belt force were increased if the crash was preceded by a braking maneuver, because of the obtained forward motion of the occupant. Another volunteer study that investigated the effect of evasive maneuvers on volunteers (Mages, Seyffert, & Class, 2011), demonstrated that occupants were realigned relative to the restraint systems. For example shoulder belt slip-off was present in lateral acceleration, and longitudinal deceleration displaced the occupant's head and chest nearer to the air-bag inflation area. Subsequent crash simulations showed negative effects on the occupant injury outcome. An existing solution for reducing the motion of the occupant during evasive maneuvers, is to activate the seat belt force early on by applying the so called electrical reversible retractor (ERR) function (M. Björklund, VCSC, personal comm., May 2018). Studies have shown that reducing the slack of the seat belt during evasive maneuvers, as performed by ERR, reduces occupant displacement (Ólafsdóttir et al., 2013; Mages et al., 2011).

Assuming that a crash is unavoidable, the seconds preceding the impact are referred to as the pre-crash phase. Considering the increasing number of cars equipped with CAS, there has been an increasing interest in research and among car manufacturers to investigate occupant safety during the pre-crash phase. Therefore methods and tools for evaluating the occupant pre-crash kinematics are needed to gain knowledge of the holistic view on the occupant safety. In general, full-scale anthropomorphic test devices (ATD), or crash test dummies, are used when performing physical and virtual simulations of crashes. They can provide data for analysis of impacts and injury outcome of a crash, and restraint systems can be evaluated with respect to the interaction with the occupant. However, ATDs cannot be applied to accurately reproduce human occupant kinematics during evasive maneuvers since they contain significant differences in the mechanics compared to humans, i.e. humans are less stiff and more viscoelastic (Muggenthaler, Adamec, Praxl, & Schönpflug, 2005; Östh, 2014). Furthermore, in the pre-crash phase, muscle activation has a considerable influence on occupant kinematics due to lower loads and longer duration than for the crash phase (Östh et al., 2013). Valuable tools for simulating pre-crash occupant kinematics are Human Body Models (HBM), which are highly detailed finite element models (Östmann & Jakobsson, 2016). Besides kinematics, these models provide insight of injury mechanisms and injury criteria down to a tissue level. More recent versions of HBM, such as the SAFER THUMS v9.0.1 (Iraeus, Davidsson, & Brolin, 2017), incorporate muscles to account for muscular activity during the maneuvers. The high level of detail in the HBM requires extensive computer capacity[1].

[1]Simulation of a 2000 ms pre-crash and 150 ms crash with the SAFER THUMS v9.0.1 (the HBM used

Evasive maneuvers can include steering- and braking interventions in different order, and can vary in duration, initial speed, and accelerations. Therefore an extensive number of maneuvers need to be considered when evaluating pre-crash safety. Furthermore, occupants can voluntarily apply muscle tension during maneuvers with the magnitude of around 1 g, in order to reduce motion (Östh et al., 2013). As a result, muscle activity of the occupant has a major influence on occupant kinematics, and the response will vary for every occupant that is exposed to a particular maneuver. Hence, at Volvo Cars Safety Centre (VCSC) there is an need for a large number of pre-crash maneuver simulations, and for that reason the use of the HBMs are limited. Moreover, it is of interest to study how varying muscle activity among occupants affect the kinematics. These purposes call for a more computationally efficient model.

1.2 Aim

The aim of this thesis is to develop a simplified occupant model that can be used to predict the kinematics of the occupant head centre of gravity (CoG), i.e. longitudinal and lateral displacement, during pre-crash maneuvers. The model needs to be computationally efficient, meaning a simulation time of less than a few seconds. Furthermore, the model is aimed to include the standard belt configuration as well as the ERR belt configuration.

1.3 Limitations

The kinematic model is limited to computing occupant kinematics in the terms of longitudinal- and lateral head CoG (and T1) displacement. The model is only aimed for simulating the response of evasive maneuvers during the pre-crash phase. The model only considers the upper body of the occupant, and the lower body is neglected. The model includes restraint systems such as the seat and the seat belt, however they are approximations of the real systems. The model is designed to simulate a front seat passenger, and a driver model is suggested. The model kinematics represent those of nine male test participants, and does not represent any specific percentile in the population distribution.

at VCSC) using a rigid sled model with full interior takes 6.8 days on 240 CPUs (J. Östh, VCSC, personal comm., 28^{th} of May, 2018).

2| Theory

In order to give a better understanding of the underlying theories to the methods applied, the presented results, and the discussions brought up in this thesis, some theoretical foundations are provided in the following sections.

2.1 Evaluation of pre-crash safety

Human body models (HBMs) are tools that are used to study human response in pre-crash and in-crash simulations. There are two types of HBMs of which the first is the FE model type, for which the anatomical structures are split into smaller elements that are defined by nodal points, for which approximate solutions to the ruling differential equations are computed. The other type is the multibody dynamic model (MB), for which the human body is modeled using flexible and rigid bodies that are connected by kinematic joints. The latter has been used primarily to simulate human kinematics in crashes, however, its' purpose has lately been exchanged by the FE model as it can predict the kinematics as well (Östh, 2014). FE HBMs have improved anthropometry compared to the MB model, and incorporate models of human tissue which enables a more human-like response in simulations. This provides the possibility to study for example kinematics and injury outcome down to a tissue level (Östmann & Jakobsson, 2016). As of today, several FE HBMs have been developed. SAFER Vehicle and Traffic Safety Research Centre at Chalmers have been executing further development of the THUMS v3[1] model, which represents a 50^{th} percentile male. The updated version of the model, SAFER THUMS v.9.0.1 here referred to as the SAFER HBM (Iraeus et al., 2017), includes models of muscles that account for muscle responses to enable human-like behavior during simulations of evasive maneuvers. The muscle models are controlled using feedback control, i.e. stabilizing muscle activation is provoked as a response to external forces (Östh, 2014). Figure 2.1 demonstrates the SAFER HBM in its nominal seated position. The model has a high level of detail, and contains around 2 million finite elements. Simulation of a 2000 ms pre-crash and 150 ms crash sequence using the SAFER HBM on a rigid sled with full interior takes approximately 7 days[2] (J. Östh, VCSC, personal comm., 28^{th} of May, 2018).

At VCSC, a simplified tool for evaluating occupant pre-crash maneuver kinematic response has been developed. It can compute occupant head displacements in the longitudinal and vertical direction as an effect of pre-crash braking maneuvers.

[1] Initially presented by Iwamoto *et al.* (Iwamoto et al., 2002), and later improved by Toyota
[2] With the use of 240 CPUs

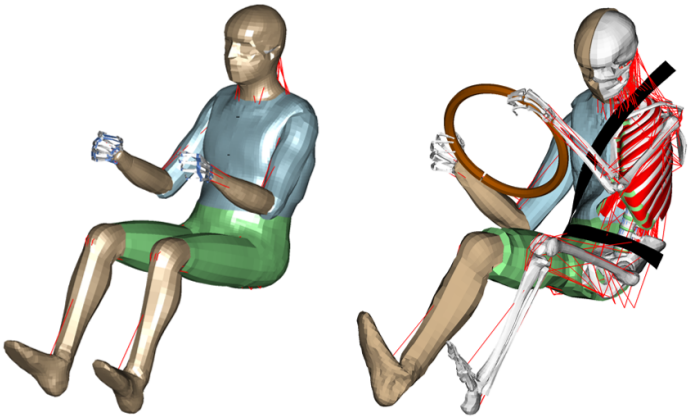

Figure 2.1: The SAFER THUMS v9.0.1 model in nominal position (left), and interior view during impact (right) where the red lines represent muscles. Images provided by J. Östh, May 2018.

Feedback originating in various sensory organs is transmitted by afferent nerves and processed by the brain or spinal cord to generate motor commands actuated by skeletal muscles. Depending on the task and external loading condition, the contribution from the various input signals originating from the visual, vestibular and somatosensory systems are modulated by the central ner- vous system (CNS) (Keshner, 1995; Peterka, 2002; Schouten et al., 2008) and integrated

2.2 Occupant kinematics in maneuvers

When external loads are acting on the body, postural control processes are excited by feedback from different sensory organs. These signals are then processed by the brain or the spinal cord to initiate motorized movements that are created by the skeletal muscles, in order to maintain stability and equilibrium (Peterka, 2002). The low magnitude linear- and rotational accelerations, as well as the long duration of evasive maneuvers, apply external loads on the occupant, which excite the occupant to apply voluntary tensing of muscles in order to reduce motion (Ólafsdóttir, 2017). As a result, muscle activation will have a strong influence on the occupant kinematics in this phase (Östh et al., 2013). In maneuver tests where volunteers have been asked to alternate muscle states, relaxed or tensed, when exposed to longitudinal and lateral maneuvers have shown that bracing during maneuver loading results in reduced head- and chest displacements for both passengers and drivers (Van Rooij, Elrofai, Philippens, & Daanen, 2013; Ejima, Ono, Holcombe, Kaneoka, & Fukushima, 2007). Hence the kinematics, i.e. the displacement for different body parts, will vary between occupants depending on the level and timing of muscular contraction.

Drivers respond differently to evasive maneuvers than passengers, since drivers have the option of bracing against the steering wheel to assist in reducing the forward and lateral motion (Ólafsdóttir et al., 2013). Results of volunteer tests of autonomous braking maneuvers, performed for the passenger position restrained by a standard seat belt (Ólafsdóttir et al., 2013) versus the driver position (Östh et al., 2013) showed significant differences between them. The mean longitudinal head displacement for the passengers was 176% of that of the driver, and the mean chest displacement for the passengers was 154% of the

driver's chest displacement[3]. Furthermore, volunteer tests have shown no sliding of the pelvic region against the seat, as well as minor rotation of the torso around the vertical axis during braking maneuvers primarily, due to the asymmetry of the three point seat belt (Huber et al., 2015).

Head posture is controlled by the vestibular organ in the inner ear, which senses head linear- and rotational acceleration and orientation (Angelaki & Cullen, 2008). Together with muscle spindles in the muscles, which sense muscle lengthening (Keshner, 2009), activation of the muscles in the neck are controlled in order to maintain an upright posture of the head. Furthermore, the visual system also influences the head's posture as stabilizing the gaze is of high priority (Wylie, 2009), i.e. if the head is rotated the occupant will by reflex attempt to maintain the head horizontal relative to the visual direction. Figure 2.2 shows an example of the head kinematics for a braking maneuver. The top row represents the behavior when the occupant model has active muscles, i.e. the gaze is maintained horizontal, and the bottom row represents when the muscles are passive (Östh, Brolin, Carlsson, Wismans, & Davidsson, 2012), i.e. there is a distinct rotation of the head. When subjected to lateral accelerations and rotations, the occupant will maintain an upright position of the head by laterally flexing the cervical spine (Muggenthaler et al., 2005). For initial movement towards the door, the occupant may also react by laterally flexing the neck further for protection from proximity with the B-pillar (Huber et al., 2015).

Occupant behavior during maneuvers has been studied using volunteers as occupants, and by exposing them to simulated evasive maneuvers. As stated in section 2.1, FE HBMs are being developed to enable evaluation of human response during the pre-crash and the crash phase. To have the models replicate human-like behavior during pre-crash simulations, in-car volunteer tests undergoing evasive maneuvers have been performed in order to provide data for tuning and validating the models (Östh et al., 2013; Ólafsdóttir et al., 2013; Ghaffari et al., 2018), see section 3.3. The tests have also served for studying human motion during maneuvers, justifying the need for further investigation and improvement for safety during the pre-crash phase (Schoeneburg et al., 2011).

[3]Calculated by comparing the maximum mean head- and chest displacement for volunteers in the tests, including 11 male and 9 female subjects (the same subjects were used for both studies) where passenger mean head displacement = 195mm, driver mean head displacement = 111mm, passenger mean chest displacement = 109.6mm, and driver mean chest displacement = 71mm.

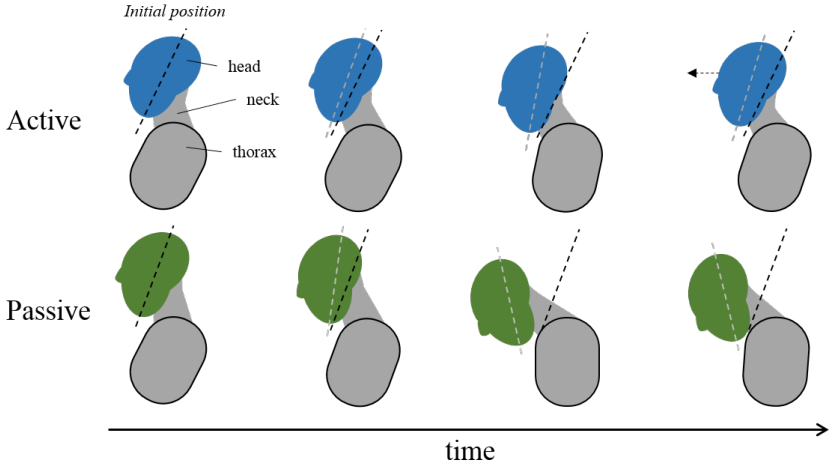

Figure 2.2: Head kinematics of the occupant model during a braking maneuver around 1 g, when restrained by a three point seat belt.

2.3 The three-point seat belt

The three point seat belt is the primary life-saving car safety invention (Håland, 2006), and it consists of several subsystems that can be activated to improve its' function for critical situations such as crashes and evasive maneuvers. The functions that are of importance in this context are stated below.

A significant part of the seat belt is the *retractor* (Håland, 2006), which is normally positioned in the lower part of the B-pillar. The seat belt webbing originates from the retractor and it is pulled back into the retractor using a spool mechanism to reduce excessive length and eliminate slack to give a snug fit across the thorax and shoulder. Besides retracting the seat belt, the retractor includes several other mechanisms that help with injury reduction. The *retractor locking mechanism* typically locks the seat belt pay-out when the vehicle decelerates or obtains a lateral acceleration above 0.45 g[4]. The function locks the shoulder belt pay-out early in a crash, which restricts the occupants' continued motion in any direction (Håland, 2006). The locking mechanism is also activated with regards to the belt pay-out rate. Another mechanism of the seat belt is the *retractor pre-tensioner*. This is a pyrotechnical pulling mechanism that, in the course of a few milliseconds, rewinds the retractor spool during a crash, which reduces remaining seat belt slack across the thorax up to 200 mm. This action fixes the occupant into the backrest during the crash, and as a result, the available displacement relative the interior is increased (Håland, 2006).

When the retractor locks the belt during an evasive maneuver, a force is applied on the occupant. However, the force is delayed by the so called *"film spool effect"* (Svensson, 1978). It is caused by a slack in the seat belt retractor roll, as the belt is not tightly rolled to begin with. At locking, the seat belt continues to pay-out as it tightens around the retractor roll. This affects the seat belt force such that when the retractor locks, the applied force on the occupant is very low up to the point when the slack has been tightened, after which the force increases rapidly. This effect contributes to an extended chest and head excursion (Svensson, 1978).

[4] $g = 9.81$ is the gravitational acceleration in m/s^2

2.3.1 Seat belt pre-crash pre-tensioning

During evasive maneuvers additional occupant protection can be achieved by initiating restraints early on to ensure occupants into an upright position when facing the potential crash (Östmann & Jakobsson, 2016). This can be attained by applying a pre-tensioning of the seat belt during the maneuver, using an electrical reversible retractor (ERR) system. The system consists of an electrical motor that is coupled to the retractor that can pull the belt with a relatively low force, typically 100-300 N, during the evasive maneuver. The system is triggered by external sensory information, for example by radar-, accelerometer- and camera signals, the same sensors that help trigger CAS, such as emergency braking. The action of the ERR will reduce the slack of the belt, and consequently the occupant displacement is reduced (Ólafsdóttir et al., 2013; Östh et al., 2013). As opposed to the pyrotechnical pre-tensioner that is deployed during a crash, the ERR applies a significantly lower force magnitude and a slower webbing reduction. It is also reversible which means it can be activated multiple times. The ERR and the pyrotechnical pre-tensioner serve for different situations, and using current technology one system cannot replace the other.

The benefit of having an ERR seat belt was demonstrated in volunteer studies with passengers (Ólafsdóttir et al., 2013), where the effect of initiating seat belt pre-tensioning of 170 N 200 ms prior to a braking maneuver was investigated. When induced to steady state braking, the head displacement was reduced by 66 mm for males and 81 mm for females, and T1 displacement was reduced by 51 mm for males and 81 mm for females using the pre-tensioned configuration. The resulting head and T1 displacement corridors, i.e. mean $\pm$ one standard deviation, in Figure 2.3, demonstrate how the retraction of webbing in the pre-tensioned belt pulls the occupant backward into the seat directly after the activation (dotted line). Furthermore, as found in EMG data recordings, muscle activity is initiated earlier when having an ERR belt (Ólafsdóttir et al., 2013; Östh et al., 2013). Similar experiments with passenger volunteers were performed for lateral maneuvers (Mages et al., 2011), where ERR activation occurred 120 ms prior to the maneuver with a force of 110 N. The results were, for lateral maneuvers with initial direction right versus left, that mean lateral head displacement was reduced by 9% and 15% respectively, and the mean lateral chest displacement was significantly reduced by 44% versus 46%. The study concluded that the reduction of lateral chest displacement could reduce the risk of shoulder belt slip-off.

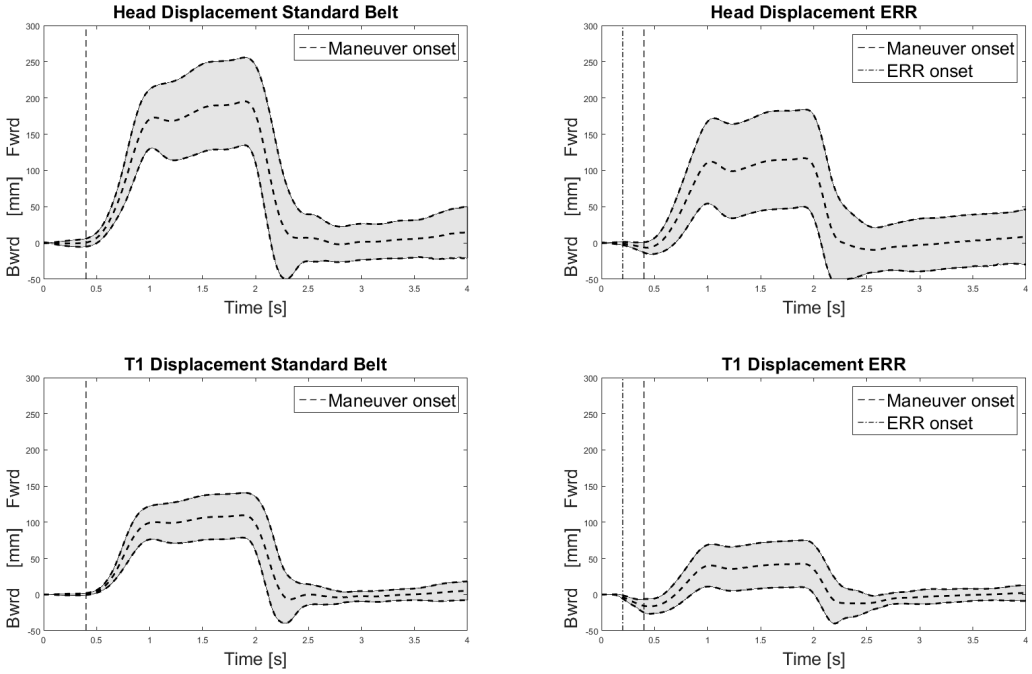

Figure 2.3: Head and T1 longitudinal displacements of volunteers subjected to a braking maneuver, using a standard belt and a pre-tensioned belt configuration. The grey area represents the mean ± one standard deviation of the displacements. Data from Olafsdottir *et al.*, 2014.

2.4 Vehicle dynamics

In this section some relevant concepts of vehicle dynamics are explained, based on the standard terminology of SAE international vehicle dynamics terminology J670 (Sayers, 1996). To show the vehicle orientation in space three angles are used, the *roll angle* ϕ, *pitch angle* θ, and *yaw angle* ψ. The *roll angle* is the angle of rotation around the longitudinal axis, measured in a counterclockwise direction. The *pitch-* and *yaw angle* are the angles of rotation around the lateral and vertical axes respectively, see Figure 2.4.

The focus for this work will lie on planar motion, which will be the case for future application of the model. Planar motion is whenever longitudinal and lateral accelerations and yaw-angle, -velocities, and -acceleration are sufficient to describe the motion of the vehicle. Roll angle, pitch angle and vertical motion will therefore be disregarded. The coordinate system has a Z-up orientation, i.e. the vertical axis (*z-axis*) originates from the vehicle CoG with positive direction pointing upwards. The longitudinal axis (*x-axis*) points forward in the direction of travel and the lateral axis (*y-axis*) points to the left from the vehicle CoG (Sayers, 1996).

Now, consider the situation of a vehicle rapidly approaching another slower vehicle from behind. The first vehicle has to avoid a collision by braking and turning left. For simplicity, assume a rigid vehicle, i.e. that the distances between points in the vehicle body remain constant, and that the road is horizontal. The motion can then be assumed to take place in the 2-dimensional plane spanned by the x- and the *y-axis*. The motion can be described using the longitudinal acceleration, the lateral accelerations and the yaw angle. When

the vehicle brakes, a negative acceleration (deceleration) will be perceived in the vehicle, which slows it down. In the same manner, when the vehicle turns and changes direction, a lateral acceleration will be perceived in the vehicle. By describing the motion only using the longitudinal and lateral acceleration, one can visualize the motion as pure translation in the horizontal plane. By adding the rotation, i.e. the *yaw angle* about the *z-axis*, the motion can be clearly defined (Jazar, 2017).

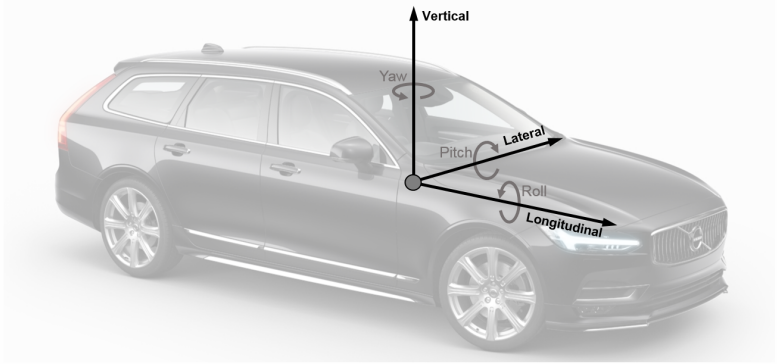

Figure 2.4: Vehicle coordinate axes and orientation. Vehicle image courtesy of Volvo Car Corporation.

2.5 Mathematical modeling

In this section, mathematical techniques and concepts are presented, including techniques such as *Lagrange's equation of motion* and concepts such as *generalized coordinates*, *generalized forces* and consequences of an *accelerating reference frame*.

2.5.1 Equations of motion

One fundamental concept in classical mechanics is the one of a particle. A particle is a body whose size and shape can be neglected when describing its motion in contrast to a body which has a propagation in space, whose inertia needs to be accounted for. One could for instance consider the earth as a particle when observing its motion around the sun, but not when considering earth's rotation around its axis. The position of a particle can be described by a position vector $\boldsymbol{r}$ with components in Cartesian coordinates, its *velocity* ($\boldsymbol{v} = d\boldsymbol{r}/dt$), and its *acceleration* ($\boldsymbol{a} = d^2\boldsymbol{r}/dt^2$).

The number of independent quantities needed to uniquely determine the position of a system of one or more particles are called *degrees of freedom* (DoF), and for a system of N particles described in the Cartesian system, the DoF are $3N$, i.e. 3 for the *x, y, z* coordinates times N individual particles. These quantities are not necessarily restricted to the Cartesian coordinates as they can be described using any reference system that is convenient for describing the system at hand. Any quantities defining the positions of the system are called generalized coordinates, and their time derivatives are called generalized velocities, hereafter referred to as $\boldsymbol{q}$ and $\dot{\boldsymbol{q}}$ respectively.

If all coordinates and their time derivatives, i.e. velocities, are specified simultaneously it means that the state of the system is completely determined and that the motion can be calculated. This means that one can mathematically and uniquely calculate the

accelerations $\ddot{\boldsymbol{q}}$ at a given time instant t, given the velocity $\dot{\boldsymbol{q}}$ and the position $\boldsymbol{q}$ at that instant. The relations are called the *equations of motion* and are second order differential equations for $\boldsymbol{q(t)}$. By solving these differential equations the trajectory of the system can be determined (Landau & Lifshitz, 1976).

2.5.2 Principle of Least Action and Lagrange's Equations

The *Principle of Least Action* is the most general formulation for describing the motion of a mechanical system. The starting point is the *Action* of a system, here denoted S. The *Action* is defined as the integral between two instants of time t_1 and t_2 of the *Lagrangian* function denoted $\mathcal{L}(\boldsymbol{q}, \dot{\boldsymbol{q}}, t)$, which is defined as the difference in the *kinetic energy* and the *potential energy*, $\mathcal{L} = T - V$. The time instants correspond to two sets of values of coordinates, $\boldsymbol{q^{(1)}}$ and $\boldsymbol{q^{(2)}}$, and the *Principle of Least Action* is the condition such that the system moves between $\boldsymbol{q^{(1)}}$ and $\boldsymbol{q^{(2)}}$ which yields that the integral

$$S = \int_{t_1}^{t_2} \mathcal{L}(\boldsymbol{q}, \dot{\boldsymbol{q}}, t) dt \tag{2.1}$$

is minimized.

Now, for simplicity, assume that a system has one DoF. To derive the differential equations which minimize the integral in Eq.(2.1), the function $q(t)$ has to be determined. Let $q = q(t)$ be the function which minimizes S. Since S is minimized by q, S is increased if $q(t)$ is replaced with

$$q(t) + \delta q(t) \tag{2.2}$$

where $\delta q(t)$ is arbitrary small everywhere in the interval $[t_1, t_2]$. This function, $\delta q(t)$, is called the *variation* of the function $q(t)$. Since all functions in Eq.(2.2) must take the values of $q^{(1)}$ and $q^{(2)}$ for $t = t_1$ and $t = t_2$ respectively, this yields

$$\delta q(t_1) = \delta q(t_2) = 0 \tag{2.3}$$

The change in value of S when varying $q(t)$, by adding $\delta q(t)$ and expanding the resulting integrand in powers of $\delta q(t)$ and $\delta \dot{q}(t)$, yields that the *Principle of Least Action* can be expressed as

$$\delta S = \delta \int_{t_1}^{t_2} \mathcal{L}(q, \dot{q}, t) dt = 0 \tag{2.4}$$

or

$$\delta S = \int_{t_1}^{t_2} (\delta T - \delta V) dt = 0 \tag{2.5}$$

which often is referred to as the mathematical statement of *Hamilton's principal*.

If the variation is carried out in Eq.(2.4) this yields

$$\delta S = \int_{t_1}^{t_2} \left(\frac{\partial \mathcal{L}}{\partial q} q + \frac{\partial \mathcal{L}}{\partial \dot{q}} \dot{q} \right) dt = 0 \tag{2.6}$$

Here $\dot{q} = dq/dt$, and by integrating Eq.(2.6) by parts yields

$$\delta S = \left[\frac{\partial \mathcal{L}}{\partial \dot{q}} \delta q \right]_{t_1}^{t_2} + \int_{t_1}^{t_2} \left(\frac{\partial \mathcal{L}}{\partial q} - \frac{d}{dt} \frac{\partial \mathcal{L}}{\partial \dot{q}} \right) \delta q dt = 0 \tag{2.7}$$

From Eq.(2.3) it is observed that the first term in Eq.(2.7) is zero. What is left is an integral which will vanish for all values of $\delta q(t)$ and hence this is only true if the integrand is equal to zero,

$$\frac{d}{dt}\left(\frac{\partial \mathcal{L}}{\partial \dot{q}}\right) - \frac{\partial \mathcal{L}}{\partial q} = 0 \tag{2.8}$$

For a system which has more than one DoF, all functions $q_i(t)$, $i = 1, 2, \ldots, N$ must be varied independently. This procedure is done analogously to the method described above, and will yield the equations

$$\frac{d}{dt}\left(\frac{\partial \mathcal{L}}{\partial \dot{q}_i}\right) - \frac{\partial \mathcal{L}}{\partial q_i} = 0 \qquad \text{for} \quad i = 1, 2, ..., N \tag{2.9}$$

In mechanics these equations are the *Lagrange's equations*. If the Lagrange's equations for a given system can be determined, then Eq.(2.9) gives the relation between accelerations, velocities and positions. These are the *equations of motion* (Landau & Lifshitz, 1976).

2.5.3 Generalized forces

One assumption in the derivation of Eq.(2.9) was that the virtual work could be expressed as a variation of the potential energy, V. This is not always the case, and if some of the forces acting on the system are not derivable from the potential energy, there is a possibility to divide the virtual work into two parts. The first part is the *conservative virtual work*, denoted δW^c, which, as the name suggests, is done by the conservative forces derivable from a potential V. One such force may be the force induced on the system by the gravity of the earth. The second part is the *non-conservative virtual work*, denoted δW^{nc}, which is done by the non-conservative forces applied on the system.

Non-conservative forces applied to the system of particles with mass m_j, $j = 1, 2, \ldots, m$, can be incorporated to the Lagrange's Equations of motion by the means of generalized forces. The generalized forces are obtained via the formulation of *virtual work*. The virtual work of the applied forces, $\boldsymbol{F}_j$, on the particles with mass m_j, is given by

$$\delta W = \sum_{j=1}^{m} \boldsymbol{F}_j \cdot \delta \boldsymbol{r}_j \tag{2.10}$$

where $\boldsymbol{r}_j$ is the position vector of each particle and $\boldsymbol{r}_j$ is a function of the generalized coordinates $\boldsymbol{q}_i$, $i = 1, 2, \ldots, N$ i.e. $\boldsymbol{r}_j(q_1, q_2, ..., q_N)$. The *virtual displacement* $\delta \boldsymbol{r}_j$ is given by

$$\delta \boldsymbol{r}_j = \sum_{i=1}^{N} \frac{\partial \boldsymbol{r}_j}{\partial q_i} \delta q_i, \quad for \quad j = 1, 2, \ldots, m \tag{2.11}$$

where δq_i is the virtual displacement of the generalized coordinate. This yields the virtual work as follows

$$\delta W = \boldsymbol{F}_1 \cdot \sum_{i=1}^{N} \frac{\partial \boldsymbol{r}_1}{\partial q_i} \delta q_i + \ldots + \boldsymbol{F}_m \cdot \sum_{i=1}^{N} \frac{\partial \boldsymbol{r}_m}{\partial q_i} \delta q_i \tag{2.12}$$

By collecting the coefficients δq_i this can be written as

$$\delta W = \sum_{j=1}^{m} \boldsymbol{F}_j \cdot \frac{\partial \boldsymbol{r}_j}{\partial q_1} \delta q_1 + \ldots + \sum_{j=1}^{m} \boldsymbol{F}_j \cdot \frac{\partial \boldsymbol{r}_j}{\partial q_N} \delta q_N \tag{2.13}$$

where the expression for the generalized force is identified as

$$Q_i = \sum_{j=1}^{m} bmF_j \cdot \frac{\partial \boldsymbol{r}_j}{\partial q_i}, \quad i = 1, \ldots, N \tag{2.14}$$

The virtual work of the system particles can now be stated as

$$\delta W = Q_1 \delta q_1 + \ldots + Q_N \delta q_N \tag{2.15}$$

Note that Q_i need not necessarily have the dimension of force, just as the generalized coordinates need not have the dimension of length but can be polar or spherical coordinates. For example, Q_i can be torques τ_i, but in that case the variation term δq_i must be a differential angle, since $\tau_i \delta q_i$ must always have the dimension of work.

By dividing the virtual work into one conservative part and one non-conservative part, this yields

$$\delta W = \delta W^c + \delta W^{nc} = -\delta V + \sum_{i=1}^{N} Q_i^{nc} \delta q_i \tag{2.16}$$

where the conservative part of the virtual work, δW^c, can be expressed as the variation of the potential energy, $-\delta V$[5]. Recall the variation of the Lagrangian $\delta \mathcal{L} = \delta T - \delta V$, by substituting the expression in Eq.(2.16) into Eq.(2.5) this yields

$$\int_{t_1}^{t_2} \delta(T - V) dt + \int_{t_1}^{t_2} \sum_{i=1}^{N} Q_i^{nc} \delta q_i dt = 0 \tag{2.17}$$

Incorporating the definition of the Lagrangian, $\mathcal{L} = T - V$, this yields

$$\int_{t_1}^{t_2} (\delta \mathcal{L} + \sum_{i=1}^{N} Q_i^{nc} \delta q_i) dt \tag{2.18}$$

which by using the techniques in Eq.(2.4) to Eq.(2.9) gives the Lagrange's equations on the following form:

$$\frac{d}{dt}\left(\frac{\partial \mathcal{L}}{\partial \dot{q}_i}\right) - \frac{\partial \mathcal{L}}{\partial q_i} = Q_i^{nc} \qquad \text{for} \quad i = 1, 2, ..., N \tag{2.19}$$

(Stutts, 2017)

2.5.4 Rayleigh's dissipation function

One special and important case of a non-conservative force that can be derived from a potential, is the viscous damping force, which is often proportional to the velocity of a particle. This yields the form of the the damping along the x-direction

$$D_{fx} = -k_x v_x \tag{2.20}$$

The potential function for this force is called the *Rayleigh's dissipation function* and is defined, for a system of N particles, as

$$\boldsymbol{D} = \frac{1}{2} \sum_{i=1}^{N} (k_x v_{i,x}^2 + k_y v_{i,y}^2 + k_z v_{i,z}^2) \tag{2.21}$$

[5]Forces derivable from a potential are called conservative forces and a conservative force can be described as the negative gradient of a potential, i.e. $W = -\nabla V$, hence the minus sign on δV.

For a system with more than one DoF, the generalized damping forces corresponding to the generalized coordinate $\boldsymbol{q}$ are linear functions of the velocities

$$D_{f_i} = -\sum_{i=1}^{N} k_i \dot{q}_i \tag{2.22}$$

Hence it is clear that the partial derivative of the *dissipation function* is the damping force acting along the generalized coordinate q_i

$$D_{f_i} = -\frac{\partial \boldsymbol{D}}{\partial \dot{q}_i} \tag{2.23}$$

In a reference system with generalized coordinates $\boldsymbol{q}$, the Lagrange's equations with dissipation and generalized forces becomes:

$$\frac{d}{dt}\left(\frac{\partial \mathcal{L}}{\partial \dot{q}_i}\right) - \frac{\partial \mathcal{L}}{\partial q_i} + \frac{\partial D}{\partial \dot{q}_i} = Q_i^{nc} \qquad \text{for} \quad i = 1, 2, ..., N \tag{2.24}$$

Hence the functions $\mathcal{L}$ and D, as well as the generalized forces Q_i^{nc}, must be specified to obtain the Equations of motion of the system (Goldstein, Poole, & Safko, 2000).

2.5.5 Inertial and non-inertial reference frames

In classical mechanics, an inertial frame of reference is a frame of reference where Newton's laws of motions, $m\ddot{\boldsymbol{r}} = \boldsymbol{F}$ holds. This means that if the net forces acting on a body is zero, then the body is not accelerated, i.e. it is at rest or moving with constant velocity in a straight line. In contrast to this, a non-inertial reference frame is a frame of reference where Newton's laws appear to be violated. A non-inertial reference frame can be used when describing an object's motion within a specific reference frame that accelerates relative the inertial frame. Many problems require the use of non-inertial reference frames. For example, situations involving an occupant in an accelerating vehicle performing some kind of evasive manoeuvre. Consider the situation of a vehicle entering a left turn, or changing lane on the freeway with constant velocity. In the car, the passenger or driver experiences a force which seems to pull him or her towards the right. This is the *fictitious force* called the *centrifugal force*, which is required in order to explain the occupants' movement towards the right. When a non-inertial reference frame is used, this phenomena of fictitious forces can arise.

Now consider Figure 2.5 which describes an arbitrary general motion of a reference frame, (*x',y',z'*), relative to an inertial reference frame, (*x,y,z*). An arbitrary *general motion* refers to both the rotation of a frame, as well as translation of the origin of that frame. In Figure 2.5, $\boldsymbol{r}$ points to the origin of the accelerating frame, and $\boldsymbol{r'}$ is a position vector in the accelerating frame. To describe the motion of an object in the moving reference frame, i.e. the movement of the position vector $\boldsymbol{r'}$, the fictitious forces acting on the object must be accounted for. Newton's equation can be modified to accommodate these fictitious forces, and the new equation can be expressed as follows

$$m\frac{d^2\boldsymbol{r'}}{dt^2}\bigg|_M = \boldsymbol{F} - m\frac{d^2\boldsymbol{r}}{dt^2}\bigg|_I - m\frac{d\boldsymbol{\omega}}{dt}\bigg|_M \times \boldsymbol{r'} - 2m\boldsymbol{\omega} \times \frac{d\boldsymbol{r'}}{dt}\bigg|_M - m\boldsymbol{\omega} \times (\boldsymbol{\omega} \times \boldsymbol{r'}) \tag{2.25}$$

For the full derivation of this equation, see Appendix B. In Eq.(2.25), I and M refer to the *Inertial-* and *Moving* reference frames. $\boldsymbol{F}$ denotes loads directly applied to the

object, and $(d^2\boldsymbol{r}/dt^2)|_I$ is the acceleration of the reference frame. The three last terms $m(d\boldsymbol{\omega}/dt)|_M \times \boldsymbol{r'}$, $2m\boldsymbol{\omega} \times (d\boldsymbol{r'}/dt)|_M$, and $\boldsymbol{\omega} \times (\boldsymbol{\omega} \times \boldsymbol{r'})$ are the fictitious forces. These forces are called the *Euler force*, the *Coriolis force* and the *centripetal force* respectively, where $\boldsymbol{\omega}$ denotes the angular velocity of the moving reference frame (Greiner, 2003).

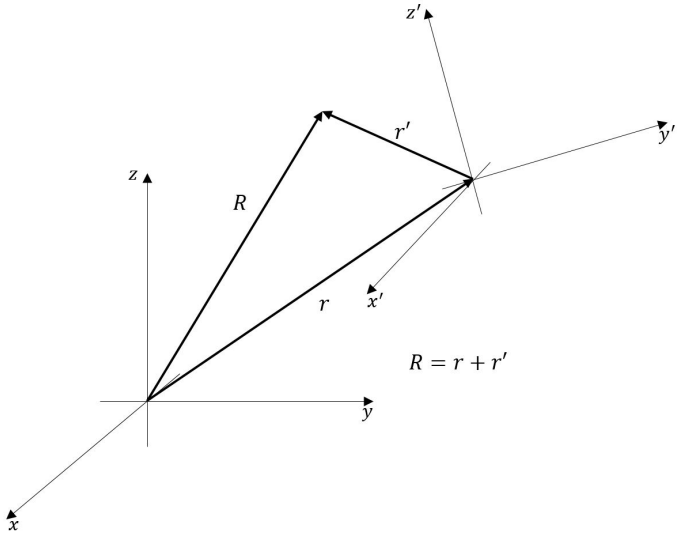

Figure 2.5: Relative position of the accelerating reference frame with coordinates (*x',y',z'*) and the inertial reference frame (*x,y,z*).

2.6 Model tuning

The simplified occupant model response will be dependent on a set of parameters. These parameters will be estimated such that the model output best fits the system which it is intended to describe, i.e. some reference data. The practice of finding these parameters is often referred to as *model tuning*. Other commonly used terms are *parameter selection* or *model fitting* (Steele & Werndl, 2016).

An objective function can be defined to find the best fit parameters for the model, i.e. in the optimization, an objective function is either minimized or maximized. This function measures the error of the model output compared to some existing reference data. A candidate for the objective function can be the root mean square error (RMSE) function, defined as

$$RMSE = \sqrt{\frac{1}{n}\sum_{t=1}^{n}(x_{1,t} - x_{2,t})^2} \tag{2.26}$$

where n is the number of data points, $x_{1,t}$ and $x_{2,t}$ are the model output and reference data respectively.

The RMSE computes the square root of the mean of the squared data point differences. This function provides a measure of the accuracy of the model which can be improved by finding better fitting parameters, referred to as minimizing the RMSE function (Fine & Boynton, 2009). The best fit parameters can be determined using an optimization algorithm which efficiently searches a defined search space, $[\boldsymbol{X}_{min}, \boldsymbol{X}_{max}]$, by minimizing the objective function. One such optimization algorithm which can be used for model

tuning or model fitting is Particle Swarm Optimization (PSO).

2.6.1 Particle Swarm Optimization

PSO is a so called evolutionary component technique developed by J. Kennedy and R. Eberhart, (1995). The original optimization algorithm was inspired by bird flocks to model simple social behavior systems. PSO builds on straightforward concepts, and requires only simple mathematical operators, making it computationally inexpensive both in terms of memory requirements and speed. This makes PSO a simple yet powerful optimization tool (Kennedy & Eberhart, 1995).

The algorithm is initialized with a population of random solutions. The population of solutions is referred to as a *particle swarm*. Each particle, or solution, has a position in an N dimensional solution space, which corresponds to value of the objective function. In the initialization phase, each particle is assigned with a randomized velocity and the particles are thereafter "flown" through the solution space to find an optimal solution. Each particle in the swarm is evaluated in the optimization problem objective function, and the individual particle keeps track of its own best position, i.e. the coordinates in the solution space which gives the optimum solution value. This value is called a fitness value, and its corresponding position is stored as p_{best} which is local to the particle itself. A global best value and position g_{best} is computed and stored as well, recognized as the best value obtained by any particle in the swarm (Kennedy & Eberhart, 1995).

2.6.2 Original PSO algorithm

The original algorithm for implementing PSO (Kennedy & Eberhart, 1995) is as follows:

1. Initialize the particle swarm with randomized positions and velocities on N dimensions in the search space.
2. For each particle in the swarm, evaluate the cost function of the optimization problem in N dimensions.
3. Compare each particle's fitness value to the stored p_{best}. If the current fitness value is better than p_{best}, then assign the new value to p_{best} and update the best position of the particle to the current position.
4. Compare the fitness value of each particle in the swarm to the globally best solution, g_{best}. If a particle has a better value then update g_{best} and its position to the fitness value and position of that particle.
5. Update the velocity v_{ij} and position x_{ij} of each particle j in the swarm i according to the following equations:

$$v_{ij}(t+1) = v_{ij}(t) + r_1 c_1 (p_{ij}(t) - x_{ij}(t)) + r_2 c_2 (p_g(t) - x_{ij}(t)) \tag{2.27}$$

$$x_{ij}(t+1) = x_{ij}(t) + v_{ij}(t+1) \tag{2.28}$$

   where t is the running index of the algorithm, r_1 and r_2 are two uniformly distributed random numbers in the interval $(0, 1)$, and c_1 and c_2 are acceleration constants. p_{ij} is the locally best position in p_{best}, and p_g is the globally best position so far in g_{best}.
6. Loop through step 2-5 until a stop criterion is met, for example a sufficiently good fitness value, or until a maximum number of iterations has been performed.

The exploration of the solution space is highly dependent on the computed velocity of the particles. Velocities that are too high may result in particles flying past good solutions. On the other hand, too low velocities may result in that the particle swarm insufficiently explores the solution space and gets trapped in local optima. Due to this, a parameter

called V_{max} is introduced and it is usually set to $10\% - 20\%$ of the dynamical range of the decision variable in each dimension. So if the computed velocity in Eq.(2.27) exceeds V_{max}, the velocity is set to V_{max}.

The acceleration constants, c_1 and c_2, in Eq.(2.27) are the *cognitive* and *social* acceleration coefficients respectively. They represent the weight that pulls each particle towards their own best solution p_{best} (*cognitive*) and the swarms best solution g_{best} (*social*). Adjustment of these two parameters change how far from the target area in the solution space particles are allowed to drift. High values results in rapid movement toward, or past, the target area while low values allow particles to drift far from the target before being "pulled" back. In early implementation of the PSO algorithm these constants were usually set to $c_1 = c_2 = 2.0$ (Eberhart & Shi, 2001).

2.6.3 Constriction factor

To improve the original PSO algorithm, and to ensure convergence of the optimizer, Eberhart and Shi (Eberhart & Shi, 2001) suggest to introduce a *constriction factor* called *Clerc's constriction factor* to the velocity equation of the original algorithm. This yields the modified velocity equation

$$v_{ij}(t+1) = \chi[v_{ij}(t) + r_1 c_1(p_{ij}(t) - x_{ij}(t)) + r_2 c_2(p_g(t) - x_{ij}(t))] \tag{2.29}$$

where χ is the *constriction factor* and is determined

$$\chi = \frac{2}{|2 - \phi\sqrt{\phi^2 - 4\phi}|}, \text{ where } \phi = c_1 + c_2. \tag{2.30}$$

When *Clerc's constriction factor* is used, one usually sets $c_1 = c_2 = 2.05$. A "rule of thumb" is also to limit the V_{max} parameter to X_{max}, i.e. the dynamic range of each decision variable.

2.6.4 PSO example

Consider a test function for optimization problems e.g. the Booth function, which is defined as

$$f(x, y) = (x + 2y - 7)^2 + (2x + y - 5)^2 \tag{2.31}$$

where the global minimum is located at $(x, y) = (1, 3)$. To find the global optimum one can implement PSO as follows

1. Define a search space, $x = [-10, 10]$ and $y = [-10, 10]$. Set the number of particles in the swarm $nPop$, and initialize the global fitness value as $g_{best} = \infty$ (for a minimization problem).
2. Initialize the PSO algorithm by randomly distribute the $nPop$ particles in the search space and assign a randomly chosen initial velocity to each particle.
3. Now compute the objective function value for each particle and store the position and fitness value in p_{best}.
4. Compare the fitness value of p_{best} to the global best fitness value in g_{best}. If the current p_{best} is better (lower) than the stored value g_{best} then update g_{best} with the new position and fitness value in p_{best}.
5. "Fly" the particles through the search space by updating the position and velocity of each particle with Eq.(2.28) and Eq.(2.29).
6. Repeat step 3 to 5 until the global minimum is found or some pre-defined stop criterion is met.

In Figure 2.6, an illustration of implementing PSO for finding the global minimum of Eq.(2.31) is presented, with $nPop = 5$ and the maximum number of iterations set to 16. The upper right corner is the first iteration or the initialization and as can bee seen the particles (blue dots) of the swarm are spread out in the search space, $x = [-10, 10]$, $y = [-10, 10]$. As the algorithm iterates forwards the swarm moves closer to the global minimum of $(x, y) = (1, 3)$, which is seen in the other corners of Figure 2.6.

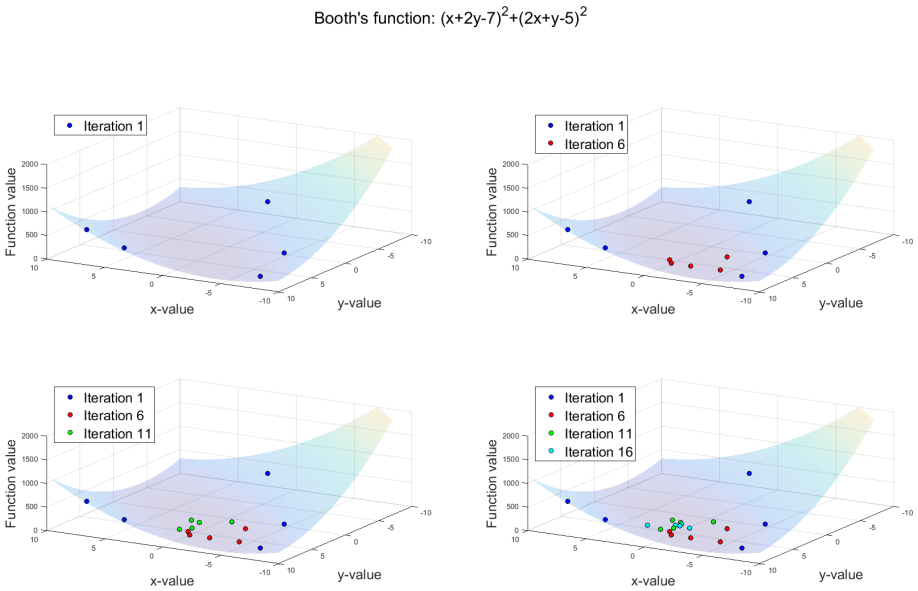

Figure 2.6: Iteration 1, 6, 11 and 16 from implementing PSO to find the global minimum of Booth's function in Eq(2.31).

3| Methods

The approach for modeling the occupant kinematics was to first investigate a suitable way for representing the human as an occupant in a car, and to define what affects the occupant motion during an evasive maneuver. The components of the modeled system were thereafter defined mathematically and implemented in Simulink and MATLAB (ver 2015b, The Mathworks Inc., Natick, MA, USA). The dynamics were computed using the built-in ODE4 solver[1]. In order for the model to replicate occupant kinematics, data from pre-existing volunteer maneuver studies were used for tuning and validating the model.

3.1 Model design

The simplified occupant kinematic model represents an occupant in a car, while the car is performing an evasive maneuver. The model can represent a front seat passenger or a driver. The model includes the torso and the head of the occupant, and the body is restrained by muscle elements, a three-point seat belt, and the seat. The driver model is also restrained by arms that are connected to the steering wheel to model the driver's bracing behavior when resisting longitudinal movement. With the vehicle accelerations and rotations as input, the model can predict the occupant head CoG- and T1 displacement with regards to their initial positions. A description of the model layout is given in Figure 3.1.

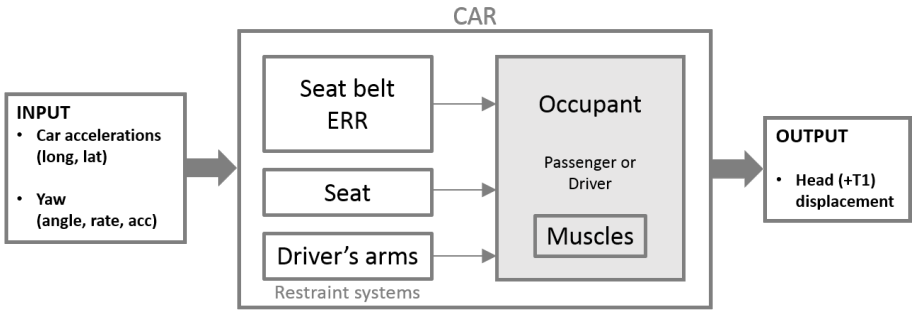

Figure 3.1: Design layout of the simplified occupant kinematic model.

There are several components that affect the occupant motion. These are the accelerating vehicle body, gravity, the seat belt, the seat, the muscle resistance of the occupant's body, and the arms of the occupant when the occupant is a driver. Moreover, since the occupant is located inside the moving car which has an acceleration and rotation, there are also physical phenomena which are induced on the occupant, i.e. fictitious forces.

In total, three different reference systems are required to describe the model. The first is the *occupant reference system*, which is a fixed local system placed in either of the two front seats of the vehicle. The second is the *vehicle reference system* which holds the occupant reference system, and is positioned in front of the car. The two systems accelerate relative a third *inertial reference system*, see section 2.5.5. Figure 3.2 describes the three reference frames in relation to one another. If the hip point coordinates O_{occ} and the coordinates

[1]ODE4 is a fixed step continuous explicit fourth order Runge-Kutta formula solver (MathWorks, 2018).

where the acceleration and rotation data is recorded P_{rec} differ, then recalculations of the data using the equations of *general plane motion*, as derived in Appendix A, is needed.

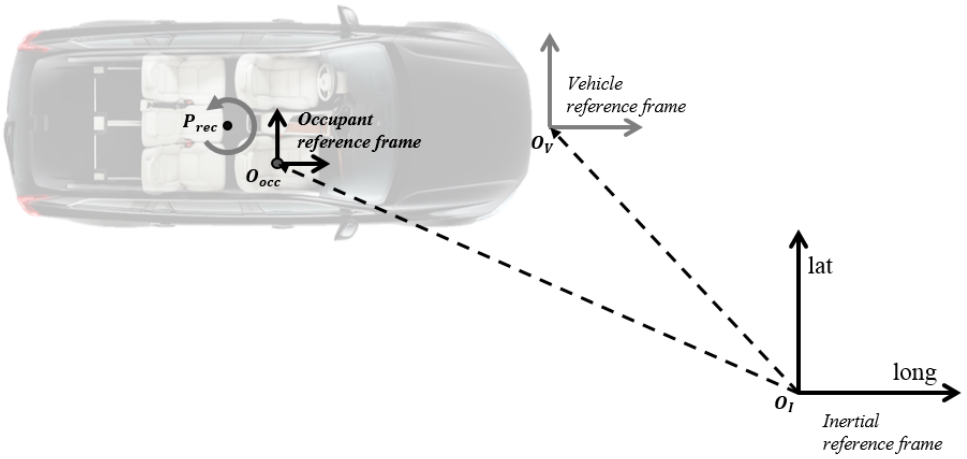

Figure 3.2: Reference systems used to describe the simplified occupant kinematic model, the *occupant-*, the *vehicle-*, and the *inertial* reference frame. Vehicle image courtesy of Volvo Car Corporation.

3.1.1 Occupant models

Since the humans' CoG is located in the upper body, the upright standing human is frequently resembled as an inverted pendulum (Cavagna, Thys, & Zamboni, 1976; McGrath, Howard, & Baker, 2015) in discussions about the human balance during standing and gait. In previous studies, the human has been modeled with one- or multiple rods with one or multiple point masses representing the total mass of the body. Based on this assumption the occupant model, which represents the upper body of a sitting occupant, can be modeled as an inverted pendulum using one or multiple rods. Contrary to gait modeling, which mostly occurs in the longitudinal direction, occupant kinematics also includes the lateral direction. Therefore the spherical inverted pendulum is suitable for modeling the occupant. Two different pendulum designs were developed and evaluated based on their behavior. The design concepts are based on connecting points at different joints and CoG positions of the body, so that pendulum rods, are formed in between. As seen in Figures 3.4a and 3.5a, these points represent the head CoG, T1, sternum, and the hip joint. These are positions that are featured as tracking points in the volunteer data, used later on for tuning and validating the model.

The pendulum consists of one or two massless rigid rods that connect one or two particle masses with a pivot point located at the hip point of the SAFER HBM, see Figure 3.4a and 3.5a. The point masses represent the sternum and head CoG coordinates of the SAFER HBM. The length of the pendulum rods are constant and the motion of the pendulums can be uniquely described with generalized coordinates. The mass and length parameters of the pendulum were chosen to match the SAFER HBM.

The differential equations of the pendulum systems were derived using Lagrangian mechanics, as described in Section 2.5. Originally, all reference systems were arranged (x, y,

z). In order to avoid singularities near the *north-pole* region, i.e. when the pendulum is pointed straight up, a modification of the occupant reference system was necessary. The new orientation yields that the z-axis is the longitudinal direction, positive indicates the direction of travel. The y-axis is the lateral direction, positive indicates left and x-axis is the vertical direction positive indicates downwards. The conversion of the reference system is demonstrated in Figure 3.3.

The pendulum's initial position is angled slightly backwards (104°, relative the longitudinal axis) to resemble the initial sitting position of the occupant when it is leaning against the backrest of the seat. The motion of the pendulum is restrained at the pivot point by two torsional spring-damper pairs. When the pendulum is forced in any direction, the spring-damper pair exerts a torque in the opposite direction of the motion, proportional to the angle and the angular velocity respectively. These components simulate the muscular resistance of the occupant when external forces are acting.

A seat model and a seat belt was added to further restrain the movement of the pendulum. The seat model prevents the pendulum from falling backwards to the south-pole position when only gravity is acting at the start of every simulation. The seat also prevents the pendulum to move too far backwards. The seat belt restricts the pendulum movement forward, i.e. when a sudden brake maneuver causes the pendulum to sling forward. The restraint systems are further described in section 3.1.2. The differential equations, referred to as the Equations of motion, for each design approach are given in section 3.2.

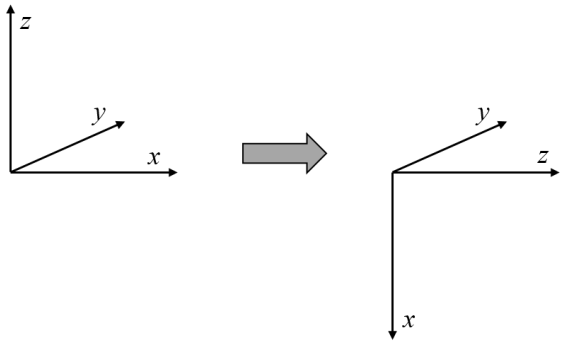

Figure 3.3: Conversion of the occupant pendulum reference system.

Inverted spherical pendulum

As a first design, the occupant was represented as a single inverted spherical pendulum as seen in Figure 3.4. A massless rigid rod represents the distance between the hip point to the sternum, where the mass, m, is positioned. The motion of the pendulum can, by using spherical coordinates, be described as a system with two DoF. The rod length is denoted r, which remains constant, and the generalized coordinates are the north-pole angle θ and its' azimuth φ.

As seen in Figure 3.4a, an imaginary line is drawn between the pivot point and the head CoG with the length r_{hCoG}. In order to apply the concept of a point mass the sternum point is relocated to this line, i.e. the length of the rod r is equal to r_s. The upper body mass of the SAFER HBM, 46 kg, was used as the mass parameter. As output, the single pendulum can compute the head CoG displacement.

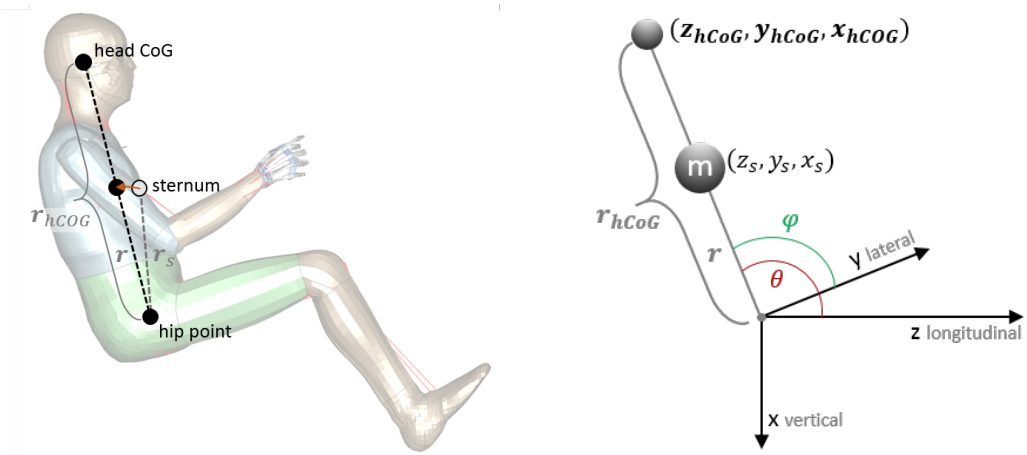

(a) Design concept of the single pendulum based on the SAFER HBM.

(b) Representation of the single pendulum in the occupant reference frame.

Figure 3.4: Design of the single pendulum model.

The position of the single pendulum can be described using spherical coordinates θ, φ and r and a conversion to the Cartesian system is needed to describe the kinematics. The positions of sternum and the head CoG are described using Eq. (3.1) and Eq. (3.2).

$$\begin{aligned} x_s &= -r\sin\theta\sin\phi \\ y_s &= r\sin\theta\cos\phi \\ z_s &= r\cos\theta \end{aligned} \tag{3.1}$$

$$\begin{aligned} x_{hCoG} &= -r_{hCoG}\sin\theta\sin\phi \\ y_{hCoG} &= r_{hCoG}\sin\theta\cos\phi \\ z_{hCoG} &= r_{hCoG}\cos\theta \end{aligned} \tag{3.2}$$

Inverted spherical double pendulum

The second design is an inverted spherical double pendulum, i.e. it has two joints, see Figure 3.5. The second joint is placed on the rod to represent a "neck joint" located at T1, defined as a hinge joint which allows movement in the plane which the pendulum spans with the longitudinal coordinate axis. This joint is restrained by one torsion spring-damper pair. The double pendulum approach allows the head and sternum to move relative each other in the longitudinal direction. A system with three DoF is yielded with two rigid rods, and the generalized coordinates θ_1, φ, and θ_2. The motion of the lower pendulum can be described by θ_1, and φ. The motion of the upper pendulum can be described by θ_2, the angle of the upper rod relative a horizontal plane in the position of the T1 joint.

For the double pendulum, the mass of the upper body is divided into two point masses, the first to represent the sternum and the second to represent the head. The sum of these masses add up to 46 kg where the head mass is 6 kg, and the sternum mass is 40 kg, as obtained from the SAFER HBM. As seen in Figure 3.5a, an imaginary line is drawn between the pivot point and T1, denoted r_{T1}. In order to apply the concept of point masses, the sternum point is relocated to this line. Hence the length of the rod r is equal

to the length between the pivot point and sternum, r_s. The length of the rod extending from T1 to the head CoG, is denoted r_{hCoG}. The double pendulum can compute the head CoG- and T1 displacements.

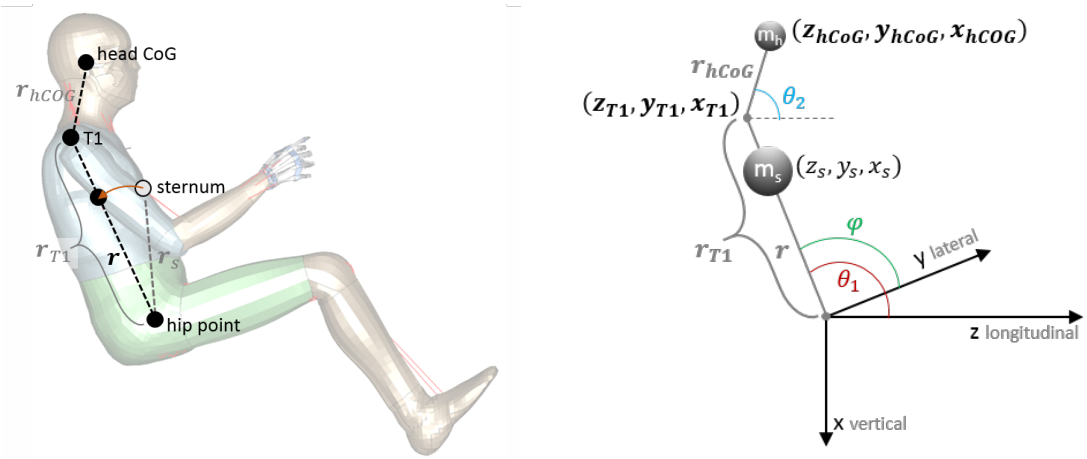

(a) Design concept of the double pendulum based on the SAFER HBM.

(b) Representation of the double pendulum in the occupant reference frame.

Figure 3.5: Design of the double pendulum model.

The position of sternum, T1 and the head CoG can be described using Eq. (3.3), Eq. (3.4), and Eq. (3.5).

$$\begin{aligned} x_s &= -r \sin\theta_1 \sin\phi \\ y_s &= r \sin\theta_1 \cos\phi \\ z_s &= r \cos\theta_1. \end{aligned} \tag{3.3}$$

$$\begin{aligned} x_{T_1} &= -r_{T_1} \sin\theta_1 \sin\phi \\ y_{T_1} &= r_{T_1} \sin\theta_1 \cos\phi \\ z_{T_1} &= r_{T_1} \cos\theta_1. \end{aligned} \tag{3.4}$$

$$\begin{aligned} x_{hCoG} &= x_{T_1} - r_{hCoG} \sin\theta_2 \sin\phi \\ y_{hCoG} &= y_{T_1} + r_{hCoG} \sin\theta_2 \cos\phi \\ z_{hCoG} &= z_{T_1} + r_{hCoG} \cos\theta_2. \end{aligned} \tag{3.5}$$

3.1.2 Restraint models

The restraint models maintain the initial position of the pendulum at the start of the simulation. When there is a maneuver, the restraint models simulate the functions of the physical restraint systems. Each restraint model exerts a force on the pendulum which is included in the system's Equations of motion as a generalized force, see section 2.5.3. A visualization of the occupant pendulum and the restraint systems is demonstrated in Figure 3.6.

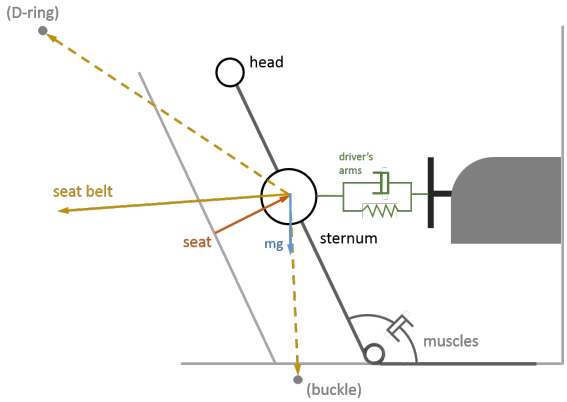

Figure 3.6: Representation of the occupant model and the restraint systems.

Seat model

The seat model restricts the pendulum from moving backwards from its initial position. The seat is set to the angle of the pendulum initial position in order for the pendulum not to fall down to the south-pole position at the start of each simulation. The seat model also restricts the pendulum from moving too far back in the case of a high acceleration forward, or in the rebound after a maneuver. The seat is modeled using three planes to simulate the flat backrest of the seat and the side barriers which restrict the occupant's lateral movement, see Figure 3.7. When the pendulum intrudes the seat, a force is applied on the point mass representing sternum. The force magnitude is proportional to the seat intrusion and acts in the normal of the plane which the pendulum has intruded. The force with respect to intrusion was approximated using a simulation in LS Dyna (R9.2 double precision, Livermore Software Technology Corporation) of an impactor with mass 46 kg hitting the backrest of a Volvo V60 seat with an impact speed of 1 m/s. As a simplification, there is no friction applied if the pendulum moves laterally against the seat.

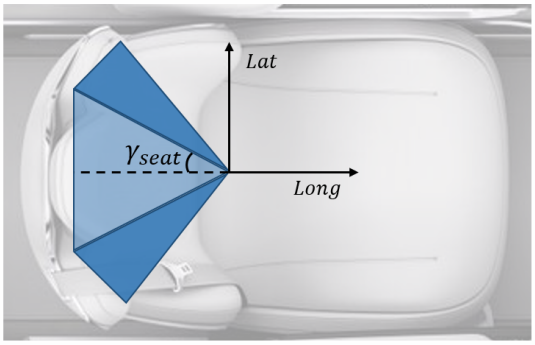

Figure 3.7: Schematics of the seat model, consisting of three planes.

Seat belt model

The seat belt was modeled to resemble the actual seat belt locking mechanism, as described in section 2.3, but assuming no sliding between the belt and the chest, i.e. no displacement of the application point of the seat belt force along the pendulum rod. The retractor locks the seat belt pay-out at a certain level of deceleration or lateral acceleration, as well as at a certain rate of the seat belt pay-out. As stated in section 2.3, the

acceleration limit used for the model is $a_{lim} = 0.45\ g$. The threshold for the seat belt pay-out rate was set to $u_{lim} = 80$ mm/s.

When the seat belt pay-out is locked, a force is applied to the pendulum point mass representing sternum. The force direction is the resultant of two vectors, where the first vector is the vector between the pendulum sternum point mass and the seat belt D-ring position which is located on the B-pillar, i.e. the second vertical supporting pillar of the occupant cabin, near the roof. The second vector is the vector between the pendulum point mass and the seat belt buckle position. The magnitude of the seat belt force depends on the elongation dependent stiffness, as described in section 2.3.

ERR

The seat belt electrical pre-tensioning system, ERR, is modeled as an additional seat belt force contribution which is triggered shortly before the maneuver. The force and activation time can be varied, but when triggered the force is applied during the whole maneuver. As seen in Figure 3.8, the function is implemented in the model as a step function with an ramp-up to the force peak value. The slope at the ramp-up can also be varied.

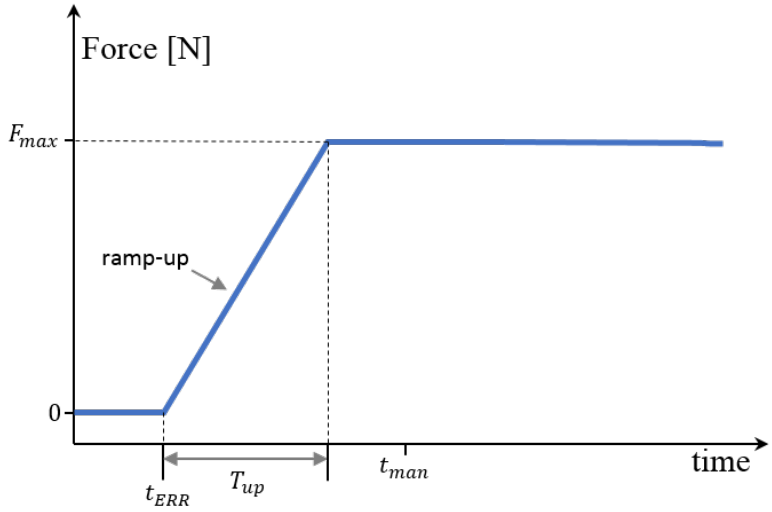

Figure 3.8: The ERR model force pulse. T denotes duration and t denotes an activation time instant.

Driver's arms

Since a driver holds the steering wheel during normal driving conditions, the kinematics in an evasive maneuver will be affected, see section 2.2. The arms are modeled with a spring-damper pair which spans between the pendulum sternum point mass, and the steering wheel. The spring-damper pair applies a force on the pendulum when the distance between the steering wheel and the pendulum deviates from the initial length. The applied force is proportional to the deviation and rate of change of this distance. The force direction is either towards the pendulum or towards the steering wheel depending on whether the distance is increasing or decreasing.

3.2 Model equations of motion

The equations of motion for the two pendulum models were derived using Lagrangian mechanics techniques, as described in section 2.5.2. The total force acting on each pendulum is the addition of the pendulum mass times the gravitational acceleration, the torques exerted in the joints by the spring-damper pairs, the forces induced by the restraint systems, as well as the fictitious forces due to the accelerating reference frame.

Inverted spherical pendulum
The equations to describe the motion of the inverted spherical pendulum are presented in the equation system of Eq. (3.6).

$$\underbrace{\begin{bmatrix} mr^2 & 0 \\ 0 & mr^2\sin^2\theta \end{bmatrix}}_{\boldsymbol{M(q)}} \underbrace{\begin{bmatrix} \ddot{\theta} \\ \ddot{\varphi} \end{bmatrix}}_{\{\ddot{q}_i i\}} = \underbrace{\begin{bmatrix} 0 & mr^2\dot{\varphi}\cos\theta sin\theta \\ -mr^2\dot{\varphi}\cos\theta\sin\theta & -mr^2\dot{\theta}\cos\theta\sin\theta \end{bmatrix}}_{\boldsymbol{S(q,\dot{q})}} \underbrace{\begin{bmatrix} \dot{\theta} \\ \dot{\varphi} \end{bmatrix}}_{\{\dot{q}_i\}} + \underbrace{\begin{bmatrix} mrg\cos\theta\sin\varphi \\ mrg\cos\varphi\sin\theta \end{bmatrix}}_{\boldsymbol{G(q)}} - \underbrace{\begin{bmatrix} k_\theta\theta \\ k_\varphi\varphi \end{bmatrix}}_{\boldsymbol{K(q)}} - \underbrace{\begin{bmatrix} c_\theta\dot{\theta} \\ c_\varphi\dot{\varphi} \end{bmatrix}}_{\boldsymbol{C(\dot{q})}} + \underbrace{\begin{bmatrix} \boldsymbol{F}_{total} r\hat{\boldsymbol{e}}_\theta \\ \boldsymbol{F}_{total} r\hat{\boldsymbol{e}}_\varphi \end{bmatrix}}_{\boldsymbol{N(q)}} + \underbrace{\begin{bmatrix} \boldsymbol{F}_r r\hat{\boldsymbol{e}}_\theta \\ \boldsymbol{F}_r r\hat{\boldsymbol{e}}_\varphi \end{bmatrix}}_{\boldsymbol{R(q)}} \tag{3.6}$$

Where $\boldsymbol{F}_{total} = \boldsymbol{F}_{system} + \boldsymbol{F}_{euler} + \boldsymbol{F}_{coriolis} + \boldsymbol{F}_{centripetal}$, i.e. the resultant of the system force and fictitious force vectors. $\boldsymbol{F}_r$ is the restraint system force resultant vector, and $\boldsymbol{F}_r = \boldsymbol{F}_{sb} + \boldsymbol{F}_s + \boldsymbol{F}_a$ (seat belt force, seat force, and driver's arms force respectively). These vectors are expressed as Cartesian vectors which are projected onto the spherical unit vectors $\hat{\boldsymbol{e}}_\theta$ and $\hat{\boldsymbol{e}}_\varphi$.

$\boldsymbol{M(q)}$ is the system mass matrix, $\boldsymbol{S(q,\dot{q})}$ is the coupling matrix, $\boldsymbol{G(q)}$, $\boldsymbol{K(q)}$, and $\boldsymbol{C(\dot{q})}$ are the gravity and spring-damper contributions. $\boldsymbol{N(q)}$ and $\boldsymbol{R(q)}$ are the system plus fictitious forces and restrains forces, respectively. By multiplying the inverse of the mass matrix, $\boldsymbol{M}^{-1}$, to both sides of Eq.(3.6), the system of differential equations in Eq.(3.7) was obtained.

$$\{\ddot{q}_i\} = \boldsymbol{M(q)}^{-1}(\boldsymbol{S(q,\dot{q})}\{\dot{q}_i\} + \boldsymbol{G(q)} - \boldsymbol{K(q)} - \boldsymbol{C(\dot{q})} + \boldsymbol{N(q)} + \boldsymbol{R(q)}). \tag{3.7}$$

For the full derivation of these equations, see Appendix C.

Inverted spherical double pendulum
The system of equations that describes the motion of the inverted spherical double pendulum can be represented using Eq.(3.8).

$$\boldsymbol{M(q)}\{\ddot{q}_i\} = \boldsymbol{S(q,\dot{q})}\{\dot{q}_i\} + \boldsymbol{G(q)} - \boldsymbol{K(q)} - \boldsymbol{C(\dot{q})} + \boldsymbol{N(q)} + \boldsymbol{R(q)} \tag{3.8}$$

where $\boldsymbol{M(q)}$ is the system mass matrix, $\boldsymbol{S(q,\dot{q})}$ is the coupling matrix, $\boldsymbol{G(q)}$, $\boldsymbol{K(q)}$ and $\boldsymbol{C(\dot{q})}$ are the gravity and spring-damper contributions. $\boldsymbol{N(q)}$ and $\boldsymbol{R(q)}$ are the system-plus fictitious forces and restraint forces, respectively. By multiplying the inverse of the mass matrix, $\boldsymbol{M}^{-1}$, to both sides of Eq.(3.8) the system of differential equations in Eq.(3.9) was obtained.

$$\{\ddot{q}_i\} = \boldsymbol{M(q)}^{-1}(\boldsymbol{S(q,\dot{q})}\{\dot{q}_i\} + \boldsymbol{G(q)} - \boldsymbol{K(q)} - \boldsymbol{C(\dot{q})} + \boldsymbol{N(q)} + \boldsymbol{R(q)}). \tag{3.9}$$

The entries in each matrix and the full derivation of the equations of motion are presented in Appendix D.

3.3 Volunteer maneuver tests

Reference data from volunteer tests was required for tuning and validation of the model. For this purpose, three data sources were selected out of pre-existing experimental studies of volunteer maneuver tests. All tests were performed in real cars on test tracks, where the volunteers were placed either in the front passenger's seat or the driver's seat. The tests included braking-, lane-change, and lane-change plus braking (combined) maneuvers. As stated in section 2.2, there are differences between passenger and driver kinematics in evasive maneuvers. Therefore the passenger- and the driver model require different tuning datasets which represent passenger- and driver kinematics respectively. Below are specifications of each volunteer study, and lastly a summary of the test datasets that were used for either tuning or validation of the model are presented in Table 3.1.

3.3.1 SAFER Longitudinal maneuver tests

The *SAFER Longitudinal*[2] volunteer study was published by J. Östh *et al.* 2013, and J. Olafsdottir *et al.* 2013, and performed by Chalmers University of Technology, Autoliv Research AB, Umeå University, Volvo Group and Volvo Cars at SAFER Vehicle and Traffic Safety Centre at Chalmers. The study is divided into two papers where the first includes only occupants in the driver position (Östh et al., 2013), and the second includes occupants in the front seat passenger position (Ólafsdóttir et al., 2013). Volunteers were seated in a Volvo V60 model year 2012 that was subjected to harsh braking maneuvers (deceleration of approximately 1.1 g). The volunteers consisted of eleven males and nine females. The seat belt configurations were standard belt and ERR belt. The ERR force was 170 N initiated 200 ms before the maneuver. The backrest of the seat was fixed to 112° relative the horizontal plane. The data acquired included displacement and rotation of several points on the volunteers (among these the head CoG and the T1 vertebrae), car longitudinal acceleration, interior forces (among these the arm's bracing force against the steering wheel, and seat belt force), and occupant muscular response.

3.3.2 SAFER Lateral maneuver tests

The *SAFER Lateral* volunteer study was published and submitted to the Ircobi Conference 2018 by G. Ghaffari 2018, and carried out by Chalmers, Autoliv Research AB, and Volvo Cars at SAFER Vehicle and Traffic Safety Centre at Chalmers. The tests in the study include lane-change and combined maneuvers, corresponding to a longitudinal deceleration and lateral acceleration of approximately 0.5 g. 9 male volunteers were positioned as passengers, and the tests were performed in a Volvo V60 model year 2016. Two seat belt configurations were used, a standard belt and ERR belt set to a force of 170 N that was initiated 200 ms prior to the maneuver. The backrest of the seat was fixed to 115° relative the horizontal plane. The collected data included displacement and rotation of points on the occupant body (among them the head CoG and the T1 vertebrae), car longitudinal and lateral acceleration as well as rotation, interior forces (including the seat belt force), and occupant muscular response.

[2]Names in italic are given as denotation of volunteer data sources in the following sections.

3.3.3 Graz maneuver tests

The *Graz* volunteer study was published by P. Huber *et al.* 2015, and carried out by Graz University of Technology at the Virtual Vehicle Research Centre in Graz, Austria. The tests were performed with a Mercedes-Benz S-500 in which the volunteers were placed in the front passenger seat and subjected to braking-, lane-change-, and combined maneuvers, for which accelerations were around 1 g. Among the volunteers were 19 males and 6 females. As opposed to the tests stated above, the maneuvers were performed by a driver instead of a robot. The tests were performed using a modified seat for which the backrest angle was fixed to 104° relative the horizontal plane. The data collected included car longitudinal and lateral acceleration and rotation, occupant head and sternum displacement and rotation, and steering wheel angle.

Complete kinematic data for all three maneuver types, i.e. braking, lane-change and combined maneuver, exists only for the passenger position. Therefore out of the passenger model and the driver model, only the passenger model was selected for tuning and validation.

Table 3.1: Summary of the datasets used for tuning and validation of the simplified occupant kinematic model, collected from volunteer maneuver tests (Östh et al., 2013; Ólafsdóttir et al., 2013; Ghaffari et al., 2018; Huber et al., 2015). Combined maneuver denotes lane-change plus braking, SB is standard belt. Note that all datasets from the presented volunteer studies are not included.

Data source	Volunteers	Maneuver	Occupant position	Belt type	Application (Tuning/ Validation)	No.
SAFER Longitudinal	11 males 9 females	Braking	Passenger	SB	Validation	1
SAFER Lateral	9 males	Combined	Passenger	SB	Tuning	2
		Lane-change	Passenger	SB	Validation	3
		Combined	Passenger	ERR	Validation	4
Graz	19 males 6 females	Combined	Passenger	SB	Validation	5

3.4 Model tuning and validation

The PSO algorithm, described in section 2.6.1, was used to tune the model response to fit the volunteer kinematic response. The parameters of interest were the spring stiffness and the damper coefficients of the spring-damper pairs, i.e. $k_\theta, k_\varphi, c_\theta, c_\varphi$ for the single pendulum and $k_{\theta_1}, k_\varphi, k_{\theta_2}, c_{\theta_1}, c_\varphi, c_{\theta_2}$ for the double pendulum, as well as the width of the backrest of the seat, γ_{seat} (see Figure 3.7). A physical interpretation of the tuning of the spring-damper pairs is to characterize the occupant tensing its muscles as a reaction to the maneuver. The shoulder width of each volunteer in the tuning dataset is unknown, and since the width of the occupant limits lateral movement against the seat, the distance before the shoulder engages the lateral side barrier of the seat is unknown. The width of the backrest was therefore optimized to provide a suitable seat geometry.

For the parameter tuning, dataset *No.*(2) from the *SAFER lateral study* was selected, see Table 3.1 in section 3.3. Since the vehicle motion of a combined maneuver induces both

longitudinal-, lateral-, and rotational motion on the occupant pendulum, this allowed for tuning of all parameters for all states simultaneously. Furthermore, as the dataset contains test data from 24 volunteers, the tuning of the models generated 24 datasets for each model design. Figure 3.9 presents the mean longitudinal and lateral accelerations, yaw angle rate of change, i.e. the angular velocity of the vehicle, as well as the mean seat belt force from the 24 volunteer tests.

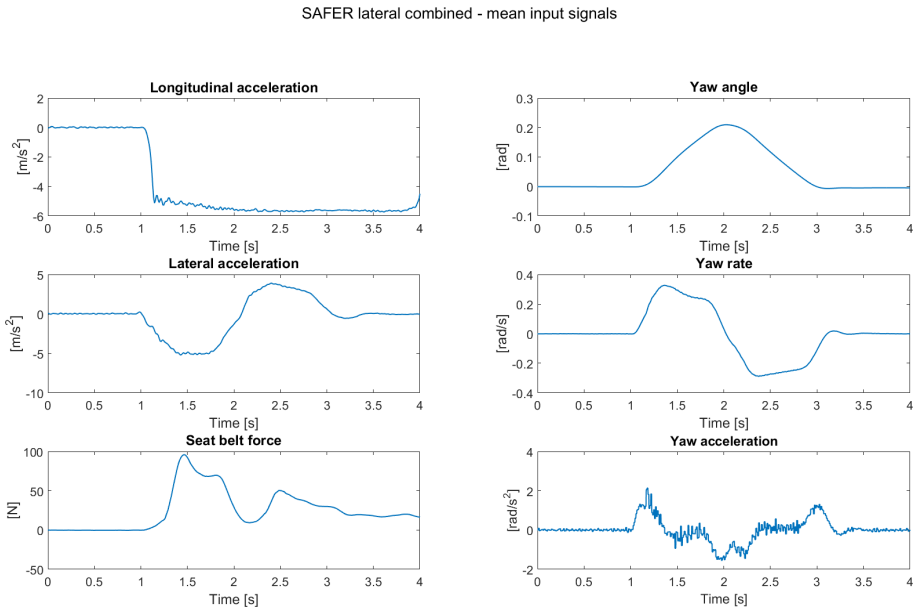

Figure 3.9: Mean signals obtained from the combined maneuver tests of the *SAFER Lateral* study, dataset *No.(2)*.

3.4.1 Particle swarm optimization

The objective function, for which the purpose is to minimize the difference between the model output and the reference data, is based on the RMSE function, defined in section 2.6. Since the reference data contains several important states that the model aims to capture, i.e. the longitudinal and lateral displacement and the seat belt force, a weighted sum of RMSE terms were used as the objective function. In order for the model response to obtain similar energy content as the reference data (Keysight Technologies, 2016), frequency spectrum analysis of the model output and reference data were compared and included in the weighted sum of RMSE. The frequency spectrum of the signal was computed using the Fast Fourier Transform.

The search space is defined by specifying the minimum and maximum value of each of the parameters that are of interest. For the optimization of the models, 40 iterations were run with 50 particles each. The amount of iterations and particles were chosen through testing different setups where iterations and particles were varied, for which it was shown that a larger number of particles and iterations gave a more accurate result compared to for example 10 iterations and 20 particles.

3.4.2 PSO setup

Tables 3.2 and 3.3 denote the search space boundaries for the two pendulum designs. Tables 3.4 and 3.5 denote the weights given for the objective functions, and Eq.(3.10) and Eq.(3.11) are the objective functions for the optimization of the two model designs. The search space boundaries were set in order to reduce the risk of the algorithm getting trapped in local optimum. Concurrently, a tight search space was undesired since the solutions would then be more likely to end up in the boundary values indicating that optimal values were not found. The weights of the objective function were selected to yield the best fit of the model response.

Table 3.2: Search space boundary values for the Inverted spherical single pendulum.

Tuning parameter	Min value	Max value	Unit
k_θ (Spring coeff.) k_θ	50	1500	[Nm/rad]
k_φ (Spring coeff.)	50	1500	[Nm/rad]
c_θ (Damper coeff.)	10	400	[Nm·s/rad]
c_φ (Damper coeff.)	10	400	[Nm·s/rad]
γ_{seat} (Seat width)	0.1	10	[°]

Table 3.3: Search space boundary values for the Inverted spherical double pendulum.

Tuning parameter	Min value	Max value	Unit
k_{θ_1} (Spring coeff.)	50	1500	[Nm/rad]
k_φ (Spring coeff.)	50	1500	[Nm/rad]
c_{θ_1} (Damper coeff.)	10	400	[Nm·s/rad]
c_φ (Damper coeff.)	10	400	[Nm·s/rad]
k_{θ_2} (Spring coeff.)	10	400	[Nm/rad]
c_{θ_2} (Damper coeff.)	10	400	[Nm·s/rad]
γ_{seat} (Seat width)	0.1	10	[°]

Table 3.4: Weights used in the objective function for the inverted spherical single pendulum.

Weight	Value
w_1	0.27
w_2	0.18
w_3	0.23
w_4	0.17
w_5	0.05
w_6	0.10

Table 3.5: Weights used in the objective function for the inverted spherical double pendulum.

Weight	Value
w_1	0.12
w_2	0.12
w_3	0.12
w_4	0.12
w_5	0.08
w_6	0.08
w_7	0.08
w_8	0.08
w_9	0.08
w_{10}	0.12

where $w_1, w_2, ..., w_6$ in Table (3.4) denote the weights of the head longitudinal displacement, head lateral displacement, seat belt force, and the frequency spectrum of the three states respectively, for the inverted single pendulum. The weights $w_1, w_2, ..., w_{10}$ in Table (3.5) correspond to the head longitudinal displacement, head lateral displacement,

T1 longitudinal displacement, T1 lateral displacement, seat belt force, and the frequency spectrum of the five states respectively, for the inverted double pendulum. The objective functions are defined in Eqs. (3.10) and (3.11), for the single and double pendulums respectively.

$$minf_{obj,single} = min \sum_{i=1}^{6} w_i RMSE_i \tag{3.10}$$

$RMSE_i = RMSE_1, RMSE_2, ..., RMSE_6$ are the computed errors for the states, i.e. longitudinal head displacement, lateral head displacement, seat belt force, and the frequency spectrum of the three states respectively.

$$minf_{obj,double} = min \sum_{i=1}^{10} w_i RMSE_i \tag{3.11}$$

$RMSE_1, RMSE_2, ..., RMSE_{10}$ are the computed errors for the states, i.e. longitudinal head displacement, lateral head displacement, T1 longitudinal displacement, T1 lateral displacement, seat belt force, and the frequency spectrum of the five states respectively. The RMSE for each state is computed as described in section 2.6.

3.4.3 Selection of parameter sets

After running the PSO algorithm for the two model designs, 24 parameter sets were obtained for each model. The parameter sets contain values for the parameters of interest, each representing the dynamic characteristics of one of the 24 volunteer tests in the dataset. The two models were then simulated using all parameter sets, with the mean acceleration and yaw from the maneuvers of the volunteer tests as input. The head displacement of the model was then compared to the corridor, i.e. the mean and the first standard deviation, of the volunteers' head displacement as presented in Figures 3.10 and 3.11. Out of these 24 parameter sets, a family of 7 parameter sets for each model were selected based on the criteria below.

1. the family must represent the whole spectrum of included individuals, which corresponds to a varying muscle stiffness between individuals,
2. each selected parameter set must capture the dynamic behavior of the underlying system.

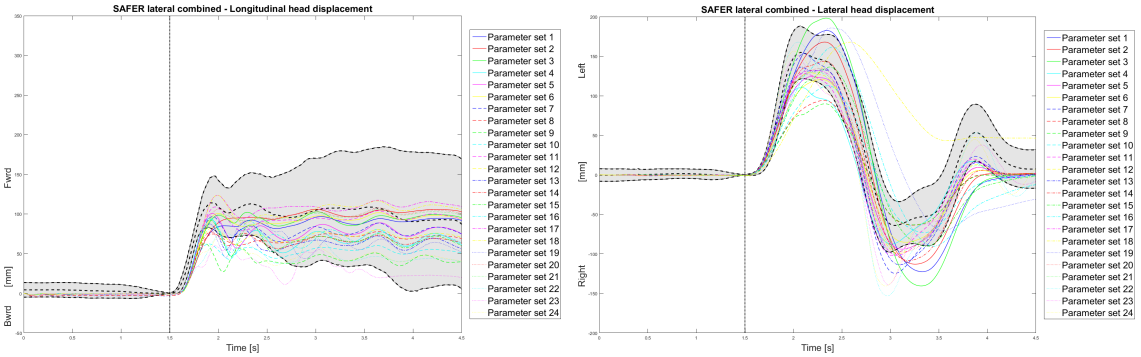

(a) Longitudinal head displacement. **(b)** Lateral head displacement.

Figure 3.10: The single pendulum model response of the 24 obtained parameter sets, with the mean acceleration and rotation of the tuning dataset ($No.(2)$) as input, and the corresponding head displacement corridors as reference (gray area). The vertical line corresponds to the maneuver onset time.

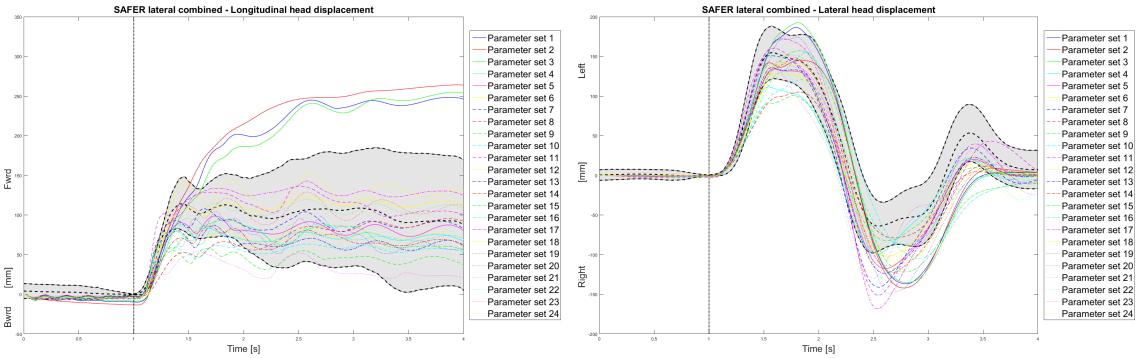

(a) Longitudinal head displacement. **(b)** Lateral head displacement.

Figure 3.11: The double pendulum model response of the 24 obtained parameter sets, with the mean acceleration and rotation of the tuning dataset ($No.(2)$) as input, and the corresponding head displacement corridors as reference (gray area). The vertical line corresponds to the maneuver onset time.

3.4.4 Model validation

To validate the response of the model, the model displacements of the parameter sets were compared to the displacement corridors[3] of the volunteer kineamatic data. The validation was performed with respect to three volunteer datasets, including the maneuvers braking, lane-change, and combined maneuvers. The input used was the mean car accelerations and yaw from each corresponding volunteer test. To avoid double-counting of the tuning data, different datasets were used for validation of the model than for the tuning. The selected validation datasets were $No.(1, 3, 5)$ as denoted in Table 3.1. The criteria for the validation were the following,

1. the model response has similar dynamic behavior to the volunteer data,
2. the model response represents the variations in displacements as seen among the volunteers of the dataset, within the time for the maneuver.

[3]For the Graz data the median and 0.16^{th} and 0.84^{th} quantiles were used.

All criteria were evaluated based on visual interpretation of the results.

ERR validation

To validate the ERR function of the seat belt model, simulations of the double pendulum model were run with the mean input from dataset *No.*(4), a combined maneuver. This dataset which includes both longitudinal and lateral acceleration, and rotation, was selected to study the reduction of the displacement both longitudinally and laterally. To study the effect of the ERR function, the T1 displacement of the model with the ERR belt configuration was compared to the corresponding displacement with the standard belt configuration. The resulting displacement alterations between the two belt configurations were then compared to the results found in the volunteer tests, as stated in section 2.3.1.

For the simulation, the configuration setup used in the volunteer tests, as stated in section 3.3 was used. Hence, the pulse was triggered 200 ms before the maneuver, with a peak force of 170 N. The duration of the function as well as the slopes of the ramp-up, were varied to obtain similar responses as for the volunteers.

4| Results

The following sections present the results of the model tuning and validation.

4.1 Inverted spherical pendulum

Table 4.1 presents the members of the selected family of parameter sets for the single pendulum model, given new set names. The letter S denotes the single pendulum. The computation time of the model is 0.7 seconds[1].

Table 4.1: The 7 parameter sets selected for the single pendulum model.

No.	Name
1	SA
2	SB
8	SC
11	SD
17	SE
18	SF
23	SG

Figures 4.1, 4.2, and 4.3 present the single pendulum model head displacement response for each parameter set in the selected family, with respect to the corridors of the validation datasets. The model input was the mean car accelerations and rotations for each corresponding validation dataset.

As seen in Figure 4.1, the overall dynamic response is captured by the model for both longitudinal and lateral displacement when it is subjected to the lane-change maneuver from dataset *No.*(3). For the lateral displacement, the model underestimates the leftward head displacement for all the parameter sets, but overestimates rightward head displacement in the rebound. The lateral head response of parameter set *SC* and *SF*, are slightly delayed compared to the validation data.

Similarly to previous plots, as seen in Figure 4.2, the model kinematic response and dynamics correspond well with the response of the emergency braking maneuver of dataset *No.*(1). During the maneuver, the seatbelt of the model locks to restrict further forward motion of the pendulum head. However, the longitudinal displacement is underestimated for all parameter sets. In this reference dataset, the lateral displacement was not recorded due to little lateral motion and is therefore not included.

As seen in Figure 4.3, the model validation with respect to dataset *No.*(5) shows that the model's longitudinal displacement corresponds well with the volunteer data for the combined pre-crash maneuver. However, the lateral head displacement is overestimated. Once again, the model captures the dynamic response of the validation data. Again, parameter set *SC* and *SF* are slightly delayed compared to the validation data.

[1]Intel i7 2.7GHz, 16GB RAM

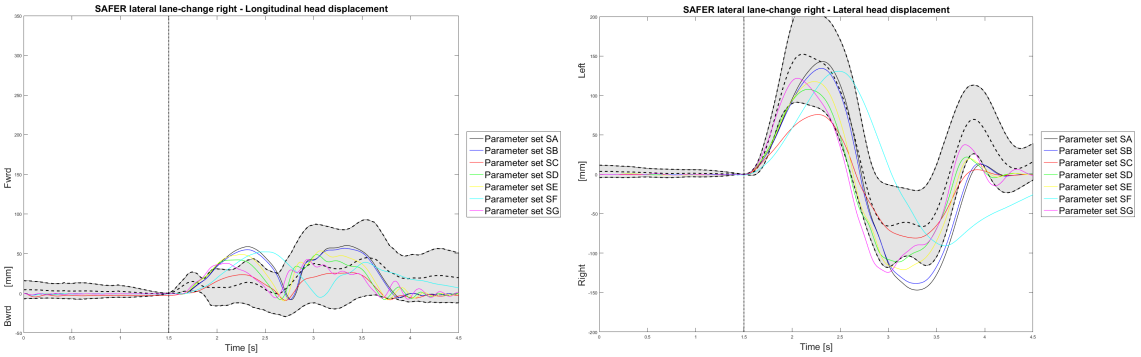

(a) Longitudinal head displacement. **(b)** Lateral head displacement.

Figure 4.1: Head displacement of the single pendulum compared to the corridor (gray area) of the head displacement in volunteer dataset *No.*(3) *SAFER lateral*, a lane-change maneuver. The vertical line corresponds to the maneuver onset time.

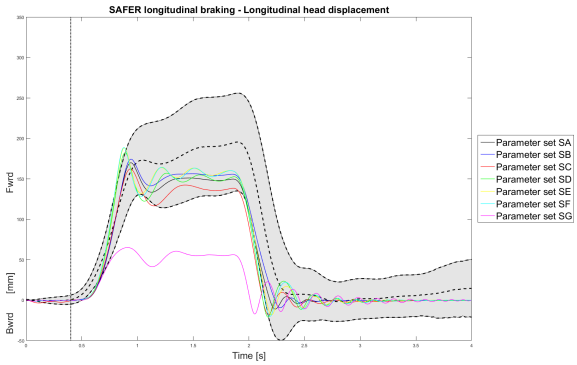

Figure 4.2: Head displacement of the single pendulum compared to the corridor (gray area) of the head displacement in volunteer dataset *No.*(1) *SAFER longitudinal*, an emergency braking maneuver. The vertical line corresponds to the maneuver onset time.

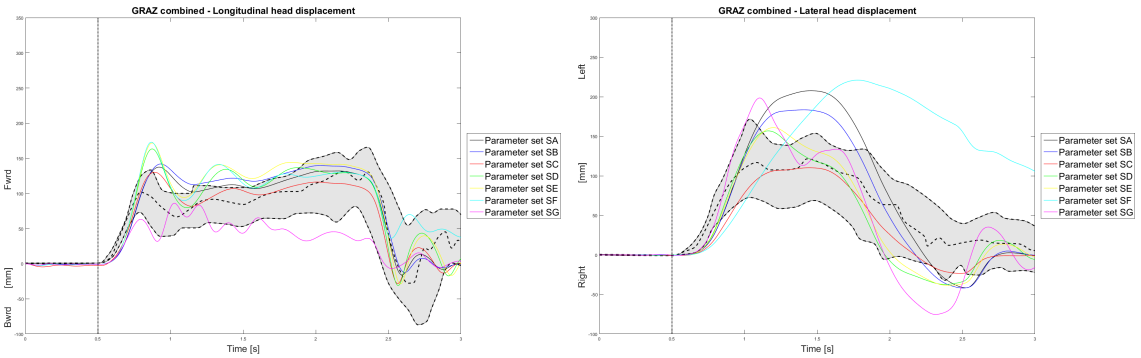

(a) Longitudinal head displacement. **(b)** Lateral head displacement.

Figure 4.3: Head displacement of the single pendulum compared to the corridor (gray area) of the head displacement in volunteer dataset *No.*(5) *Graz study*, a combined maneuver. The vertical line corresponds to the maneuver onset time.

4.2 Inverted spherical double pendulum

In Table 4.2 the members of the selected family of parameter sets for the double pendulum model are displayed, given new names. The letter D denotes the double pendulum. The computation time of the model is 0.7 seconds[2].

Table 4.2: The 7 parameter sets selected for the double pendulum model.

No.	Name
1	DA
5	DB
6	DC
7	DD
9	DE
11	DF
17	DG

Below, the double pendulum model responses for the head CoG and T1 displacement are presented with respect to the corridors of the validation datasets. The model input were the mean car accelerations and rotations for each corresponding validation dataset.

Head displacement

Regarding the response for the lane-change maneuver in dataset *No.*(3), as seen in Figure 4.4, the overall dynamic response is captured by the double pendulum model for both the longitudinal and lateral head displacements. For lateral head displacement the model slightly underestimates the leftward head displacement for all parameter sets, but overestimates rightward head displacement in the rebound.

Observing the model response of the pure braking maneuver as seen in Figure 4.5, the model captures the overall dynamics of dataset *No.*(1) and demonstrates a variation in responses for the longitudinal head displacement. A similar reduction of forward motion of the model's head, due to the locking of the seat belt, can be observed during the maneuver when comparing the response to the data. The timing of the model response corresponds to the validation data except for parameter set *DA* which shows a lagging behavior in the rebound phase of the movement.

As seen in Figure 4.6, the model response captures the kinematics of dataset *No.*(5), which implicates a combined maneuver. However, most of the parameter sets overestimate both the longitudinal and lateral head displacement. Again, parameter set *DA* shows a lagging behavior for the longitudinal displacement.

[2]Intel i7 2.7GHz, 16GB RAM

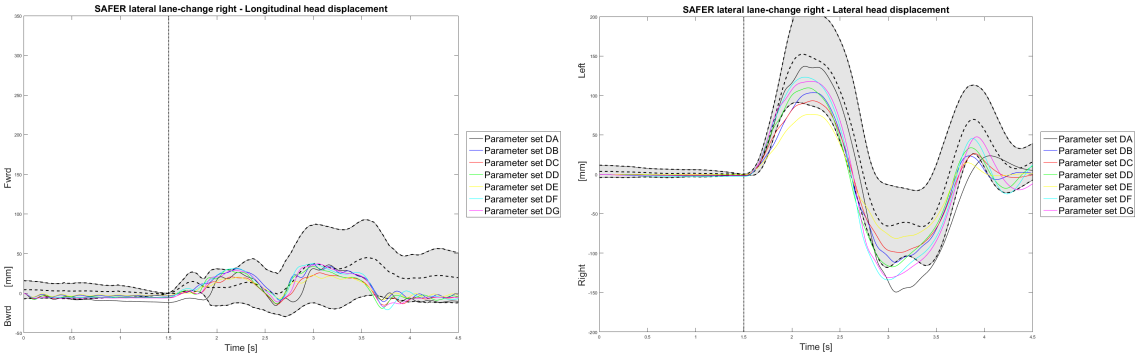

(a) Longitudinal head displacement. **(b)** Lateral head displacement.

Figure 4.4: Head displacement of the double pendulum compared to the corridor (gray area) of the head displacement in volunteer dataset *No.*(3) *SAFER lateral*, a lane-change maneuver. The vertical line corresponds to the maneuver onset time.

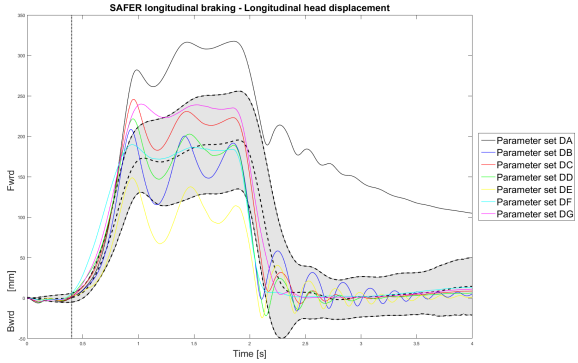

Figure 4.5: Head displacement of the double pendulum compared to the corridor (gray area) of the head displacement in volunteer dataset *No.*(1) *SAFER longitudinal*, an emergency braking maneuver. The vertical line corresponds to the maneuver onset time.

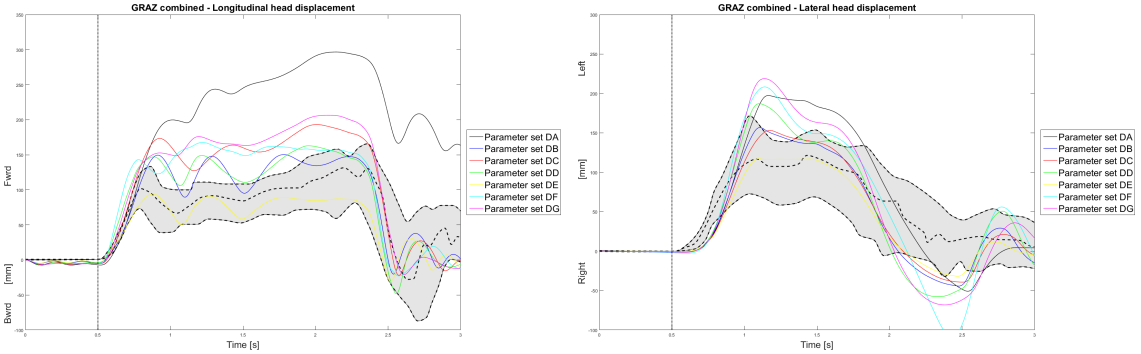

(a) Longitudinal head displacement. **(b)** Lateral head displacement.

Figure 4.6: Head displacement of the double pendulum compared to the corridor (gray area) of the head displacement in volunteer dataset *No.*(5) *Graz study*, a combined maneuver. The vertical line corresponds to the maneuver onset time.

T1 displacement

The response for the longitudinal T1 displacement in the lane-change maneuver, as seen in Figure 4.7a, has a similar dynamic response in terms of magnitude without any delays. The lateral T1 response in Figure 4.7b shows that the response is somewhat underestimated for all parameter sets. Again for the longitudinal T1 displacement response to the braking maneuver as presented in Figure 4.8, the model gives a proper response with respect to the dynamics. However, the response is oscillating.

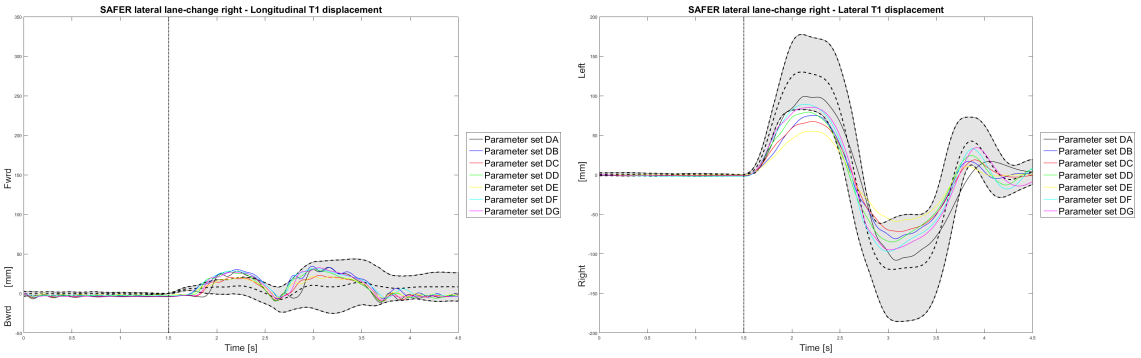

(a) Longitudinal T1 displacement. **(b)** Lateral T1 displacement.

Figure 4.7: T1 displacement of the double pendulum compared to the corridor (gray area) of the T1 displacement in volunteer dataset *No.*(3) *SAFER lateral*, a lane-change maneuver. The vertical line corresponds to the maneuver onset time.

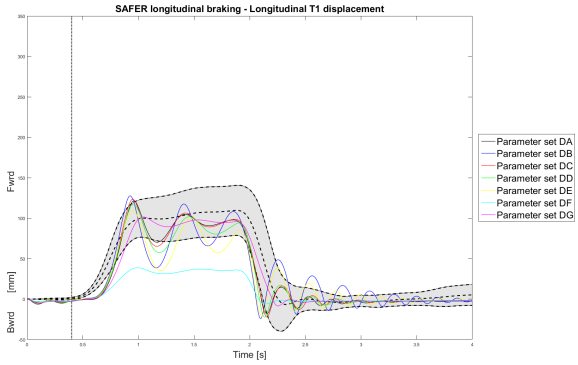

Figure 4.8: T1 displacement of the single pendulum compared to the corridor (gray area) of the T1 displacement in volunteer dataset *No.*(1) *SAFER longitudinal*, an emergency braking maneuver. The vertical line corresponds to the maneuver onset time.

4.3 ERR test

Figures 4.9 and 4.10 demonstrate the T1 displacement for the double pendulum, parameter sets *DA, DC, DF* and *DG*, when running simulations using the ERR belt and the standard belt configuration. Simulations of parameter sets *DB*, *DD*, and *DE* are presented in Appendix E.

The occupant model is slightly pulled back by the belt after ERR has been activated, as can be seen in particular for the longitudinal displacement of parameter set *DF*. Moreover,

the displacement is reduced in both longitudinal and lateral direction during the maneuver for all parameter sets.

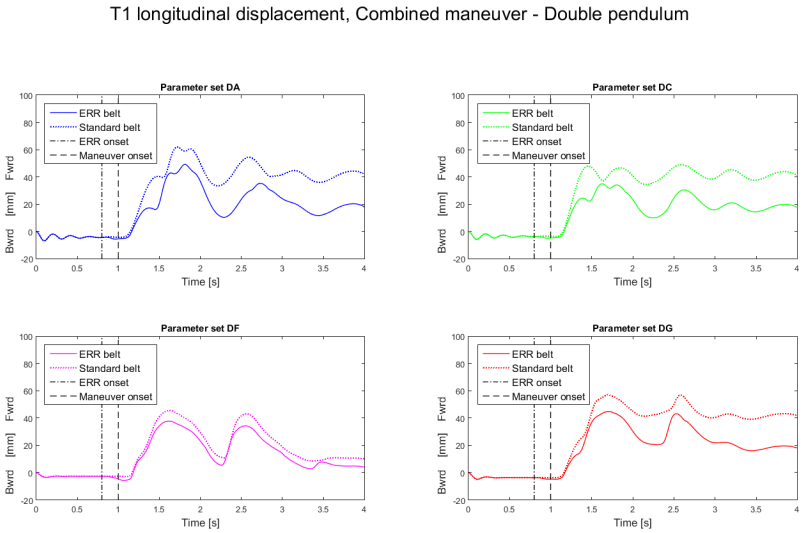

Figure 4.9: Longitudinal displacement of T1 for the double pendulum model, where the solid line is the response with ERR, and the dotted line is with a standard belt.

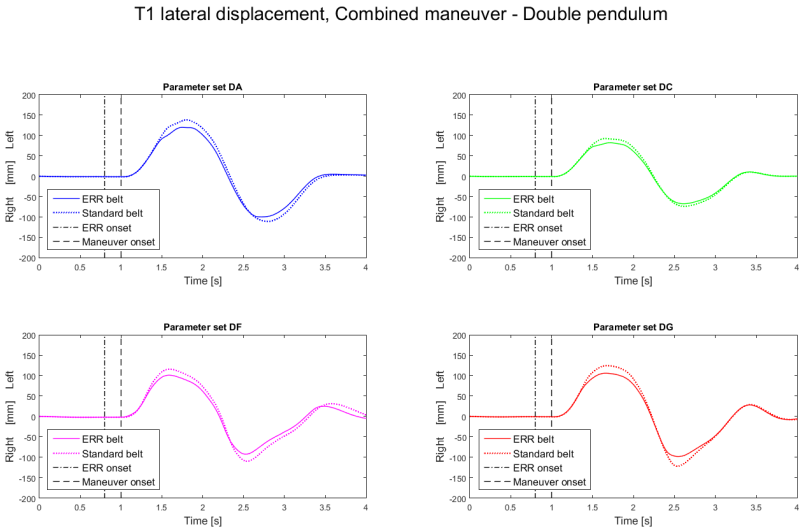

Figure 4.10: Lateral displacement of T1 for the double pendulum model, where the solid line is the response with ERR, and the dotted line is with a standard belt.

5| Discussion

This chapter will present a discussion about the modeling approach of the simplified occupant kinematic model. Furthermore, a discussion about the results will be brought up and lastly, proposals for further development will be suggested.

5.1 Methods discussion

When studying the kinematic behavior of a seated human, parallels can be drawn to an inverted spherical pendulum. Assuming that the hip of the occupant when seated in a car is fixed to the seat, and the flexion of the spine is modest, then the upper body geometry is basically a lever with a distributed mass. Together with support from studies, where human balance and locomotion have been simulated using inverted pendulum models (see section 3.1), the idea to the design of the simplified occupant kinematic model was initiated.

In order to build a computationally efficient model that was able capture such an advanced system as the human occupant kinematics, simplifications and generalization were necessary. First, rigid bodies were used for the occupant pendulum. This implied that the pendulum would not be able to bend in the same way as a human, to capture such movement, as slouching of the back or extension and flexion of the neck as mentioned in section 2.2 and as seen in Figure 2.2. The fixation of the hip point was regarded as a minor simplification with regards to volunteer test results showing minimal or no slip at low acceleration levels, as observed in section 2.2. The non-linear characteristic of the volunteer muscular response cannot be fully captured with the linear spring-damper pairs. However, these components allowed for straightforward tuning of the model.

Desirably the anthropometric data, i.e. the initial position coordinates of the hip point, sternum, T1 and the head CoG, from each volunteer would have been used to set the size of the occupant pendulum when tuning the model. Then it would have been possible to include the length of the pendulum in the parameter sets. As of now, the dimensions of the pendulum are based on the SAFER HBM and are the same for each parameter set. An advantage of having the same pendulum size for each parameter set was that the parameter sets were then more intuitively comparable. For example, as seen in Table 4.2, parameter set *DE* seems to be stiffer than parameter set *DG* based on the values of the spring coefficients $k_{\theta_1}, k_{\varphi}, k_{\theta_2}$. This is confirmed as the displacements of parameter set *DE* are lower than the displacements of *DG* in Figures 4.4, 4.5, 4.6, 4.7 and 4.8.

The modeling of the seat required some generalizations. Firstly the most important function for the seat is to prevent the occupant pendulum from falling backwards towards the south-pole position. Another function is to some extent prevent the occupant pendulum from moving laterally when it is leaning against the seat. However, the widths of the occupants in the volunteer study were unknown, as well as the friction between the seat and the occupant, thus the relative movement between the occupant and the seat was unknown. To generalize this characteristic three planes were used, one as the flat backrest and two symmetrically angled planes as the side barriers. The width parameter, γ_{seat}, of the backrest was tuned to optimize the response of the model. The results suggest that

this was a valid assumption for the double pendulum since the values for γ_{seat} vary for the parameter sets in Table 4.2. However, as seen in Table 4.1, this parameter does not vary for the single pendulum model which suggests that it may be a redundant parameter for this model.

Also the seat belt model was generalized. First, the area where the seat belt force is applied was reduced to one point, since the pendulum lacks a width to enable for a distributed force. This further disables any rotation of the occupant model as an effect of the asymmetric seat belt force distribution mentioned in section 2.2. Moreover, the belt cannot slide on the chest nor slip off the shoulder. These aspects could be valuable to predict, however not included in the scope of this work. Furthermore, the lap belt was omitted for the model as a consequence of the fixed hip position.

Although simplifications were made, the tuning of the spring-damper pairs and the backrest width of the model compensated for many phenomena of the occupant kinematics. This was also confirmed by the results for both the single and the double pendulum.

The approach to use a rigid body inverted pendulum for modeling the occupant has the advantages of being physically intuitive and computationally efficient. However, besides not allowing for any deformation, the inverted spherical pendulum owns the characteristic of being unstable which infers that without any restraints it would return to its stable point, i.e. pointing straight downwards. This instability was compensated for by the spring-damper pairs, the seat, and the seat belt since they force the pendulum back toward the initial position. The upper rod of the double pendulum is not as restrained as the lower rod and thus exhibits a more unstable behavior. To prevent this behavior a hinge joint, which is more numerically stable than the spherical joint, was applied as the "neck-joint". This allowed for a longitudinal relative motion between the head and T1.

5.1.1 Tuning of model

The tuning of the model was executed with respect to a set of 24 volunteer evasive maneuver tests, consisting of 9 male subjects. This produced 24 parameter sets that correspond to the characteristics of each of the volunteers in the tests. The decision to tune the model based on each individual test, and later select a family of seven parameter sets among them, was made in order to produce a family of parameter sets that would represent a variation in occupant kinematics. However, this family does not represent any specific population group. In order to make the model more representative for the entire population, a larger dataset which includes female volunteer data and different sized volunteers, i.e. volunteers that represent a wider range of statures, is needed.

Despite the small number of volunteers that were included in the tuning dataset, there were still clear variations in the kinematic behavior. This implied that the model, as it is, was nevertheless able to capture a wide spectrum of occupant responses.

5.2 Results discussion

The results of the single pendulum model in section 4.1 showed that the single pendulum lateral displacement coincided well with the reference data. However, the longitudinal displacement was limited, as seen in Figure 4.2. The maximum mean longitudinal displacement of the reference data was approximately 170 mm during the maneuver, but the model responded with a displacement of approximately 40 mm below this level for most parameter sets. The believed reason behind the limitation is that the seat belt force becomes too high at this longitudinal displacement. This may be due to that one of the tuning states is the seat belt force. Hence this resulted in a compromise of both the longitudinal displacement and the seat belt force responses, as neither of them will therefore be highly inaccurate but also, one repose will not be highly accurate while the other is highly inaccurate. This means that the overall dynamic response can be captured but the magnitude of the response might be underestimated.

The double pendulum model results, as stated in section 4.2, show a wider spectrum of responses compared to the single pendulum, especially for the longitudinal head displacement. For the longitudinal T1 displacement, the model response was satisfactory however, the lateral displacement was somewhat underestimated. Since it was possible for the head and T1 to move relative one another, the head displacement was improved compared to the single pendulum. Just as for the single pendulum, the phenomena of the seat belt force remained and limited the longitudinal movement of the lower pendulum rod to some extent, i.e. T1 displacement, but the added hinge joint allowed for further movement of the head. The spring-damper coefficients of the "neck-joint" were presumably given values which let the upper rod compensate for the lack of longitudinal motion of the lower rod, as a consequence of the "seat belt effect". A fallout might be that the longitudinal head displacement in other maneuvers may be overestimated, which applied for the responses in Figure 4.6a. The double pendulum model is more unstable than the single pendulum model, which is presumably one reason for the oscillating property of the head CoG and T1 responses, as seen in Figures 4.5 and 4.8. However, the outcome of these oscillations are not regarded as having a negative outcome on the results of the model response.

As a part of the validation it was of interest to study pure braking maneuvers to understand if the seat belt model interferes with the occupant pendulum model response, i.e. if it introduces any unwanted lateral displacement during pure braking maneuvers. Considering that the seat belt force is applied in the sternum point and the force direction is the resultant of two vectors as described in section 3.1.2, the concern was that it would impose unwanted lateral movement when no lateral acceleration was present. However, as seen in Figure 5.1 which shows the lateral head displacement response of the single pendulum and the double pendulum models during a braking maneuver (dataset $No.(1)$), the lateral displacement is below 15 mm during the entire maneuver. This implies that the seat belt model behaves as expected, i.e. no lateral displacement is induced by the seat belt.

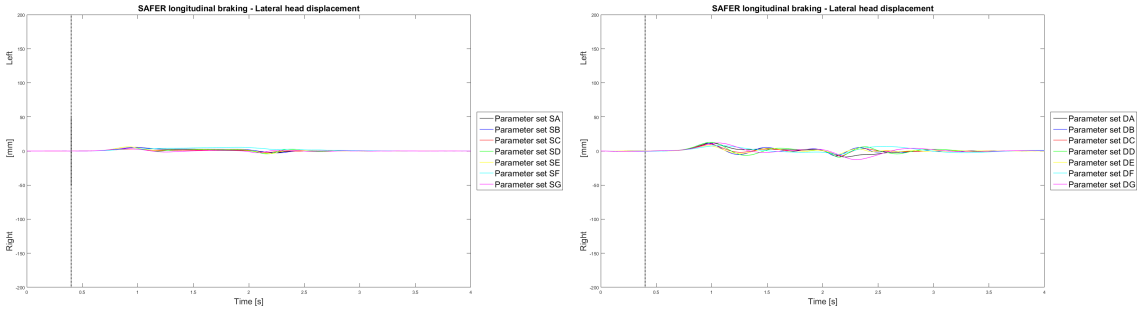

(a) Lateral head displacement of the single pendulum model.

(b) Lateral head displacement of the double pendulum model.

Figure 5.1: Lateral head displacement for the models when subjected to a pure braking maneuver, dataset *No.*(1).

When the ERR is activated, similarly to the volunteer response as seen in section 2.3.1, a backward motion of the occupant pendulum T1 point was observed. However, the model T1 displacement reduction was not as distinct as for the volunteers. One reason for this result could be that the input mean acceleration for the model was lower than that of the volunteer maneuver study, i.e. 0.5 g versus 1 g. Furthermore, the large reduction of displacement in the volunteer tests when ERR is used, may be due to that muscle activity was initialized earlier when ERR is active, as stated in section 2.3.1. This possibly affected the volunteer stiffness. If this is the case, the model would need to be re-tuned to obtain new parameter sets that would compensate for the change in muscular activity. The model, as it is, can be used to provide a first prediction of the effect of ERR for different maneuvers.

5.3 Future work

The applicability of the model would be improved by tuning the model for a wider range of occupants, including females and a greater variety of stature. This would generate more datasets for selection of the family of parameter sets, and as a suggestion two groups of parameter sets representing males and females respectively. Furthermore, to make use of the driver model, parameter tuning and validation is required using adequate data, i.e. driver's kinematic data. Note that the driver's arms model extend the parameter sets with two coefficients, i.e. the related spring and damper coefficients. This is only possible once volunteer data representing drivers subjected to combined maneuvers becomes available.

The seat belt model could potentially be improved by modeling belt slip-off and gliding against the chest. If gliding was possible, the limitation of the longitudinal displacement for both models may be improved. Furthermore, it is important to be aware of when belt slip-off occurs, and implementing this approach in the model could be valuable.

The response when having the ERR model could potentially be improved by re-tuning the model with respect to volunteer datasets which include an ERR belt. This would provide another set of parameters which correspond to occupants restrained by the ERR belt.

To allow for an enhancement of the dynamic representation of the occupant kinematics, the modeling of the muscle response could be developed. A suggestion is to study the

muscle response data as collected by Östh *et al.* (2013) and Olafsdottir *et al.* (2013) to identify activation times and magnitudes of voluntary muscular reflexes. Accordingly, a type of "muscle response level model" could be designed and applied to the spring-damper pairs. The spring-damper pairs could in this way be tuned with varying stiffness and damping contributions over the time of the maneuver.

To further improve on the kinematic response the occupant could be modeled as a triple pendulum. The first rod would connect the hip and sternum, the second rod would be sternum to T1, and the third rod joins T1 and the head CoG. This would allow the occupant model to better capture the slouching of the occupant during a maneuver. However, this approach would require volunteer kinematic data that corresponds to to the sternum point in addition to the point of T1 and the head CoG, which is not yet available.

6| Conclusion

The development of the simplified occupant kinematic model resulted in a system that includes an occupant model derived as an inverted spherical pendulum, and restraint models - the seat, the seat belt, and driver's arms - applied as generalized forces. The occupant model was first derived as a single pendulum, and then further developed into a double pendulum. The model was tuned using pre-existing front seat passenger kinematic data from volunteer maneuver tests, corresponding to a combined maneuver. The computation time of the simplified occupant kinematic model, either the single pendulum model or the double pendulum model, was 0.7 seconds for a maneuver with an approximate duration of 4 seconds.

The results from the simulations showed that both designs of the pendulum model designs were able to capture the dynamics of the occupant head kinematics during a pre-crash maneuver by means of head displacement. However, the double pendulum captured the longitudinal displacement to a greater extent than the single pendulum model although the displacement was overestimated for some maneuvers. Since a larger displacement of the head is more critical for the occupant when facing a potential crash, an overestimation of the displacement is preferred rather than an underestimation. Furthermore, the double pendulum was able to capture the T1 displacement in addition to the head displacement, and the responses showed a wider spread of the displacements for the obtained parameter sets. Therefore, the double pendulum is suggested as the model of choice.

The seat belt model and the ERR model were evaluated and compared, in which the seat belt model obtained expected behaviour, while the ERR belt did not reduce the displacement of T1 as much as desired.

With respect to the stated conclusions, the simplified occupant kinematic model which was developed can be a suitable tool for running a large number of pre-crash maneuver simulations.

References

Angelaki, D. E., & Cullen, K. E. (2008). Vestibular system: the many facets of a multimodal sense. *Annu. Rev. Neurosci.*, *31*, 125–150.

Antona, J., Ejima, S., & Zama, Y. (2011). Influence of the driver conditions on the injury outcome in front impact collisions. *International Journal of Automotive Engineering*, *2*(2), 33–38.

Aust, M. L., Jakobsson, L., Lindman, M., & Coelingh, E. (2015). *Collision avoidance systems-advancements and efficiency* (Tech. Rep.). SAE Technical Paper.

Cavagna, G. A., Thys, H., & Zamboni, A. (1976). The sources of external work in level walking and running. *The Journal of physiology*, *262*(3), 639–657.

Cicchino, J. B. (2016). Effectiveness of forward collision warning systems with and without autonomous emergency braking in reducing police-reported crash rates. *Arlington, VA: Insurance Institute for Highway Safety*.

Eberhart, R., & Shi, Y. (2001). Particle Swarm Optimization: Developments, Applications and Resources. In *Evolutionary Computation, 2001. Proceedings of the Congress on Evolutionary Computation* (Vol. 1, p. 81-86). IEEE.

Ejima, S., Ono, K., Holcombe, S., Kaneoka, K., & Fukushima, M. (2007). A study on occupant kinematics behaviour and muscle activities during pre-impact braking based on volunteer tests. In *Proceedings of the 2007 International IRCOBI Conference on the Biomechanics of Impact, September, Maastricht, the Netherlands.*

European Road Safety Observatory. (2017). *Annual Accident Report 2017.*

Fine, I., & Boynton, G. (2009). *Model fitting.* Retrieved 2018-05-03, from `https://courses.washington.edu/matlab1/ModelFitting.html#20`

Ghaffari, G., Brolin, K., Bråse, D., Pipkorn, B., Svanberg, B., Jakobsson, L., & Davidsson, J. (2018). Passenger kinematics in Lane change and Lane change with Braking Manoeuvres using two belt configurations: standard and reversible pre-pretensioner. In *Proceedings of the 2018 International IRCOBI Conference on the Biomechanics of Impact, September 12-14, Athens, Greece.*

Goldstein, H., Poole, C., & Safko, J. (2000). *Classical Mechanics, third edition.* Addison Wesley.

Greiner, W. (2003). *Classic Mechanics: Systems of Particles and Hamiltonian Dynamics.* Springer.

Håland, Y. (2006). The evolution of the three point seat belt from yesterday to tomorrow. In *Proceedings of the 2006 International IRCOBI Conference on the Biomechanics of Impact, Sept 20-22, Madrid, Spain.*

Huber, P., Kirschbichler, S., Prüggler, A., & Steidl, T. (2015). Passenger kinematics in braking, lane change and oblique driving maneuvers. In *Proceedings of IRCOBI Conference, Sept 9-11 2015, Lyon, France.*

Iraeus, J., Davidsson, J., & Brolin, K. (2017). Recent HBM Activities at Chalmers University. In *Presentation at the Human Body Modelling in Automotive Safety Conference, November 28-29, 2017, Berlin, Germany.*

Isaksson-Hellman, I., & Lindman, M. (2016). Using insurance claims data to evaluate the collision-avoidance and crash-mitigating effects of Collision Warning and Brake Support combined with Adaptive Cruise Control. In *Intelligent Vehicles Symposium (IV), 2016 IEEE* (pp. 1173–1178).

Iwamoto, M., Kisanuki, Y., Watanabe, I., Furusu, K., Miki, K., & Hasegawa, J. (2002). Development of a finite element model of the total human model for safety (THUMS)

and application to injury reconstruction. *Proceedings of the 2002 International Research Council on Biomechanics of Injury, Munich, Germany*, 31–42.

Jazar, R. (2017). *Vehicle Dynamics Theory and Application, Third edition.* Springer International Publishing AG.

Kennedy, J., & Eberhart, R. (1995). Particle Swarm Optimization. In *Neural Networks, 1995. Proceedings of IEEE International Conference on Neural Network* (Vol. 6, p. 1942-1948). IEEE.

Keshner, E. A. (2009). Vestibulocollic and cervicocollic control. In *Encyclopedia of Neuroscience* (pp. 4220–4224). Springer Berlin Heidelberg.

Keysight Technologies. (2016). *Keysight Spectrum Analysis Basics - Application note 150.* `http://literature.cdn.keysight.com/litweb/pdf/5952-0292.pdf`. (Accessed: 2018-05-30)

Krafft, M., Kullgren, A., Lie, A., Strandroth, J., & Tingvall, C. (2009). The effects of automatic emergency braking on fatal and serious injuries. In *21st International Conference on Enhanced Safety of Vehicles.*

Landau, L., & Lifshitz, E. (1976). *Mechanics, third edition* (Vol. 1).

Mages, M., Seyffert, M., & Class, U. (2011). Analysis of the pre-crash benefit of reversible belt pre-pretensioning in different accident scenarios. In *Proceedings of the 22nd ESV-Conference, June 13-16 2011, Washington D.C., USA.*

MathWorks. (2018). *Choose a Solver.* `https://se.mathworks.com/help/simulink/ug/types-of-solvers.html#responsive_offcanvas`. (Accessed: 2018-06-04)

McGrath, M., Howard, D., & Baker, R. (2015). The strengths and weaknesses of inverted pendulum models of human walking. *Gait & Posture*, *41*(2), 389–394.

Muggenthaler, H., Adamec, J., Praxl, N., & Schönpflug, M. (2005). The influence of muscle activity on occupant kinematics. In *Proceedings of the International IRCOBI Conference on the Biomechanics of Impact, Sept 21-23, Prague, Czech Republic.*

Ólafsdóttir, J. M. (2017). *Muscle responses in dynamic events: Volunteer experiments and numerical modeling for the advancement of human body models for vehicle safety assessment (Doctoral dissertation).* Chalmers University of Technology. Available from Chalmers Publication Library.

Ólafsdóttir, J. M., Östh, J., Davidsson, J., & Brolin, K. (2013). Passenger kinematics and muscle responses in autonomous braking events with standard and reversible pretensioned restraints. In *Proceedings of the 2013 International IRCOBI Conference on the Biomechanics of Impact, Sept 11-13, Gothenburg, Sweden* (pp. 602–617).

Östh, J. (2014). *Muscle responses of car occupants: Numerical modeling and volunteer experiments under pre-crash braking conditions (Doctoral dissertation).* Chalmers University of Technology. Available from Chalmers Publication Library.

Östh, J., Brolin, K., Carlsson, S., Wismans, J., & Davidsson, J. (2012). The occupant response to autonomous braking: a modeling approach that accounts for active musculature. *Traffic Injury Prevention*, *13*(3), 265–277.

Östh, J., Ólafsdóttir, J. M., Davidsson, J., & Brolin, K. (2013). *Driver kinematic and muscle responses in braking events with standard and reversible pre-tensioned restraints: validation data for human models* (Tech. Rep.). SAE Technical Paper.

Östmann, M., & Jakobsson, L. (2016). An examination of pre-crash braking influence on occupant crash response using an active human body model. In *Proceedings of the 2016 International IRCOBI Conference on the Biomechanics of Impact, Sept 14-16, Malaga, Spain.*

Peterka, R. (2002). Sensorimotor integration in human postural control. *Journal of neurophysiology*, *88*(3), 1097–1118.

Sayers, M. (1996). Standard terminology for vehicle dynamics simulations. *The University of Michigan Transportation Research Institute (UMTRI), Tech. Rep*.

Schoeneburg, R., Baumann, K.-H., Fehring, M., Ag, D., & Cars, M. (2011). The Efficiency of PRE-SAFE Systems in Pre-braked Frontal Collision Situations. *Proceedings of the 22nd International Techical Conference on the Enhanced Safety of Vehicles (ESV), June 13-16 2011, Washington D.C., USA*(11-0207).

Steele, K., & Werndl, C. (2016). Model tuning in engineering: Uncovering the logic. *The Journal of Strain Analysis for Engineering Design*, *51*(1), 63-71.

Stutts, D. (2017). Analytical Dynamics: Lagrange's Equation and its Application – A Brief Introduction.

Svensson, L. G. (1978). *Means for effective improvement of the three-point seat belt in frontal crashes* (Tech. Rep.). SAE Technical Paper.

Van Rooij, L., Elrofai, H., Philippens, M., & Daanen, H. (2013). Volunteer kinematics and reaction in lateral emergency maneuver tests. *Stapp Car Crash Journal*, *57*, 313.

World Health Organization. (2015). *Global Status Report on Road Safety 2015*.

Wylie, D. R. W. (2009). Visual-vestibular interaction. In *Encyclopedia of Neuroscience* (pp. 4349–4353). Springer Berlin Heidelberg.

A| Appendix 1

A.1 General plane motion

The general plane motion is the translation and rotation of a rigid body in a two dimensional plane. The motion can be decomposed into the superposition of one translating motion and a rotational motion. Here follows the derivation of the equations which describe the general plane motion.

A.1.1 Motion relative a moving reference frame

A starting point to derive the equations describing general plane motion is to consider the motion relative a moving reference frame. Consider particle A and B in Figure A.1, which are moving along two independent trajectories in the plane with the fixed reference frame (x, y). Let $\boldsymbol{r}_A$ and $\boldsymbol{r}_B$ be the position vector of the particles A and B in the fixed reference frame. Attach a non-rotating reference frame in particle B, the position of particle A can now be described by the position vector $\boldsymbol{r}_{A/B}$ which is a position vector of particle A in the moving reference frame of particle B. The position vector $\boldsymbol{r}_{A/B}$ can be expressed as

$$\boldsymbol{r}_{A/B} = x'\hat{\boldsymbol{e}}'_1 + y'\hat{\boldsymbol{e}}'_2 \tag{A.1}$$

where $\hat{\boldsymbol{e}}'_1$ and $\hat{\boldsymbol{e}}'_2$ are the basis vectors of the moving reference frame. Observe that since the moving reference frame is non-rotating, as the basis vectors do not change in time. Taking the derivative of the position yields the velocity as

$$\boldsymbol{v}_{A/B} = \frac{dx'}{dt}\hat{\boldsymbol{e}}'_1 + \frac{dy'}{dt}\hat{\boldsymbol{e}}'_2 \tag{A.2}$$

which can be interpreted as the velocity of particle A relative to B. Now the position of A can be expressed as

$$\boldsymbol{r}_A = \boldsymbol{r}_B + \boldsymbol{r}_{A/B} \tag{A.3}$$

and by differentiating this expression the velocity and acceleration of A is obtained

$$\boldsymbol{v}_A = \boldsymbol{v}_B + \boldsymbol{v}_{A/B} \tag{A.4}$$

$$\boldsymbol{a}_A = \boldsymbol{a}_B + \boldsymbol{a}_{A/B} \tag{A.5}$$

these equations describe the motion of particle A observed relative a moving particle B.

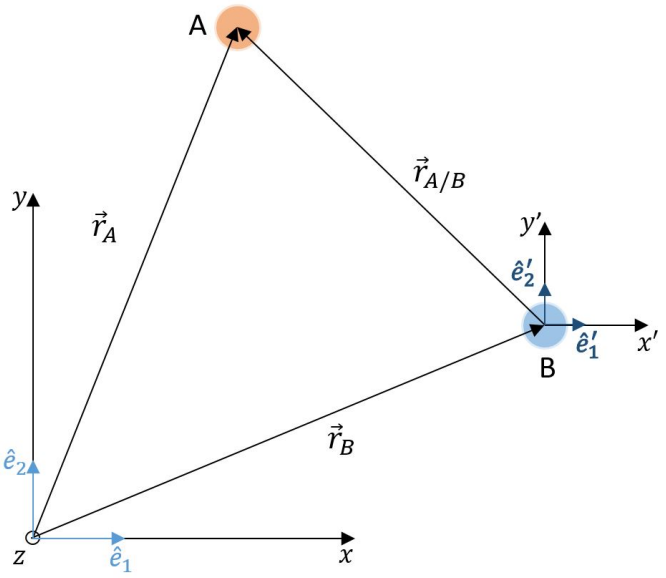

Figure A.1: Motion of a particle relative a moving reference.

Now consider a rigid body undergoing plane motion, see Figure A.2a. The position of the two lines on the body can be specified by the two angles θ_1 and θ_2 measured from the x-axis in a fixed reference frame. The angle β in between the two lines relates θ_1 and θ_2 in the following manner

$$\theta_2 = \beta + \theta_1 \tag{A.6}$$

Since the body is rigid this preserves the distance between the lines, i.e. β is constant and differentiation of Eq.(A.6) yields

$$\frac{d\theta_1}{dt} = \frac{d\theta_2}{dt} \tag{A.7}$$

$$\frac{d^2\theta_1}{dt^2} = \frac{d^2\theta_2}{dt^2} \tag{A.8}$$

This holds for any pair of lines in the body which implies that the body can be associated with a unique angular velocity $\boldsymbol{\omega}$, defined as

$$\boldsymbol{\omega} = \omega\hat{\boldsymbol{e}}_3 = \frac{d\theta_1}{dt}\hat{\boldsymbol{e}}_3 \tag{A.9}$$

where $\hat{\boldsymbol{e}}_3$ is the basis vector perpendicular to the plane. Arguing analogously the body can be associated with a unique angular acceleration $\dot{\boldsymbol{\omega}}$, defined as

$$\dot{\boldsymbol{\omega}} = \frac{d\omega}{dt}\hat{\boldsymbol{e}}_3 = \frac{d^2\theta_1}{dt^2}\hat{\boldsymbol{e}}_3 \tag{A.10}$$

and thus all lines on a rigid body in plane motion have the same angular displacement, velocity, and acceleration, see Figure A.2b. Now consider the motion of a rigid body as shown in figure A.2c with a point B_0 taken as a reference. The motion can be considered to occur in two stages, one pure translation of an arbitrary line A_0B_0 and one rotation about the point B_1 giving the final position A_1B_1. The motion is thus the sum of the translation of the reference B_0 described by the velocity and acceleration $\boldsymbol{v}_B$ and $\boldsymbol{a}_B$ and the rotation characterized by the angular velocity and acceleration $\boldsymbol{\omega}$ and $\dot{\boldsymbol{\omega}}$ of the body. This means that the motion of an arbitrary point within the rigid body is known when the translation components, $\boldsymbol{v}_B$ and $\boldsymbol{a}_B$ and rotation components, $\boldsymbol{\omega}$ and $\dot{\boldsymbol{\omega}}$, are known.

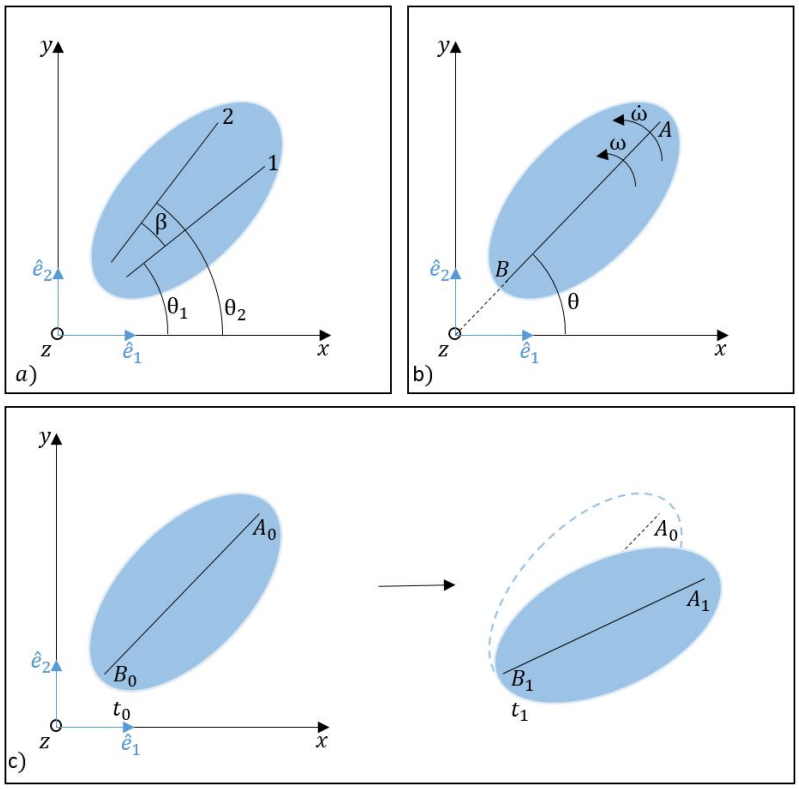

Figure A.2: Decomposition of rigid body motion.

A.1.2 Velocities and accelerations

To derive the equations that describe the motion in the plane, consider Figure A.3. The figure is a schematic representation of a rigid body moving in the plane with an angular velocity and acceleration, $\boldsymbol{\omega}$ and $\dot{\boldsymbol{\omega}}$, about the point B. Recall that the position and velocity of A in the fixed reference frame now can be expressed as

$$\boldsymbol{r}_A = \boldsymbol{r}_B + \boldsymbol{r}_{A/B} \tag{A.11}$$

$$\boldsymbol{v}_A = \boldsymbol{v}_B + \boldsymbol{v}_{A/B} \tag{A.12}$$

where the index A/B means the position or velocity of A relative to B. As the rigid body moves, A traces a circular path relative to B. Since the rigid body does not deform in any way, the radius of that path is the length of the vector $\boldsymbol{r}_{A/B}$, i.e. $|\boldsymbol{r}_{A/B}|$. The angular velocity of this motion is $\boldsymbol{\omega}$ and the tangential velocity of A, $\boldsymbol{v}_{A/B}$, is the time derivative of the rotating position vector $\boldsymbol{r}_{A/B}$, which is

$$\boldsymbol{v}_{A/B} = \frac{d\boldsymbol{r}_{A/B}}{dt} = \boldsymbol{\omega} \times \boldsymbol{r}_{A/B} \tag{A.13}$$

Now the velocity of A can be expressed as

$$\boldsymbol{v}_A = \boldsymbol{v}_B + \boldsymbol{\omega} \times \boldsymbol{r}_{A/B} \tag{A.14}$$

which is the sum of a translational component $\boldsymbol{v}_B$ and the rotational component $\boldsymbol{\omega} \times \boldsymbol{r}_{A/B}$ of the motion. The acceleration of A in the fixed frame can be derived by an analogous procedure. The acceleration of A is simply the time derivative of the velocity of A, recall Eq.(A.5)

$$\boldsymbol{a}_A = \boldsymbol{a}_B + \boldsymbol{a}_{A/B} \tag{A.15}$$

where $\boldsymbol{a}_{A/B}$ is the time derivative of $\boldsymbol{v}_{A/B}$ which can be expressed as

$$\boldsymbol{a}_{A/B} = \frac{d(\boldsymbol{\omega} \times \boldsymbol{r}_{A/B})}{dt} = \frac{d\boldsymbol{\omega}}{dt} \times \boldsymbol{r}_{A/B} + \boldsymbol{\omega} \times \frac{d\boldsymbol{r}_{A/B}}{dt} = \dot{\boldsymbol{\omega}} \times \boldsymbol{r}_{A/B} + \boldsymbol{\omega} \times (\boldsymbol{\omega} \times \boldsymbol{r}_{A/B}) \quad \text{(A.16)}$$

This yields the resulting expression for the acceleration of point A

$$\boldsymbol{a}_A = \boldsymbol{a}_B + \dot{\boldsymbol{\omega}} \times \boldsymbol{r}_{A/B} + \boldsymbol{\omega} \times (\boldsymbol{\omega} \times \boldsymbol{r}_{A/B}) \quad \text{(A.17)}$$

and as for the velocity the acceleration is the sum of a translational component $\boldsymbol{a}_B$ and a rotational component $\dot{\boldsymbol{\omega}} \times \boldsymbol{r}_{A/B} + \boldsymbol{\omega} \times (\boldsymbol{\omega} \times \boldsymbol{r}_{A/B})$.

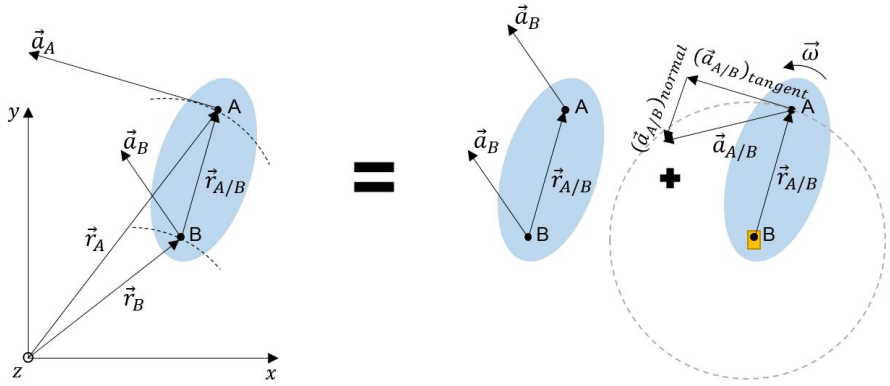

Figure A.3: Decomposition of the general plane acceleration of point A relative the reference point B.

B| Appendix 2

B.1 Fictitious forces in an accelerating reference frame

To derive the fictitious forces that may appear in an accelerating reference frame, first consider the rotation of an ordinary Cartesian reference frame, denoted by the axes (x, y, z), about the origin. The rotating reference system is denoted by the axes (x', y', z') as shown in Figure B.1. Note that the two coordinate origins coincide for the case of pure rotation. For further readability the inertial reference system will be denoted I, and the moving frame will be denoted M. For an observer resting in the primed reference frame, a vector $\boldsymbol{A}(t)$ with its components $(A'_1(t), A'_2(t), A'_3(t))$ that change with time can be represented as follows

$$\left.\frac{d\boldsymbol{A}}{dt}\right|_M = \frac{dA'_1}{dt}\boldsymbol{e}'_1 + \frac{dA'_2}{dt}\boldsymbol{e}'_2 + \frac{dA'_3}{dt}\boldsymbol{e}'_3 \tag{B.1}$$

where the index M refers to that the derivative is calculated in the moving reference frame.

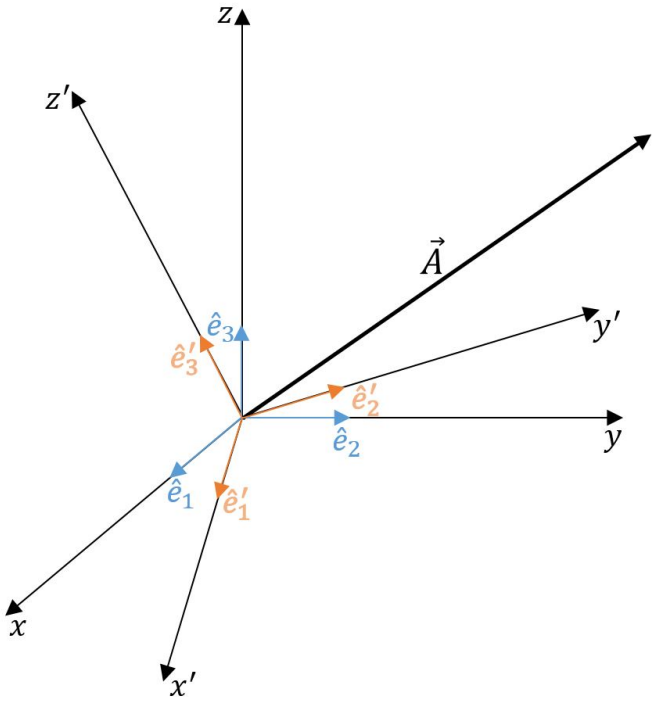

Figure B.1: Relative position of the reference frames with coordinates (*x,y,z*) and (*x'*,*y'*,*z'*).

Now, for the inertial reference frame both the vector $\boldsymbol{A}(t)$ and the unit vectors $(\boldsymbol{e}'_1, \boldsymbol{e}'_2, \boldsymbol{e}'_3)$ change with time. Hence when differentiating $\boldsymbol{A}(t)$ the unit vectors should be differentiated as well, thus we need to use the product rule for differentiation

$$\left.\frac{d\boldsymbol{A}}{dt}\right|_I = \frac{dA'_1}{dt}\boldsymbol{e}'_1 + \frac{dA'_2}{dt}\boldsymbol{e}'_2 + \frac{dA'_3}{dt}\boldsymbol{e}'_3 + A'_1\dot{\boldsymbol{e}}'_{\mathbf{1}} + A'_2\dot{\boldsymbol{e}}'_{\mathbf{2}} + A'_3\dot{\boldsymbol{e}}'_{\mathbf{3}} \tag{B.2}$$

which yields the following results

$$\left.\frac{d\boldsymbol{A}}{dt}\right|_I = \left.\frac{d\boldsymbol{A}}{dt}\right|_M + A'_1\dot{\boldsymbol{e}}'_{\mathbf{1}} + A'_2\dot{\boldsymbol{e}}'_{\mathbf{2}} + A'_3\dot{\boldsymbol{e}}'_{\mathbf{3}} \tag{B.3}$$

Since the following generally holds: $d/dt(\boldsymbol{e}_i' \cdot \boldsymbol{e}_i') = \boldsymbol{e}_i' \cdot \dot{\boldsymbol{e}}_{\boldsymbol{i}}' + \boldsymbol{e}_i' \cdot \dot{\boldsymbol{e}}_{\boldsymbol{i}}' = d/dt(1) = 0$. Hence $\boldsymbol{e}_i' \cdot \dot{\boldsymbol{e}}_i' = 0$, i.e. the derivative of a unit vector is always orthogonal to the vector itself and thus the derivative can be written as linear combinations of two other unit vectors. This can be expressed as follows

$$\dot{\boldsymbol{e}}_{\boldsymbol{1}}' = a_1 \boldsymbol{e}_{\boldsymbol{2}}' + a_2 \boldsymbol{e}_{\boldsymbol{3}}' \tag{B.4}$$

$$\dot{\boldsymbol{e}}_{\boldsymbol{2}}' = a_3 \boldsymbol{e}_{\boldsymbol{1}}' + a_4 \boldsymbol{e}_{\boldsymbol{3}}' \tag{B.5}$$

$$\dot{\boldsymbol{e}}_{\boldsymbol{3}}' = a_5 \boldsymbol{e}_{\boldsymbol{1}}' + a_6 \boldsymbol{e}_{\boldsymbol{2}}' \tag{B.6}$$

This yields that only 3 of the coefficients $a_1, a_2, ..., a_6$ are independent. This is done by first differentiating $\boldsymbol{e}_1' \cdot \boldsymbol{e}_2' = 0$ which yields

$$\dot{\boldsymbol{e}}_1' \cdot \boldsymbol{e}_2' = -\dot{\boldsymbol{e}}_2' \cdot \boldsymbol{e}_1' \tag{B.7}$$

Now, by multiplying Eq.(B.4) and correspondingly Eq.(B.5) by $\boldsymbol{e}_{\boldsymbol{1}}'$ results in

$$\boldsymbol{e}_2' \cdot \dot{\boldsymbol{e}}_1' = a_1 \quad \text{and} \quad \boldsymbol{e}_1' \cdot \dot{\boldsymbol{e}}_2' = a_3 \tag{B.8}$$

and thus $a_3 = -a_1$. By an analogous procedure one find the that the following is true as well, $a_5 = -a_2$ and $a_6 = -a_4$. The time derivative in the inertial reference frame of $\boldsymbol{A}(t)$ can now be expressed as follows

$$\left.\frac{d\boldsymbol{A}}{dt}\right|_I = \left.\frac{d\boldsymbol{A}}{dt}\right|_M + A_1'(a_1 \boldsymbol{e}_{\boldsymbol{2}}' + a_2 \boldsymbol{e}_{\boldsymbol{3}}') + A_2'(a_3 \boldsymbol{e}_{\boldsymbol{1}}' + a_4 \boldsymbol{e}_{\boldsymbol{3}}') + A_3'(a_5 \boldsymbol{e}_{\boldsymbol{1}}' + a_6 \boldsymbol{e}_{\boldsymbol{2}}') \tag{B.9}$$

which also can be expressed as

$$\left.\frac{d\boldsymbol{A}}{dt}\right|_I = \left.\frac{d\boldsymbol{A}}{dt}\right|_M + \boldsymbol{e}_1'(-a_1 A_2' - a_2 A_3') + \boldsymbol{e}_2'(-a_1 A_1' - a_4 A_3') + \boldsymbol{e}_3'(-a_1 A_1' - a_4 A_2') \tag{B.10}$$

Recognize the evaluation rule of the vector product in the last three terms:

$$\boldsymbol{C} \times \boldsymbol{A} = \begin{vmatrix} \boldsymbol{e}_1' & \boldsymbol{e}_2' & \boldsymbol{e}_2' \\ C_1 & C_2 & C_3 \\ A_1' & A_2' & A_3' \end{vmatrix} = \boldsymbol{e}_1'(C_2 A_3' - C_3 A_2') - \boldsymbol{e}_2'(C_1 A_3' - C_3 A_1') + \boldsymbol{e}_3'(C_1 A_2' - C_2 A_1') \tag{B.11}$$

and by setting $C = (a_4, -a_2, a_1)$ it follows that

$$\left.\frac{d\boldsymbol{A}}{dt}\right|_I = \left.\frac{d\boldsymbol{A}}{dt}\right|_M + \boldsymbol{C} \times \boldsymbol{A} \tag{B.12}$$

where $\boldsymbol{C}$ is a vector. To find the meaning of $\boldsymbol{C}$, consider the special case of pure rotation around the z-axis in the inertial frame, i.e. the z-axis and the z'-axis coincide and $d\boldsymbol{A}/dt|_M = 0$, i.e. the motion of the vector $\boldsymbol{A}(t)$ in the moving frame vanishes. This means that $\boldsymbol{A}(t)$ is fixed in the moving frame and rotates with the frame around the z-axis. Now let θ be the north-pole angle by which $\boldsymbol{A}(t)$ is inclined from the rotation axis, see Figure B.2. The component parallel to the angular velocity ω is not changed by the rotation. The motion of $\boldsymbol{A}(t)$ in the inertial frame can then be described by the equation

$$\left.\frac{d\boldsymbol{A}}{dt}\right|_I = \omega A \sin(\theta) \tag{B.13}$$

which also equals

$$\left.\frac{d\boldsymbol{A}}{dt}\right|_I = \omega \times \boldsymbol{A} \tag{B.14}$$

Since the choice of the vector $\boldsymbol{A}(t)$ can be made arbitrarily, $\boldsymbol{C}$ must represent the angular velocity ω of the rotating system M. By insertion in Eq.(B.12) this yields

$$\left.\frac{d\boldsymbol{A}}{dt}\right|_I = \left.\frac{d\boldsymbol{A}}{dt}\right|_M + \omega \times \boldsymbol{A} \tag{B.15}$$

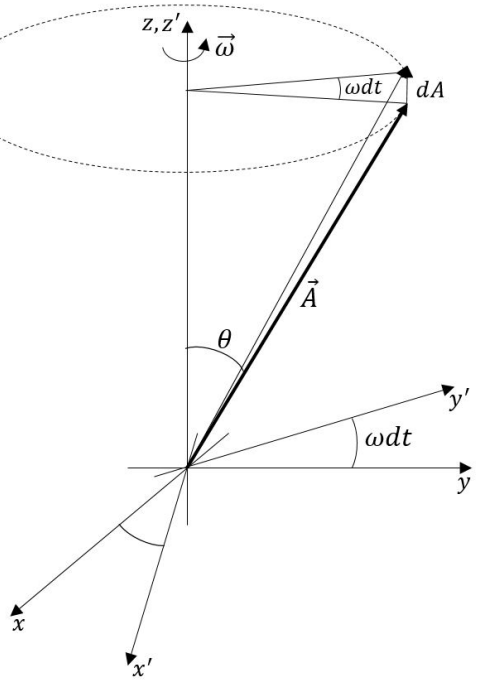

Figure B.2: Change of the position vector $\boldsymbol{A}$ tightly fixed in a rotating reference frame.

B.2 $\hat{\mathcal{D}}$ operator

For readability the expressions are shortened and the operator $\hat{\mathcal{D}} = \partial/\partial t$ is introduced. This yields the two expressions

$$\hat{\mathcal{D}}_I = \left.\frac{\partial}{\partial t}\right|_I \quad \text{and} \quad \hat{\mathcal{D}}_M = \left.\frac{\partial}{\partial t}\right|_M \tag{B.16}$$

which simplifies the Eq.(B.15) to

$$\hat{\mathcal{D}}_I \boldsymbol{A} = \hat{\mathcal{D}}_M \boldsymbol{A} + \omega \times \boldsymbol{A} \tag{B.17}$$

This operator can operate on arbitrary vectors and the expression looks as follows, with $\boldsymbol{A}$ omitted

$$\hat{\mathcal{D}}_I = \hat{\mathcal{D}}_M + \omega\times \tag{B.18}$$

B.3 Newton's equation in systems with pure rotation

Now consider Figure (B.2) again, instead of vector $\boldsymbol{A}$, call the position vector for $\boldsymbol{R}$ instead, i.e. $\boldsymbol{R}$ is the position vector in the accelerating system. In the accelerated system the fictitious forces must be derived since Newton's law $m\ddot{\boldsymbol{R}} = \boldsymbol{F}$ only holds in the inertial system. Again consider the case of pure rotation, to obtain the modified Newton's equation for the accelerating reference system the first step is to differentiate Eq.(B.15)

$$\begin{aligned}\ddot{\boldsymbol{R}}_I &= \frac{d}{dt}(\dot{\boldsymbol{R}})_I = \hat{\mathcal{D}}_I(\hat{\mathcal{D}}_I\boldsymbol{R}) = (\hat{\mathcal{D}}_M + \omega\times)(\hat{\mathcal{D}}_M\boldsymbol{R} + \omega\times\boldsymbol{R}) = \\ &= \hat{\mathcal{D}}_M^2\boldsymbol{R} + \hat{\mathcal{D}}_M(\omega\times\boldsymbol{R}) + \omega\times\hat{\mathcal{D}}_M\boldsymbol{R} + \omega\times(\omega\times\boldsymbol{R}) = \\ &= \hat{\mathcal{D}}_M^2\boldsymbol{R} + (\hat{\mathcal{D}}_M\omega)\times\boldsymbol{R} + 2\omega\times\hat{\mathcal{D}}_M\boldsymbol{R} + \omega\times(\omega\times\boldsymbol{R})\end{aligned} \tag{B.19}$$

By replacing the operator $\mathcal{D}$ with the usual differential quotient the following expression for the acceleration is obtained

$$\left.\frac{d^2\boldsymbol{R}}{dt^2}\right|_I = \left.\frac{d^2\boldsymbol{R}}{dt^2}\right|_M + \left.\frac{d\omega}{dt}\right|_M \times \boldsymbol{R} + 2\omega\times\left.\frac{d\boldsymbol{R}}{dt}\right|_M + \omega\times(\omega\times\boldsymbol{R}) \tag{B.20}$$

Multiplying the above equation with the mass m yields the force $\boldsymbol{F}$

$$\boldsymbol{F} = m\left.\frac{d^2\boldsymbol{R}}{dt^2}\right|_M + m\left.\frac{d\omega}{dt}\right|_M \times \boldsymbol{R} + 2m\omega\times\left.\frac{d\boldsymbol{R}}{dt}\right|_M + m\omega\times(\omega\times\boldsymbol{R}) \tag{B.21}$$

and finally, by rearranging this equation Newton's equation in the accelerating system is obtained

$$m\left.\frac{d^2\boldsymbol{R}}{dt^2}\right|_M = \boldsymbol{F} - \left.\frac{d\omega}{dt}\right|_M \times \boldsymbol{R} - 2m\omega\times\left.\frac{d\boldsymbol{R}}{dt}\right|_M - m\omega\times(\omega\times\boldsymbol{R}) \tag{B.22}$$

The three terms $m(d\omega/dt)|_M \times \boldsymbol{R}$, $2m\omega\times(d\boldsymbol{R}/dt)|_M$ *and* $m\omega\times(\omega\times\boldsymbol{R})$ are the fictitious forces appearing due to the accelerating reference frame. They are called the *Euler force*, *Coriolis force* and *centripetal force* respectively.

B.4 Newton's equation in systems with arbitrary general motion

Now consider an arbitrary general motion of the accelerating reference system, i.e. the condition that the origins of the two reference systems should coincide is no longer applied. This motion consists of both a rotation of the reference frame and a translation of the origin. Consider Figure (B.3), here $\boldsymbol{r}$ points to the origin of the primed reference system and $\boldsymbol{r'}$ is a position vector in the primed reference system. Thus the position vector $\boldsymbol{R}$ in the inertial system can be expressed as

$$\boldsymbol{R} = \boldsymbol{r} + \boldsymbol{r'} \tag{B.23}$$

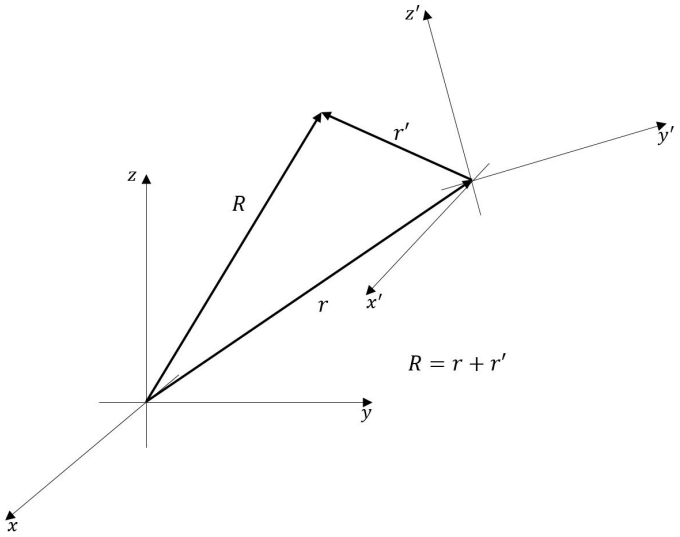

Figure B.3: Relative position of the reference frames with coordinates (*x,y,z*) and (*x'*,*y'*,*z'*).

Now Newton's equation in the inertial system is expressed

$$m\frac{d^2\boldsymbol{R}}{dt^2}\bigg|_I = \boldsymbol{F}_I = \boldsymbol{F} \tag{B.24}$$

and by inserting the expression of the position vector from Eq.(B.23) and performing the differentiation as performed above, the following expression is obtained

$$m\frac{d^2\boldsymbol{r'}}{dt^2}\bigg|_M = \boldsymbol{F} - m\frac{d^2\boldsymbol{r}}{dt^2}\bigg|_I - m\frac{d\boldsymbol{\omega}}{dt}\bigg|_M \times \boldsymbol{r'} - 2m\boldsymbol{\omega} \times \frac{d\boldsymbol{r'}}{dt}\bigg|_M - m\boldsymbol{\omega} \times (\boldsymbol{\omega} \times \boldsymbol{r'}) \tag{B.25}$$

(Greiner, 2003).

C| Appendix 3

C.1 Equations of motion of an inverted spherical pendulum

The first approach to model the occupant was to model the upper body as an inverted spherical pendulum consisting of a massless rigid rod, connecting a point mass to a pivot point in the origin of a reference system. The point mass coordinates $\boldsymbol{r} = (x, y, z)$ can be uniquely specified by a set of state variables (θ, φ, r), where θ is the north-pole angle, φ is the azimuth, and r is the rod length, see Figure 3.4b in section 3.1. To avoid singularities near the north-pole, i.e. the region near $\theta = n\pi$ for $n = 0, 2, 4, ...$, the reference frame in the model is rotated clockwise 90° around the *y-axis*, see Figure 3.3 in section 3.1.

Note that the *z-axis* is the longitudinal axis, positive indicates the direction of travel of the vehicle. The *y-axis* is the same as the old system while the *x-axis* is the vertical axis which points downwards to the "ground". The Cartesian coordinates of the point mass in the new system are denoted

$$\begin{aligned} x &= -r\sin(\theta)\sin(\varphi) \\ y &= r\sin(\theta)\cos(\varphi) \\ z &= r\cos(\theta) \end{aligned} \tag{C.1}$$

The inverted spherical pendulum is configured with two spring-damper pairs acting in the direction of θ and φ at the pivot point. The starting point of the derivation of the equations of motion is the Lagrangian as described in section 2.5.1. The Lagrangian for a system of particles can be defined by

$$\mathcal{L} = T - V \tag{C.2}$$

where T is the total kinetic energy of the system, defined as

$$T = \frac{1}{2}\sum_{k}^{N} m_k \boldsymbol{v}_k^2 \tag{C.3}$$

where m_k is the mass and $\boldsymbol{v}$ is the velocity of each particle, respectively. For the inverted spherical pendulum, consisting of a massless rod and a single point mass, $k = 1$ and the kinetic energy is thus calculated by the equation

$$T = \frac{1}{2} m \boldsymbol{v}^2 \tag{C.4}$$

The square of the velocity $\boldsymbol{v}$ of the particle can be expressed in terms of the time derivatives of the Cartesian states as follows

$$\boldsymbol{v}^2 = \dot{x}^2 + \dot{y}^2 + \dot{z}^2 \tag{C.5}$$

where the derivatives of the Cartesian states are

$$\begin{aligned} \dot{x} &= -r(\dot{\theta}\cos\theta\sin\varphi + \dot{\varphi}\sin\theta\cos\varphi) \\ \dot{y} &= r(\dot{\theta}\cos\theta\cos\varphi - \dot{\varphi}\sin\theta\sin\varphi) \\ \dot{z} &= -r\dot{\theta}\sin\theta \end{aligned} \tag{C.6}$$

which by squaring each of the equations in Eq.(C.6) yields that $\boldsymbol{v}^2$ can be expressed in terms of the generalized coordinates θ and φ as follows

$$\boldsymbol{v}^2 = r^2(\dot{\theta}^2 + \dot{\varphi}^2 \sin^2\theta) \tag{C.7}$$

and thus, the kinetic energy of the inverted spherical pendulum is

$$T = \frac{1}{2} m r^2(\dot{\theta}^2 + \dot{\varphi}^2 \sin^2\theta) \tag{C.8}$$

The potential energy V, of the pendulum is a combination of the mass of the pendulum and the torsion springs included at the pivot point. The potential energy can be defined as

$$V = mgx + \frac{1}{2}k_\theta\theta^2 + \frac{1}{2}k_\varphi\varphi^2 = -mgr\sin\theta\sin\varphi + \frac{1}{2}k_\theta\theta^2 + \frac{1}{2}k_\varphi\varphi^2 \tag{C.9}$$

where m is the particle mass, $g = 9.81$ m/s^2 is the gravitational constant, x is the vertical distance from the pivot point to the mass particle and k_θ and k_φ are the spring coefficients of the torsion springs. The springs exert a torque on the pendulum proportional to the angle of rotation, i.e. the spring coefficients is of unit Nm/rad. Combining Eq.(C.8) and Eq.(C.9) the Lagrangian can now be expressed as

$$\mathcal{L} = \frac{1}{2} m r^2(\dot{\theta}^2 + \dot{\varphi}^2 \sin^2\theta) + mgr\sin\theta\sin\varphi - \frac{1}{2}k_\theta\theta^2 - \frac{1}{2}k_\varphi\varphi^2 \tag{C.10}$$

With the Lagrangian expressed in terms of the generalized coordinates we can now shift focus to the dissipative forces of the system, the two dampers. The dampers will exert a torque on the pendulum which is proportional to the angular velocity of the pendulum. The dissipative potential function is called the *Rayleigh's dissipation function*, and can be defined, for the generalized coordinates, as follows

$$D_\theta = \frac{1}{2}c_\theta\dot{\theta}^2 \tag{C.11}$$

$$D_\varphi = \frac{1}{2}c_\varphi\dot{\varphi}^2 \tag{C.12}$$

with the damper coefficients c_θ and c_φ which have the unit Nm·s/rad. Now, the Lagrange's Equations of motion can be expressed from Eq.(2.24) derived in section 2.5.1 as

$$\frac{d}{dt}\left(\frac{\partial\mathcal{L}}{\partial\dot{q}_i}\right) - \frac{\partial\mathcal{L}}{\partial q_i} + \frac{\partial D}{\partial\dot{q}_i} = Q_i^{nc} \qquad \text{for} \quad i = 1, 2, ..., N \tag{C.13}$$

where $q_i = (\theta, \varphi)$ are the generalized coordinates, $\dot{q}_i = (\dot{\theta}, \dot{\varphi})$ are the generalized velocities and Q_i^{nc} are the generalized forces, i.e. forces induced on the pendulum from the seat, the seat belt and the driver's arms.

By performing all the differentiations in Eq.(C.13), we arrive at the following two equations which describe the motion of the pendulum, i.e. the Lagrange's Equations of motion are

$$\ddot{\theta} = (\dot{\varphi}^2\sin\theta + \frac{g}{r}\sin\varphi)\cos\theta - \frac{1}{mr^2}(k_\theta\theta + c_\theta\dot{\theta}) \tag{C.14}$$

$$\ddot{\varphi} = -2\dot{\theta}\dot{\varphi}\frac{\cos\theta}{\sin\theta} + \frac{g}{r}\frac{\cos\varphi}{\sin\theta} - \frac{1}{mr^2\sin^2\theta}(k_\varphi\varphi + c_\varphi\dot{\varphi}) \tag{C.15}$$

These equations describe the motion of the pendulum when it is only affected by gravity but since the vehicle accelerates, hereinafter referred to as *vehicle or system acceleration*,

some additional contributions need to be considered. The vehicle acceleration as well as the fictitious acceleration, arising in an accelerating reference system, need to be included since they induce forces on the pendulum. The forces induced by these accelerations exert a torque about the pendulum pivot point which needs to be included in the equations of motion. The additional terms are the *System force*, the *Euler force*, the *Coriolis force* and the *Centripetal force*. The force induced by the accelerating reference system is expressed as

$$\boldsymbol{F}_{system} = m a_{system} \tag{C.16}$$

and the fictitious forces are expressed as follows

$$\begin{aligned} \boldsymbol{F}_{euler} = & \quad -m\boldsymbol{\omega} \times \boldsymbol{r} \\ \boldsymbol{F}_{coriolis} = & \quad -2m\boldsymbol{\omega} \times \dot{\boldsymbol{r}} \\ \boldsymbol{F}_{centripetal} = & \quad -m\boldsymbol{\omega} \times (\boldsymbol{\omega} \times \boldsymbol{r}) \end{aligned} \tag{C.17}$$

where m is the pendulum mass, a_{system} is the system acceleration, i.e. the acceleration of the reference system, $\boldsymbol{\omega}$ and $\dot{\boldsymbol{\omega}}$ are the angular velocity and angular acceleration of the accelerating reference system, and $\boldsymbol{r}$ and $\dot{\boldsymbol{r}}$ are the pendulum position and velocity in the accelerating reference system. The total contribution of the system and fictitious forces are added in a vector called $\boldsymbol{F}_{total}$

$$\boldsymbol{F}_{total} = \boldsymbol{F}_{system} + \boldsymbol{F}_{euler} + \boldsymbol{F}_{coriolis} + \boldsymbol{F}_{centripetal} \tag{C.18}$$

The resulting torque which $\boldsymbol{F}_{total}$ induces on the pendulum is dependent on the pendulum length r, and the direction as well as the magnitude of the force vector. Note here, that $\boldsymbol{F}_{total}$ is expressed in Cartesian coordinates and hence a transformation into the spherical coordinates is needed. Note that the dot product between a vector $\boldsymbol{a}$ and a unit vector $\hat{\boldsymbol{b}}$, is the projection of $\boldsymbol{a}$ along the direction of $\hat{\boldsymbol{b}}$. This technique can used to express $\boldsymbol{F}_{total}$ in the directions of the spherical unit vectors. The spherical unit vectors for our reference system are defined as follows

$$\hat{\boldsymbol{e}}_r = \frac{\dfrac{d\boldsymbol{r}}{dr}}{\left|\dfrac{d\boldsymbol{r}}{dr}\right|} = \begin{bmatrix} -\sin\theta\sin\varphi \\ \sin\theta\cos\varphi \\ \cos\theta \end{bmatrix} \tag{C.19}$$

$$\hat{\boldsymbol{e}}_\theta = \frac{\dfrac{d\boldsymbol{r}}{d\theta}}{\left|\dfrac{d\boldsymbol{r}}{d\theta}\right|} = \begin{bmatrix} -\cos\theta\sin\varphi \\ \cos\theta\cos\varphi \\ -\sin\theta \end{bmatrix} \tag{C.20}$$

$$\hat{\boldsymbol{e}}_\varphi = \frac{\dfrac{d\boldsymbol{r}}{d\varphi}}{\left|\dfrac{d\boldsymbol{r}}{d\varphi}\right|} = \begin{bmatrix} -\cos\varphi \\ \sin\varphi \\ 0 \end{bmatrix} \tag{C.21}$$

The directions of the spherical unit vector can be observed in Figure C.1.

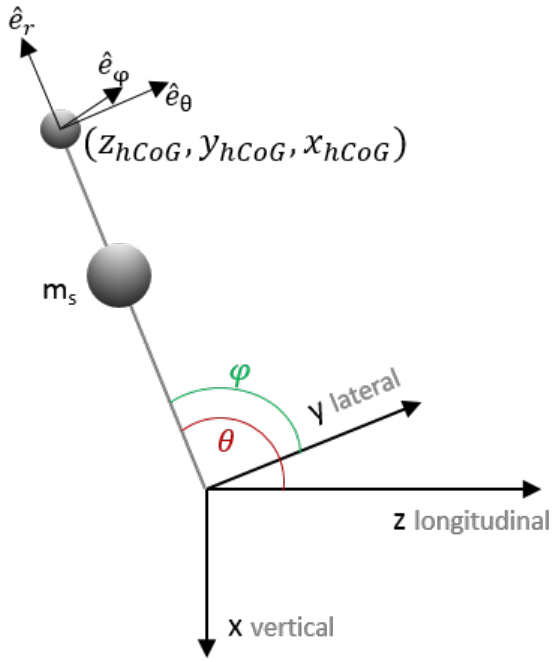

Figure C.1: Spherical unit vectors relative the Cartesian reference frame as defined in Eq.(C.19), Eq.(C.20) and Eq.(C.21).

Note that $\hat{\boldsymbol{e}}_r$ points along the rigid rod which means there is no contribution of the portion of $\boldsymbol{F}_{total}$ acting along $\hat{\boldsymbol{e}}_r$. Since both $\hat{\boldsymbol{e}}_\theta$ and $\hat{\boldsymbol{e}}_\varphi$ are perpendicular to the pendulum rod, the torque contribution to the system is the force acting along $\hat{\boldsymbol{e}}_\theta$ and $\hat{\boldsymbol{e}}_\varphi$ times the lever from the pivot point. This expands Eq.(C.14) and (C.15) to the following equations

$$\ddot{\theta} = (\dot{\varphi}^2 \sin\theta + \frac{g}{r}\sin\varphi)\cos\theta - \frac{1}{mr^2}(k_\theta\theta + c_\theta\dot{\theta}) + \frac{r}{mr^2}\boldsymbol{F}_{total}\cdot\hat{\boldsymbol{e}}_\theta \tag{C.22}$$

$$\ddot{\varphi} = -2\dot{\theta}\dot{\varphi}\frac{\cos\theta}{\sin\theta} + \frac{g}{r}\frac{\cos\varphi}{\sin\theta} - \frac{1}{mr^2\sin^2\theta}(k_\varphi\varphi + c_\varphi\dot{\varphi}) + \frac{r}{mr^2\sin^2\theta}\boldsymbol{F}_{total}\cdot\hat{\boldsymbol{e}}_\varphi \tag{C.23}$$

The contributions of the restraint systems also need to be added to the equations of motion. The restraint systems include the seat belt, the seat and, if the model is simulated as a driver, the arms. The restraint systems induce forces on the pendulum which are defined as Cartesian vectors, $\boldsymbol{F}_{sb}$, $\boldsymbol{F}_s$ and $\boldsymbol{F}_a$ such that they are applied on the pendulum in the sternum point, i.e. at the length r from the pivot point. Since these are Cartesian vectors this means that their contribution to the equations of motion can be added in an analogous procedure just as for the fictitious forces. This yields to the following equations

$$\ddot{\theta} = (\dot{\varphi}^2 \sin\theta + \frac{g}{r}\sin\varphi)\cos\theta - \frac{1}{mr^2}(k_\theta\theta + c_\theta\dot{\theta}) + \frac{r}{mr^2}\boldsymbol{F}_{total}\cdot\hat{\boldsymbol{e}}_\theta + \frac{r}{mr^2}\boldsymbol{F}_r\cdot\hat{\boldsymbol{e}}_\theta \tag{C.24}$$

$$\ddot{\varphi} = -2\dot{\theta}\dot{\varphi}\frac{\cos\theta}{\sin\theta} + \frac{g}{r}\frac{\cos\varphi}{\sin\theta} - \frac{1}{mr^2\sin^2\theta}(k_\varphi\varphi + c_\varphi\dot{\varphi}) + \frac{r}{mr^2\sin^2\theta}\boldsymbol{F}_{total}\cdot\hat{\boldsymbol{e}}_\varphi + \frac{r}{mr^2\sin^2\theta}\boldsymbol{F}_r\cdot\hat{\boldsymbol{e}}_\varphi \tag{C.25}$$

where $\boldsymbol{F}_r$ is the restraint system force resultant vector, $\boldsymbol{F}_r = \boldsymbol{F}_{sb} + \boldsymbol{F}_s + \boldsymbol{F}_a$. These equations

can be expressed in the following equation system:

$$\underbrace{\begin{bmatrix} mr^2 & 0 \\ 0 & mr^2\sin^2\theta \end{bmatrix}}_{\boldsymbol{M(\theta)}} \underbrace{\begin{bmatrix} \ddot{\theta} \\ \ddot{\varphi} \end{bmatrix}}_{\{\ddot{q}_i\}} = \underbrace{\begin{bmatrix} 0 & mr^2\dot{\varphi}\cos\theta\sin\theta \\ -mr^2\dot{\varphi}\cos\theta\sin\theta & -mr^2\dot{\theta}\cos\theta\sin\theta \end{bmatrix}}_{\boldsymbol{S(q,\dot{q})}} \underbrace{\begin{bmatrix} \dot{\theta} \\ \dot{\varphi} \end{bmatrix}}_{\{\dot{q}_i\}} + \underbrace{\begin{bmatrix} mrg\cos\theta\sin\varphi \\ mrg\cos\varphi\sin\theta \end{bmatrix}}_{\boldsymbol{G(q)}} - \underbrace{\begin{bmatrix} k_\theta\theta \\ k_\varphi\varphi \end{bmatrix}}_{\boldsymbol{K(q)}} - \underbrace{\begin{bmatrix} c_\theta\dot{\theta} \\ c_\varphi\dot{\varphi} \end{bmatrix}}_{\boldsymbol{C(\dot{q})}} + \underbrace{\begin{bmatrix} \boldsymbol{F}_{total} r\hat{\boldsymbol{e}_\theta} \\ \boldsymbol{F}_{total} r\hat{\boldsymbol{e}_\varphi} \end{bmatrix}}_{\boldsymbol{N(q)}} + \underbrace{\begin{bmatrix} \boldsymbol{F}_r r\hat{\boldsymbol{e}_\theta} \\ \boldsymbol{F}_r r\hat{\boldsymbol{e}_\varphi} \end{bmatrix}}_{\boldsymbol{R(q)}} \tag{C.26}$$

$\boldsymbol{M(q)}$ is the system mass matrix, $\boldsymbol{S(q,\dot{q})}$ is the coupling matrix, $\boldsymbol{G(q)}$, $\boldsymbol{K(q)}$ and $\boldsymbol{C(\dot{q})}$ are the gravity, spring and damping contributions. $\boldsymbol{N(q)}$ and $\boldsymbol{R(q)}$ are the system, fictitious and restrains forces, respectively.

D| Appendix 4

D.1 Equations of motion of an inverted spherical double pendulum

The second approach to model the occupant is a development of the first model. Instead of modeling the occupant as a single rod a hinge joint was added to act as a "neck joint", making it an inverted spherical double pendulum. The developed model is a double pendulum in the sense that it has two rods, but the second rod can only move longitudinal relative the first rod. As for the first single pendulum the rods are rigid and massless which brings a three DoF system with the generalized coordinates $(\theta_1, \varphi, \theta_2)$.

Just as for the first model the reference frame is rotated to avoid singularities near the region pointing vertically upwards, see Figure 3.3 in section 3.1. Figure 3.5b in section 3.1 is a schematic figure of the double pendulum. The total mass of the upper body is divided into two point masses, the first represents sternum $m_1 = 40$ kg and the second represents the head $m_2 = 6$ kg. Each of the joints are constrained with spring-damper pairs which restrain the rotations about the generalized coordinates.

The hinge joint is placed in the position of the T1 vertebra to approximately resemble the "neck-joint". The first point mass is placed in the sternum position on the first rod while the second point mass is placed at the end of the second rod to resemble the head. The expressions for the Cartesian coordinates of the sternum and the T1 position only differ by the lever lengths, first we introduce the expressions for the sternum positing denoted (x_1, y_1, z_1)

$$\begin{aligned} x_1 &= -r_1 \sin\theta_1 \sin\varphi \\ y_1 &= r_1 \sin\theta_1 \cos\varphi \\ z_1 &= r_1 \cos\theta_1. \end{aligned} \tag{D.1}$$

where r_1 is the rod length from the pivot point to sternum. The position of T1 is denoted (x_2, y_2, z_2) and is expressed as follows

$$\begin{aligned} x_2 &= -r_2 \sin\theta_1 \sin\varphi \\ y_2 &= r_2 \sin\theta_1 \cos\varphi \\ z_2 &= r_2 \cos\theta_1 \end{aligned} \tag{D.2}$$

where r_2 is the rod length from the pivot point to the T1 vertebra. Note how the difference in the sternum position and T1 position only differs by the lever length. The head center of gravity position is computed relative the horizontal plane at the end of the first pendulum rod, as can be seen in 3.5b in section 3.1. Thus, the head position is the addition of the T1 position and the local head position, here denoted (x_3, y_3, z_3)

$$\begin{aligned} x_3 &= x_2 - r_3 \sin\theta_2 \sin\varphi \\ y_3 &= y_2 + r_3 \sin\theta_2 \cos\varphi \\ z_3 &= z_2 + r_3 \cos\theta_2 \end{aligned} \tag{D.3}$$

where r_3 is the rod length from the T1 vertebra to the head CoG.

The procedure to derive the equations of motion for the double pendulum is analogous to the procedure in appendix C. We start by defining the Lagrangian of the system

$$\mathcal{L} = T - V \tag{D.4}$$

where T is the total kinetic energy, i.e. the sum of the kinetic energy of each of the two point masses

$$T = \frac{1}{2}m_1\boldsymbol{v}_1^2 + \frac{1}{2}m_2\boldsymbol{v}_2^2 \tag{D.5}$$

where the expression for $\boldsymbol{v}_1$ and $\boldsymbol{v}_2$ can be written

$$\boldsymbol{v}_1 = \dot{x}_1^2 + \dot{y}_1^2 + \dot{z}_1^2 \tag{D.6}$$

$$\boldsymbol{v}_2 = \dot{x}_3^2 + \dot{y}_3^2 + \dot{z}_3^2 \tag{D.7}$$

Squaring the time derivative of the Cartesian states and adding the terms together yields the following expression for the kinetic energy

$$\begin{aligned} T = &\frac{1}{2}m_1 r_1^2\Big(\dot{\theta_1}^2 + \dot{\varphi}^2\sin^2\theta_1\Big) + \\ &\frac{1}{2}m_2\Big(r_2^2(\dot{\theta_1}^2 + \dot{\varphi}^2\sin^2\theta_1) + 2r_2r_3(\dot{\theta_1}\dot{\theta_2}\cos(\theta_1-\theta_2) + \dot{\varphi}^2\sin\theta_1\sin\theta_2) + \\ &r_3^2(\dot{\theta_2}^2 + \dot{\varphi}^2\sin^2\theta_2\Big). \end{aligned} \tag{D.8}$$

The potential energy, V, is the combination of the potential energy of the two point masses, and the potential energy stored in each of the three torsion springs which restrain the joints of the pendulum. The expression for the potential energy can be defined as

$$\begin{aligned} V &= m_1gx_1 + m_2gx_3 + \frac{1}{2}k_{\theta_1}\theta_1^2 + \frac{1}{2}k_\varphi\varphi^2 + \frac{1}{2}k_{\theta_1}\theta_1^2 \\ &= -m_1gr_1\sin\theta_1\sin\varphi - m_2g(r_2\sin\theta_1\sin\varphi + r_3\sin\theta_2\sin\varphi) + \frac{1}{2}k_{\theta_1}\theta_1^2 + \frac{1}{2}k_\varphi\varphi^2 + \frac{1}{2}k_{\theta_1}\theta_1^2 \end{aligned} \tag{D.9}$$

This yields the Lagrangian

$$\begin{aligned} \mathcal{L} = &\frac{1}{2}m_1 r_1^2\Big(\dot{\theta_1}^2 + \dot{\varphi}^2\sin^2\theta_1\Big) + \\ &\frac{1}{2}m_2\Big(r_2^2(\dot{\theta_1}^2 + \dot{\varphi}^2\sin^2\theta_1) + 2r_2r_3(\dot{\theta_1}\dot{\theta_2}\cos(\theta_1-\theta_2) + \dot{\varphi}^2\sin\theta_1\sin\theta_2) + \\ &r_3^2(\dot{\theta_2}^2 + \dot{\varphi}^2\sin^2\theta_2\Big) + m_1gr_1\sin\theta_1\sin\varphi + m_2g(r_2\sin\theta_1\sin\varphi - r_3\sin\theta_2\sin\varphi) - \\ &\frac{1}{2}k_{\theta_1}\theta_1^2 - \frac{1}{2}k_\varphi\varphi^2 - \frac{1}{2}k_{\theta_1}\theta_1^2 \end{aligned} \tag{D.10}$$

The Lagrangian is now expressed in terms of the generalized coordinates and we can shift focus to the dissipative terms of the system, the three dampers. This is executed using *Rayleigh's dissipation function* just as for the single pendulum and the three terms become

$$D_{\theta_1} = \frac{1}{2}c_{\theta_1}\dot{\theta_1}^2 \tag{D.11}$$

$$D_{\varphi} = \frac{1}{2} c_{\varphi} \dot{\varphi}^2 \tag{D.12}$$

$$D_{\theta_2} = \frac{1}{2} c_{\theta_2} \dot{\theta_2}^2 \tag{D.13}$$

The Lagrange's equations of motion can now be derived via

$$\frac{d}{dt}\left(\frac{\partial \mathcal{L}}{\partial \dot{q}_i}\right) - \frac{\partial \mathcal{L}}{\partial q_i} + \frac{\partial D}{\partial \dot{q}_i} = Q_i^{nc} \qquad \text{for} \quad i = 1, 2, ..., N \tag{D.14}$$

where $q_i = (\theta_1, \varphi, \theta_2)$ are the generalised coordinates, $\dot{q_i} = (\dot{\theta_1}, \dot{\varphi}, \dot{\theta_1})$ are the generalized velocities, and Q_i^{nc} are the generalized forces, i.e. forces induced on the pendulum from the seat, the seat belt, and the driver's arms.

Performing all the differentions in Eq.(D.14) yields the equations of motion for the double pendulum. The additions of the forces induced by the accelerating reference system and fictitious forces $\boldsymbol{F}_{total}$ and restraint forces $\boldsymbol{F}_r$ are added to the equation system as previously described in Appendix C, i.e. we compute the force vectors and compute their contribution in the directions of the spherical unit vectors. For space issues the following abbreviations are used in the expressions of the equations

- $c\theta_1 = \cos\theta_1$
- $c\varphi = \cos\varphi$
- $c\theta_2 = \cos\theta_2$
- $s\theta_1 = \sin\theta_1$
- $s\varphi = \sin\varphi$
- $s\theta_2 = \sin\theta_2$
- $s^2\theta_1 = \sin^2\theta_1$
- $c\alpha = \cos(\theta_1 - \theta_2)$
- $s\alpha = \sin(\theta_1 - \theta_2)$

The full equation system can be seen on the following page.

$$\underbrace{\begin{bmatrix} m_1 r_1^2 + m_2 r_2^2 & 0 & m_2 r_2 r_3 c\alpha \\ 0 & m_1 r_1^2 s^2\theta_1 + m_2(r_2 s\theta_1 + r_3 s\theta_2)^2 & 0 \\ m_2 r_2 r_3 c\alpha & 0 & m_2 r_3^2 \end{bmatrix}}_{\boldsymbol{M(q,\dot{q})}} \underbrace{\begin{bmatrix} \ddot{\theta}_1 \\ \ddot{\varphi} \\ \ddot{\theta}_2 \end{bmatrix}}_{\{\ddot{q}_i\}} =$$

$$\underbrace{\begin{bmatrix} 0 & (m_1 r_1^2 + m_2 r_2^2)\dot{\varphi} c\theta_1 s\theta_1 + m_2 r_2 r_3 \dot{\varphi} c\theta_1 s\theta_2 & -m_2 r_2 r_3 \dot{\theta_2} s\alpha \\ -(m_1 r_1^2 + m_2 r_2^2)\dot{\varphi} c\theta_1 s\theta_1 - m_2 r_2 r_3 \dot{\varphi} c\theta_1 s\theta_2 & -(m_1 r_1^2 + m_2 r_2^2)\dot{\theta_1} c\theta_1 s\theta_1 - m_2 r_2 r_3 \dot{\theta_1} c\theta_1 s\theta_2 - m_2 r_2 r_3 \dot{\theta_2} c\theta_2 s\theta_1 - m_2 r_3^2 \dot{\theta_2} c\theta_2 s\theta_2 & -m_2 r_2 r_3 \dot{\varphi} c\theta_2 a\theta_1 - m 2_{r_3}^3 \dot{\varphi} c\theta_2 s\theta_2 \\ m_2 r_2 r_3 \dot{\theta_2} s\alpha & m_2 r_2 r_3 \dot{\varphi} c\theta_2 a\theta_1 + m 2_{r_3}^3 \dot{\varphi} c\theta_2 s\theta_2 & 0 \end{bmatrix}}_{\boldsymbol{M\dot{q},\dot{q}}} \underbrace{\begin{bmatrix} \dot{\theta}_1 \\ \dot{\varphi} \\ \dot{\theta}_2 \end{bmatrix}}_{\{\dot{q}_i\}} +$$

$$\underbrace{\begin{bmatrix} (m_1 r_1 + m_2 r_2) g c\theta_1 s\varphi \\ ((m_1 r_1 + m_2 r_2) s\theta_1 + m_2 r_3 s\theta_2) c\varphi \\ m_2 r_3 g c\theta_2 s\varphi \end{bmatrix}}_{\boldsymbol{G(q)}} - \underbrace{\begin{bmatrix} k_{\theta_1}\theta_1 \\ k_\varphi \varphi \\ k_{\theta_2}\theta_2 \end{bmatrix}}_{\boldsymbol{K(q)}} - \underbrace{\begin{bmatrix} c_{\theta_1}\dot{\theta}_1 \\ c_\varphi \dot{\varphi} \\ c_{\theta_2}\dot{\theta}_2 \end{bmatrix}}_{\boldsymbol{C(\dot{q})}} + \underbrace{\begin{bmatrix} (m_1 + m_2)\boldsymbol{a}_{total} r_1 \hat{\boldsymbol{e}_{\theta_1}} \\ (m_1 + m_2)\boldsymbol{a}_{total} r_1 \hat{\boldsymbol{e}_\varphi} \\ m_2 \boldsymbol{a}_{total} r_3 \hat{\boldsymbol{e}_{\theta_2}} \end{bmatrix}}_{\boldsymbol{N(q)}} + \underbrace{\begin{bmatrix} \boldsymbol{F}_r r_1 \hat{\boldsymbol{e}_{\theta_1}} \\ \boldsymbol{F}_r r_1 \hat{\boldsymbol{e}_\varphi} \\ 0 \end{bmatrix}}_{\boldsymbol{R(q)}} \tag{D.15}$$

$\boldsymbol{M(q)}$ is the system mass matrix, $\boldsymbol{S(q,\dot{q})}$ is the coupling matrix, $\boldsymbol{G(q)}$, $\boldsymbol{K(q)}$ and $\boldsymbol{C(\dot{q})}$ are the gravity, spring and damping contributions. $\boldsymbol{N(q)}$ and $\boldsymbol{R(q)}$ are the, system plus fictitious forces and restrains forces, respectively.

E| Appendix 5

E.1 Additional ERR results

Figure E.1 and E.2 present the longitudinal and lateral displacement of *parameter sets DB*, *DD* and *DE* when an ERR equipped seat belt restrains the double pendulum occupant model. The occupant model is slightly pulled back by the belt after ERR has been activated. Moreover, the displacement is reduced in both longitudinal and lateral direction during the maneuver for all three parameter sets.

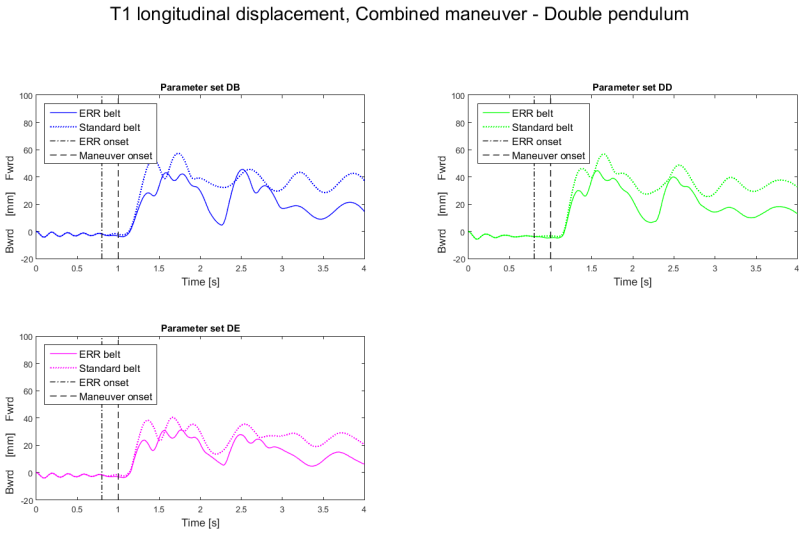

Figure E.1: Longitudinal displacement of T1 for the double pendulum model, where the solid line is the response with ERR, and the dotted line is with a standard belt.

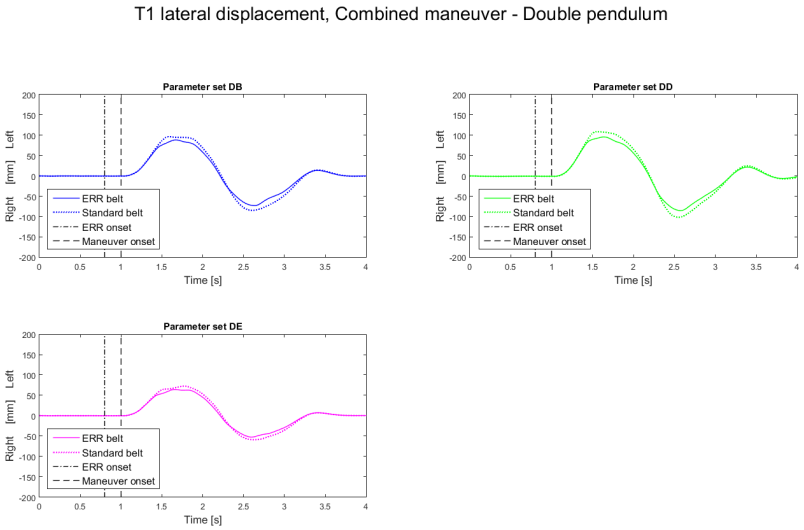

Figure E.2: Lateral displacement of T1 for the double pendulum model, where the solid line is the response with ERR, and the dotted line is with a standard belt.